

A Homogenization Based Phase Field Approach for Solid-State Phase Transitions

Dem Fachbereich Maschinenbau und Verfahrenstechnik
der Technischen Universität Kaiserslautern
zur Verleihung des akademischen Grades
Doktor-Ingenieur (Dr.-Ing.)
genehmigte Dissertation

von
Dipl.-Ing. Simon David Schmidt
aus Saarbrücken

Hauptreferent: Prof. Dr.-Ing. Ralf Müller
Korreferent: Prof. Dr.-Ing. Stefan Diebels
Vorsitzender: Prof. Dr.-Ing. Hans Hasse
Dekan: Prof. Dr.-Ing. Tilmann Beck

Tag der Einreichung: 15.06.2020
Tag der mündlichen Prüfung: 01.09.2020

Kaiserslautern, 2020

Herausgeber

Lehrstuhl für Technische Mechanik
Technische Universität Kaiserslautern
Gottlieb-Daimler-Straße
Postfach 3049
67653 Kaiserslautern

© Simon David Schmidt

Druck

Technische Universität Kaiserslautern
Hauptabteilung 5 / Bau-Technik-Energie
Abteilung 5.6 Foto-Repro-Druck

Alle Rechte vorbehalten, auch das des auszugsweisen Nachdrucks, der auszugsweisen oder vollständigen Wiedergabe (Fotographie, Mikroskopie), der Speicherung in Datenverarbeitungsanlagen und das der Übersetzung.

ISBN 978-3-942695-20-6

Vorwort

Die vorliegende Arbeit wäre nicht entstanden ohne die Unterstützung, Zeit und Hilfe einiger wundervollen Menschen. Deswegen danke ich folgenden Personen sehr herzlich.

An erster Stelle danke ich meinem Doktorvater Prof. Dr.-Ing. Ralf Müller, für die hervorragende Betreuung und Unterstützung. Ohne ihn wäre diese Arbeit nicht möglich gewesen. Weiterhin danke ich Prof. Dr.-Ing. Stefan Diebels für das Korreferat und das Interesse an meiner Arbeit, sowie Prof. Dr.-Ing. Hans Hasse für die Übernahme des Vorsitzes.

Ich danke auch meinen Kollegen am Lehrstuhl für technische Mechanik für die schöne Zeit, die fachlichen Gespräche und Bier. Mein besonderer Dank gilt Kais Ammar und Samuel Forest für die eingiebigen fachlichen Gespräche und Ratschläge sowie für deren Gastfreundschaft in Paris. Ich danke Alexander Schlüter, Ramses Sala und Christian Kaucher für die sehr ausführlichen und hilfreichen Korrekturanmerkungen, sowie Wolfgang Dornisch, Robert Bischof, Paul Breuninger und Fabian Krull für die Inspirationen, die fachlichen, aber auch unterhaltsamen Gespräche.

Zu guter Letzt danke ich meinen langjährigen Freunden Pascal Berrang, Christian Risch, Jonas Abel und Curd Becker, für deren Unterstützung ich sehr dankbar bin. Ich danke meiner Familie, meinen Eltern und meinen Schwestern, deren uneingeschränkte Unterstützung ich habe, dass sie für mich da sind und für alles was sie für mich getan haben.

Saarbrücken, im Juni 2020

Simon Schmidt

Zusammenfassung

Die hier vorliegende Arbeit beschäftigt sich mit der Modellierung von Festkörperphasenübergängen, im Besonderen mit der Martensittransformation. Die beiden Allotrope Austenit und Martensit sind für technische Anwendungen wichtig. Während Austenit duktil und deshalb im Bauteilinneren erwünscht ist, ist es die härtere Martensitphase an der Oberfläche. In Fertigungsprozessen wird dieser Phasenübergang durch schnelles Kühlen hervorgerufen. So ist der Martensitgehalt in Oberflächennähe höher als im Bauteilinneren. Typischerweise bilden spanende Fertigungsverfahren, so wie Drehen und Fräsen, und die Wärmebehandlung zum Oberflächenhärten des Bauteils eine Prozesskette. Das heißt sie werden nacheinander durchgeführt. Ein Prozess, dessen Ziel es ist einen dieser Prozessschritte zu eliminieren, ist das kryogene Drehen. Hierbei wird der Bauteiloberfläche ein kryogener Kühlschmierstoff zugeführt. Als Kühlschmierstoff wird hier zum Beispiel kryogener CO₂-Schnee verwendet (Heep, Bickert und Abele, 2019; Mayer, Kirsch und Aurich, 2014). Der kryogene Drehprozess vereint somit das Drehen und die normalerweise nachgestellte Wärmebehandlung.

Für den Modellierungsaspekt dieser Arbeit ist die Kontinuumsmechanik von entscheidender Bedeutung. Um eine theoretische Grundlage zu schaffen, werden zunächst kinematische Beziehungen eingeführt. Somit ist es möglich anhand gegebener Verschiebungen den Verschiebungsgradienten zu berechnen, der als Voraussetzung für Verzerrungsmaße dient. Mit Hilfe von Bilanzgleichungen können anhand von Kraft- und Momentengleichgewicht, oder genau anhand von Impuls- und Drehimpulsleichgewicht die Feldgleichungen hergeleitet werden. Weiterhin wird das Konzept der Spannung motiviert. Zur weiteren Information dienen die Werke von Gurtin (1982), sowie Becker und Gross (2013).

Allotropie ist eine Eigenschaft von Kristallen. Eisen, aber auch Stahl, weisen in technischen Anwendungen auf der Mikrostrukturebene eine Vielzahl von Allotropen auf. Die Martensittransformation ist aufgrund der Nanostruktur des Martensits von entscheidender Bedeutung (Bhadeshia, 2017). Diese Transformation ist diffusionslos. Sie verläuft dadurch im Vergleich zu diffusionsbehafteten Phasenübergängen schnell und lokalisiert. Hierbei ordnen sich Atome auf einer neuen Gitterstruktur an. Die Atombewegung sind auf interatomare Distanzen beschränkt. Dadurch ist es möglich, die Transformation mit Hilfe einer Orientierungsbeziehung, die das untransformierte und das transformierte Gitter ins Verhältnis setzt, zu beschreiben. Eine Übersicht findet sich in Bhadeshia (2017) und in Kelly (2012). Die phänomenologische Theorie der martensitischen Kristallstruktur (PTMC), welche von Bowles und Mackenzie (1954) und Wechsler, Lieberman und Read (1953) zeitgleich entwickelt wurde, erklärt die Diskrepanz zwischen der Orientierungsbeziehung und der undeformierten Habitus-ebene. Die Triebkräfte der Martensittransformation sind zum Einen die Dehnung und externe Last, da bei der Transformation eine Dehnung eingeführt wird. Weiterhin ist die chemische freie Energie temperaturabhängig. Die Martensittransformation erfolgt, wenn durch eine Umwandlung die freie Energie, bestehend aus einem elastischen und einem chemischen Teil, minimiert werden kann.

Mit Hilfe der Phasenfeldmethode können Phasenübergänge modelliert werden. Die Methode ist nahezu ubiquitär und wurde zur Modellierung von Erstarrungsvorgängen (Wang und Urbassek, 2012), Strukturoptimierung (Muench, Gierden und Wagner, 2018), Bruchvorgängen (Kuhn und Müller, 2010; Miehe, Welschinger und Hofacker, 2010), Weißschen Domänen (Schrade, Mueller, Xu und Gross, 2007; Dornisch, Schrade, Xu, Keip und Müller, 2019; Nadgir, Dornisch, Müller und Keip, 2019), Fluide (Diewald u. a., 2018; Heida, 2013), aber auch der Martensittransformation eingesetzt. Als Referenz dienen hier die Werke von Wang und Khachaturyan (1997) und Schmitt, Wang und Urbassek (2013b). Der Ordnungsparameter dient zur Identifikation der allotropen Phasen. Mit einem skalaren Ordnungsparameter können zwei Allotrope, Austenit und Martensit, dargestellt werden. Mit Hilfe eines Vektors als Ordnungsparameter kann ein multivariantes Phasenfeld beschrieben werden, in dem mehrere Martensitvarianten berücksichtigt werden können. Die Phasenfeldmethode beruht auf Minimierung der freien Energie. Unter Einhalten des ersten Hauptsatzes der Thermodynamik können mit Hilfe der Clausius-Duhem-Ungleichung die Feldgleichungen für das Phasenfeld und das mechanische Problem hergeleitet werden. Die Kopplung beider Gleichungen geschieht durch die Einführung einer Transformationsdehnung. Im multivarianten Fall ist zudem die Interpolation entscheidend. Hier wird eine Methode vorgestellt, in der eine skalare Interpolationsfunktion zum Interpolieren von Größen in einem multivarianten Phasenfeld dient. Als Ergebnis zeigt sich, dass eine lineare Interpolation nur bei maximal zwei Phasen uneingeschränkt zulässig ist. Im Gegensatz zum Khachaturyanmodell kann sie nicht im Voigt/Taylor-Modell verwendet werden, da so die Ableitungen zweiter Ordnung verschwinden. Abhilfe schafft zum Beispiel eine kubische Interpolation.

Die oben angesprochene chemische Energie ist temperaturabhängig. Deswegen wird hier eine temperaturabhängige Modellierung vorgestellt. Zunächst wird der Modellierung von Schmitt, Wang und Urbassek (2013b) im Khachaturyanmodell gefolgt. Die normierte chemische Energie kann durch ein Landau-Polynom beschrieben werden. Mit Hilfe von Molekulardynamik-Simulationen können dessen Parameter temperaturabhängig identifiziert werden. Im Folgenden werden die Parameter des Landau-Polynoms als Funktion der Temperatur beschrieben. Mit Hilfe von Konfigurationskräften kann die Geschwindigkeit der Phasentransformation ermittelt werden. Das Modell wurde mit Hilfe der Finiten Elemente Methode gelöst. Es wurde in FEAP implementiert. Numerische Beispiele dienen zur Illustration der Eigenschaften des Modells.

Um mehrere Martensitorientierungsvarianten berücksichtigen zu können, kann ein multivariantes Phasenfeldmodell verwendet werden. Die Methode nach Khachaturyan beschreibt die effektiven Materialparameter in Abhängigkeit der Phasenzusammensetzung. Somit ist die Wahl des Konstitutivgesetzes direkt von der Phase abhängig, sodass zur numerischen Lösung für jedes Materialgesetz individuelle Residuen und dazugehörige Tangenten aufgestellt werden müssen. Eine Generalisierung ist kompliziert. Einen Ausweg bietet hier die Voigt/Taylor-Methode. Hier wird die elastische Energie homogenisiert, sodass eine Schnittstelle für Konstitutivgesetze in den einzelnen Phasen geschaffen wird. Ein Nachteil dieser Methode ist allerdings, dass für jede Phase ein Materialgesetz gelöst werden muss. Eine Parallelisierung ist jedoch trivial. Die Beschreibung des Modells erfolgt für eine beliebige Anzahl an Phasen. Dank der Unabhängigkeit der Materialgesetze erfolgt die Implementierung in FEAP und in Zébulon generalisiert. Weiterhin wurde die in Schmitt, Wang und Urbassek (2013b) vorgestellte Methode um eine beliebige Anzahl an Phasen erweitert und es wurde eine Schnittstelle für eine beliebige Interpolationsfunktion geschaffen. Anhand von numerischen

Beispielen werden die oben genannten Methoden verglichen. In einigen Fällen liefern beide Methoden die gleichen Endzustände. In der Literatur wird im Khachaturyan-Modell die lineare Interpolation verwendet. Dies kann zu unphysikalischen oder zu falschen Ergebnissen führen. Eine Lösung ist das Verwenden einer nichtlinearen Interpolationsmethode. Dadurch, dass die Interpolation der elastische Energie in dem Voigt/Taylor-Modell und in dem Khachaturyan-Modell unterschiedlich erfolgt, ergeben sich unterschiedliche Geschwindigkeiten der Phasentransformation.

Abstract

This thesis is concerned with the modeling of the solid-solid phase transformation, such as the martensitic transformation. The allotropes austenite and martensite are important for industry applications. As a result of its ductility, austenite is desired in the bulk, as opposed to martensite, which is desired in the near surface region. The phase field method is used to model the phase transformation by minimizing the free energy. It consists of a mechanical part, due to elastic strain and a chemical part, due to the martensitic transformation. The latter is temperature dependent. Therefore, a temperature dependent separation potential is presented here. To accommodate multiple orientation variants, a multivariant phase field model is employed. Using the Khachaturyan approach, the effective material parameters can be used to describe a constitutive model. This however, renders the nodal residual vector and elemental tangent matrix directly dependent on the phase, making a generalization complicated. An easier approach is the use of the Voigt/Taylor homogenization, in which the energy and their derivatives are interpolated creating an interface for material law of the individual phases.

Contents

Vorwort	i
Zusammenfassung	iii
Abstract	vi
List of Figures	x
List of Tables	xi
Notation and Symbols	xiii
1 Introduction	1
1.1 Motivation	1
1.2 Outline	2
2 Continuum Mechanics	3
2.1 Kinematics	4
2.1.1 Linear theory	7
2.2 Balance Equations	8
2.2.1 Mass Conservation	8
2.2.2 Linear and Angular Momentum Balance	9
2.2.3 Stress	9
3 Martensite Transformation	13
3.1 Lattice Mismatch and Shape Strain	15
3.2 Driving Forces	18
4 Phase Field Models	23
4.1 Multivariant Phase Field	24
4.2 Energetic Setup	25
4.3 Evolution Equation	26
4.4 Interpolation	27
5 A Temperature Dependent Separation Potential	33
5.1 Parameters of the Separation Potential	34
5.1.1 Temperature Dependency	36
5.1.2 Parameter Identification	39
5.2 Model Equations	42
5.3 Implementation	43
5.3.1 Residual and Elemental Stiffness Matrix	43
5.4 Interface Propagation	45
5.4.1 Temperature Dependency of the Interface Propagation	49
5.4.2 Influence of Load on the Interface Propagation	51
5.5 Locally Varying Temperature Field	52
6 A Homogenization Phase Field Approach	55
6.1 Motivation	55
6.2 Assumptions	56

6.2.1	Constitutive Law and Field Equations	59
6.2.2	Elastic Energy	59
6.3	Implementation	62
6.3.1	Residual and Elemental Stiffness Matrix	63
6.3.2	Derivatives of the Elastic Energy	67
6.3.3	Derivatives of the Chemical Energy	67
6.3.4	Technical Details	68
6.4	Basic Considerations	70
6.5	Comparison to the Khachaturyan Approach	74
6.5.1	Using a Non-linear Interpolation Function	78
7	Conclusions	83
7.1	Outlook	85
	Bibliography	95
8	Appendix	97
8.1	Additional Plots for the Interface Velocity	97
8.2	Comparison of Interpolation Methods	98

List of Figures

2.1	A material body in motion	4
2.2	Polar decomposition of the deformation gradient	6
2.3	Concept of stress	10
2.4	Cauchy tetrahedron	11
2.5	Infinitesimal volume element with stress tensor	12
3.1	Two fcc unit cells before and after the transformation	14
3.2	Habit Plane	17
3.3	Crystallographic twinning	17
3.4	The Gibbs free energy and the martensitic transformation induced by stress and strain	18
3.5	Normalized chemical energy and Eshelby inclusion	19
3.6	Inheritance of plastic deformation, and crystallographic defects	20
4.1	Comparison of the analogous and the case dependent approach with constant bulk values using the tanh interpolation	30
5.1	Landau polynomial where $A = 20$, $B = 72$, $C = 52$, and $D = 1$. The metastable ($\phi = 0$) and the stable phase ($\phi = 1$) are indicated for those parameters. The maximum is located at $\phi = \frac{A}{C}$	34
5.2	Landau polynomial (solid lines) and normalized free energy (+) from molecular dynamics simulations at $T = 700$ K (a) and $T = 900$ K (b) (Sandoval, Urbassek, and Entel, 2009).	36
5.3	Energy barrier Δf_L as a function of A for $D = 1$ (solid line) and $D = 0$ (dashes, - -)	37
5.4	Parameter A as a function of the temperature T for varying curvatures where $\gamma_1 \leq \gamma_2 \leq \gamma_3$ according to (5.24)	39
5.5	Parameter A as a function of T (solid line) fitted to value pairs (T, A_{lsq}) in Table 5.1 (+)	41
5.6	Interface motion for $T = 94.95$ K	46
5.7	Interface motion for $T = 1311.99$ K	46
5.8	Interface velocity over time for $T = 94.95$ K	47
5.9	Interface velocity over time for $T = 1311.99$ K	48
5.10	Mean interface velocity \bar{v}_{cf} obtained using configurational forces over the temperature. The inset on the top left shows the region around the equilibrium temperature in detail. The pluses (+) mark the data points.	49
5.11	Mean interface velocity \bar{v}_{cf} obtained using configurational forces over the energy barrier Δf_L with temperatures corresponding to the respective velocities (+)	50
5.12	Mean interface velocity \bar{v}_{cf} over temperature and load	51
5.13	Martensitic transformation at different times t with different initializations s	52

6.1	Flow chart of the Voigt/Taylor homogenization approach	57
6.2	Flow chart of the Khachaturyan approach	58
6.3	Elastic energy in a uniform strain setting	59
6.4	Landau polynomial and its first order derivative	67
6.5	Time evolution for different levels of mesh refinements. The solid colored regions indicate the interface region where $0.8 > \phi_1 > 0.2$ (left, dark gray), and where $0.8 > \phi_2 > 0.2$ (right, light gray). The austenitic phase is present in the center (A), with the martensitic orientation variants to the left (M_1) and to the right (M_2).	71
6.6	Example 1. Order parameter for the Khachaturyan and the Voigt/Taylor approach	74
6.7	Example 1. Energy for the Khachaturyan and the Voigt/Taylor approach	75
6.8	Example 2. Order parameter for the Khachaturyan and the Voigt/Taylor approach	76
6.9	Example 2. Energy for the Khachaturyan and the Voigt/Taylor approach	77
6.10	Example 3. Order parameter for the Khachaturyan and the Voigt/Taylor approach	77
6.11	Example 4. Order parameter for the Khachaturyan and the Voigt/Taylor approach	79
6.12	Time evolution of two spherical martensitic domains for the Khachaturyan approach and the Voigt/Taylor approach	80
7.1	Flow chart of a modified Voigt/Taylor homogenization approach	85
8.1	Interface velocity over time for $T = 654.57$ K	97
8.2	Interface velocity over time for $T = 992.92$ K	97
8.3	Comparison of the analogous and the case dependent approach with constant bulk values using the cubic interpolation	99
8.4	Comparison of the analogous and the case dependent approach with constant varying values using the linear interpolation	99
8.5	Comparison of the analogous and the case dependent approach with constant varying values using the cubic interpolation	100
8.6	Comparison of the analogous and the case dependent approach with constant varying values using the tanh interpolation	100

List of Tables

3.1	Common orientation relationship	14
4.1	Applicability of the analogous and the case dependent interpolation approach	31
5.1	Parameter A over temperature T for different interpolation methods .	40
5.2	Parameters γ , $\hat{\theta}$ and T_0 determined using the method of least squares .	41
5.3	Comparison of interface velocities	49
6.1	Summary of the interpolation	61
6.2	Interface position	73

Notation and Symbols

Symbols

	Symbolic	Components
Scalar	a	
Vector	\underline{a}	a_i
Matrix or 2nd rank tensor	$\underline{\underline{a}}$	a_{ij}
4th rank tensor	$\underline{\underline{\underline{a}}}$	a_{ijkl}

Operations

	Symbolic	Component	Einstein
Scalar product	$c = \underline{a} \cdot \underline{b}$	$c = \sum_i a_i b_i$	$c = a_i b^i$
Cross product	$\underline{c} = \underline{a} \times \underline{b}$	$c_i = \sum_{jk} \epsilon_{ijk} a^j b^k$	$c_i = \epsilon_{ijk} a^j b^k$
Outer/dyadic product	$\underline{\underline{C}} = \underline{a} \otimes \underline{b}$	$C_{ij} = a_i b_j$	$C_{ij} = a_i b_j$
Hadamard product	$\underline{\underline{C}} = \underline{\underline{A}} \circ \underline{\underline{B}}$	$C_{ij} = A_{ij} B_{ij}$	$C_{ij} = A_{ij} B_{ij}$
Matrix product	$\underline{\underline{C}} = \underline{\underline{A}} \underline{\underline{B}}$	$C_{ij} = \sum_k A_{ik} B_{kj}$	$C_{ij} = A_{ik} B^k_j$
Double Contraction	$c = \underline{\underline{A}} : \underline{\underline{B}}$	$c = \sum_{ij} A_{ij} B_{ij}$	$c = A_{ij} B^{ij}$

1 Introduction

1.1 Motivation

Allotropes exhibit different material properties. A well known example for an allotrope is martensite. In contrast to its austenitic parent phase, martensite is less ductile, but less susceptible to force and wear, making it desired in the near surface region. Heat treatment is a process, where, due to rapid cooling, a phase transformation from the austenitic to the martensitic phase is induced. Typically, machining and surface hardening are subsequential steps in the manufacturing process. However, cryogenic turning is a process which unifies these subsequential steps into a single one. A sub zero cooling agent is applied to the cut region, where the tool acts on the workpiece. Therefore, not only the temperature, but as an addition to heat treatment a load is applied to the workpiece.

The martensitic transformation is a process which is dependent on the temperature, but also on the load state, as the transformation introduces a strain. This transformation strain is crucial for the phase transformation. The temperature and the strain interact through the chemical and the mechanical energy, where the phase transformation is driven by the minimization of the free energy. Therefore in this work, a temperature dependent separation potential is developed.

Phase field models are a versatile tool for a variety of interfacial problems. They allow to regularize the sharp interface by the introduction of a phase field variable or order parameter, which identifies the local chemical composition of the material. This simplifies the solution process, as there is no need to track the interface. Often, in literature, a Khachaturyan approach is presented. While it is flexible, as it allows to define a material law in dependence of phase dependent effective material parameters, it comes with the disadvantage that introducing a new material requires to change the numerical implementation of the phase field model. Furthermore, the material law chosen in the Khachaturyan approach needs to comply with each individual phase, e.g., the constitutive model is a unified material law for all the phases. The approach is in contrast to homogenization schemes, such as the Voigt/Taylor and the Reuss/Sachs model. Here, a phase dependent mechanical energy is interpolated. This allows to choose individual material laws within the individual phases. Additionally, the numerical implementation can be generalized to introduce an interface to material laws. That way it is possible to choose the material law of the individual phases freely. A Voigt/Taylor approach is presented, which is compared to a Khachaturyan approach.

1.2 Outline

The second chapter of this thesis is concerned with the theory of continuum mechanics. Here, kinematic equations relating the displacements with the strain measures are established. The linearization to small strain is introduced. Balance equations help to identify the governing field equations. Furthermore, the concept of stress is introduced.

The third chapter demonstrates a brief literature review of the martensite transformation. Common orientation relationships are examined, relating the parent and the transformed child phase geometrically. The Wechsler-Lieberman-Read (WLR), and the Bowles-Mackenzie (BM) theories of martensite transformation are discussed. They both explain the mismatch of the shape strain, exhibiting an invariant plane strain, and the strain derived from the orientation relationship. Together, they form the phenomenological theory of martensite transformation. The knowledge of the transformation strain is crucial for the martensitic transformation. The driving forces, such as the temperature, strain, and stress, are laid out. The martensitic transformation depends on energy minimization, leading to an interplay of the chemical energy due to the phase transformation, and of the mechanical energy because of the transformation strain and the load situation.

In the fourth chapter the phase field method is introduced. The model equations for a phase field with a single variant and a multivariant phase field are presented. The energetic setup is crucial for the martensitic transformation. Additionally, interpolation methods in a multivariant phase field are outlined, where an interpolation method for the vector valued order parameter is presented. This method allows to use scalar interpolation functions, simplifying subsequent implementations.

The fifth chapter is concerned with a temperature dependent separation potential. With the use of data from molecular dynamics simulations, parameters for a temperature dependent chemical potential are identified. A function interpolating those parameters based on energetic considerations is proposed and the parameters of this function are determined. As an additional result, the equilibrium temperature can be determined, such that a temperature dependent energetic landscape can be formulated. The implementation in a finite element scheme is discussed. The kinetics of the phase transformation are compared to molecular dynamics simulation and to the literature.

The development of a homogenization approach in a phase field model for martensitic transformation is presented in the sixth chapter. Here, the advantages and disadvantages are discussed. The Voigt/Taylor model presented in this chapter generalizes the phase field by homogenization of the elastic energy. Therefore, as an advantage already implemented material routines can be used in that framework with the disadvantage that a constitutive law needs to be solved for every phase individually. However, parallelization can mitigate this issue to some extent. Here, the Voigt/Taylor approach stands in contrast to the Khachaturyan model, where a single unified material law is presented by interpolating the effective material parameters. In order to illustrate the findings, numerical examples are given. The Voigt/Taylor approach is compared to the Khachaturyan approach.

Finally, the last chapter draws conclusions from the results in the previous two chapters. A brief outlook on further research is given.

2 Continuum Mechanics

In this work, the martensitic transformation in metastable austenitic steels is the main focus. While there are a variety of atomistic simulations studying this problem, modeling larger length and time scales by atomistic approaches is neither feasible nor effective. Therefore, the present approach relies on the theory of continuum mechanics. The characteristic length scales for material structures that are relevant for the martensitic transformations are in the μm range. For instance the grain size of an average grain in iron is about $20\mu\text{m}$. This is larger by five orders of magnitude than atomistic length scales which are typically in the range of 10 - 100 nm.

Consequently, a continuum model is justified. In continuum mechanics a deformable, material body \mathcal{B} is regarded as a continuum, such that its mass occupies a volume, an area or a line continuously. Therefore, a continuum can be subdivided indefinitely; the smallest subset on such a body is a material point or a particle. Typically, continuum mechanics can be divided into kinematics, describing a material body \mathcal{B} and its particles in motion; into deformation and a strain measure, describing the local deformation due to the relative motion of nearby particles; into the material law, relating the strain measure to stresses, heat energy and entropy; and into the balance equations, which describe the local force and momentum equilibrium. While kinematics and the balance equations are independent of the problem, the material law is problem specific. For more informations, the textbooks of Gurtin (1982), and Becker and Gross (2013) prove as excellent resources.

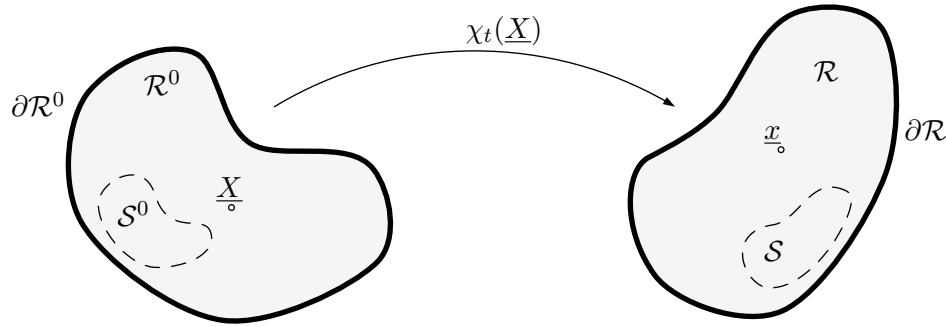


FIGURE 2.1: A material body \mathcal{B} in motion assumes the reference configuration \mathcal{R}^0 at time t_0 and in the actual configuration \mathcal{R} at time t .

2.1 Kinematics

A continuum body \mathcal{B} is a set of material points or particles which, in their entirety, provide the body with local physical properties. A particle of the body \mathcal{B} is denoted by \mathcal{P} . The body can be subdivided into a subregion \mathcal{S} which, mathematically speaking, are subsets of \mathcal{B} . Due to the motion, the body \mathcal{B} occupies several distinct regions or configurations in Euclidean space \mathbb{R}^3 and time t . The motion of \mathcal{B} is a time dependent map $\underline{\chi}_0 : \mathcal{B} \times \mathbb{R} \rightarrow \mathbb{R}^3$ such that

$$\underline{x} = \underline{\chi}_0(\mathcal{P}, t), \quad (2.1)$$

where $\underline{x} \in \mathbb{R}^3$ is the location vector pointing from the fixed origin $\underline{0}$ to the point p which is occupied by the particle \mathcal{P} at time t . The vector \underline{x} is usually represented by its coordinates in an orthonormal basis coordinate system. Due to the motion the body occupies several distinct time dependent configurations. The initial, or undeformed configuration is the reference configuration \mathcal{R}^0 of \mathcal{B} at a fixed time $t = t_0$. A point in the reference configuration is denoted by P , where \underline{X} is its respective location vector. The body assumes several intermediate configurations, eventually leading to the current configuration \mathcal{R} at time t . The map $\underline{\chi}_0$ is assumed bijective for all times t , e.g. only one particle occupies one distinct point at a particular point in time. A subregion \mathcal{S} of \mathcal{B} is transformed using the map $\underline{\chi}_0$ by transforming all its particles into the current subregion $\mathcal{S} = \{p | p = \underline{\chi}_0(\mathcal{P}, t) \forall \mathcal{P} \in \mathcal{S}\}$.

The bijectivity of $\underline{\chi}_0$ allows to define the Lagrangian description of the motion (see Figure 2.1) from the reference to the actual configuration $\underline{\chi} : \mathcal{R}^0 \rightarrow \mathcal{R}$ such that

$$\underline{x} = \underline{\chi}(\underline{X}, t) = \underline{\chi}_t(\underline{X}), \quad \text{where } \underline{\chi}(\underline{X}, t) = \underline{\chi}_0(\underline{\chi}_0^{-1}(\underline{X}, t_0), t). \quad (2.2)$$

Let \underline{E}_I and \underline{e}_i be the right-handed orthonormal bases with a fixed origin $\underline{0}$ for their respective location vectors in the reference \underline{X} and the current configuration \underline{x} . The location vector \underline{X} of a certain particle \mathcal{P} in the reference configuration \mathcal{R}^0 is constant over time and therefore acts as an identifier for the respective particle. For the current configuration however, the location vector \underline{x} is subject to change with respect to time t . The trajectory or pathline of a point occupying \underline{X} in the reference configuration is a function of time $\underline{\chi}(t, \underline{X})$. The location vectors of particles in \mathcal{R}^0 and \mathcal{R} in terms of their respective bases read

$$\underline{X} = X_I \underline{E}^I \quad \text{and} \quad \underline{x} = x_i \underline{e}^i, \quad (2.3)$$

where the Einstein summation convention applies. Transforming an orthogonal coordinate system with a conformal map yields another orthogonal coordinate system. A conformal map is angle and orientation conserving. The map $\chi_t : \mathcal{R}^0 \rightarrow \mathcal{R}$ has to be direction conserving in order to enforce the impenetrability of matter, however it is not necessarily angle conserving as shear deformations may apply. In the following a capital symbol or index identifies a measure in the reference configuration, whereas a small symbol or index refers to a measure in the current configuration. Assuming 2nd order continuity of the map χ with respect to time t , the velocity and the acceleration of a particle read

$$\underline{v} = \frac{d\underline{\chi}_t(\mathcal{P})}{dt} = \dot{\underline{x}} \quad \text{and} \quad \underline{a} = \frac{d^2\underline{\chi}_t(\mathcal{P})}{dt^2} = \frac{d\underline{v}}{dt} = \dot{\underline{v}} = \ddot{\underline{x}}. \quad (2.4)$$

Further, the map χ_t is assumed to be bijective, such that no overlapping of the material points occur for any intermediate and actual configuration. Consider an infinitesimal line element $d\underline{X}$ in the reference configuration, the total differential of (2.2) reads

$$d\underline{x} = \frac{\partial \underline{\chi}_t(\underline{X})}{\partial \underline{X}} d\underline{X} = \underline{\mathbf{F}} d\underline{X}. \quad (2.5)$$

In the following, the distinction between material \underline{X} and spatial \underline{x} coordinates is of importance. In this work, material derivatives, that means derivatives with respect to \underline{X} are denoted with upper case initial letters such as “Div” and “Grad” whereas spatial derivatives, or derivatives with respect to \underline{x} are denoted with lower case initial letters such as “div” and “grad”. Additionally $(\cdot)_{,I}$ with an uppercase index denotes a material derivative $\frac{\partial}{\partial X_I}(\cdot)$, where $(\cdot)_{,i}$ denotes a spatial derivative $\frac{\partial}{\partial x_i}(\cdot)$. The deformation gradient $\underline{\mathbf{F}}$ is defined as the material or Lagrangian derivative of the map $\underline{\chi}_t$:

$$\underline{\mathbf{F}} = \frac{\partial \underline{\chi}(\underline{X}, t)}{\partial \underline{X}} = F_{iJ} \underline{e}_i \otimes \underline{E}_J \quad \text{where} \quad F_{iJ} = \frac{\partial x_i(\underline{X}, t)}{\partial X_J} = x_{i,J}. \quad (2.6)$$

It is a two field tensor, meaning it lives both in the references configuration \mathcal{R}^0 and the current configuration \mathcal{R} and it has a two field tensor basis, which involves both \underline{e}_i and \underline{E}_J . To be precise, the deformation gradient $\underline{\mathbf{F}}$ transforms infinitesimal line elements $d\underline{X}$ from the reference into the current configuration \mathcal{R} . As the map $\underline{\chi}(t, \underline{X})$ is bijective, or invertible, the inverse $\underline{\mathbf{F}}^{-1}$ exists. It can be identified as the map that transforms line elements $d\underline{x}$ from the current configuration back into the reference configuration, i.e.

$$d\underline{X} = \underline{\mathbf{F}}^{-1} d\underline{x} = \frac{\partial \underline{X}}{\partial \underline{x}} d\underline{x}. \quad (2.7)$$

The inverse of the deformation gradient reads

$$\underline{\mathbf{F}}^{-1} = \frac{\partial \underline{X}(\underline{x})}{\partial \underline{x}(t)} \quad \text{or} \quad F_{Ij}^{-1} = \frac{\partial X_I(\underline{X})}{\partial x_j} = X_{I,j}. \quad (2.8)$$

Using $\underline{\mathbf{F}}$, in addition to the deformation of an infinitesimal line element 2.5, it is possible to calculate the deformation of an infinitesimal area element $d\underline{A}$ and an infinitesimal volume element dv , reading

$$d\underline{a} = \underline{n} da = J \underline{\mathbf{F}}^{-1} \underline{N} dA = J \underline{\mathbf{F}}^{-1} d\underline{A}, \quad \text{and} \quad (2.9)$$

$$dv = \det \underline{\mathbf{F}} dv = J dv. \quad (2.10)$$

Where equation (2.9) is referred to as Nanson’s formula. The deformation gradient $\underline{\mathbf{F}}$

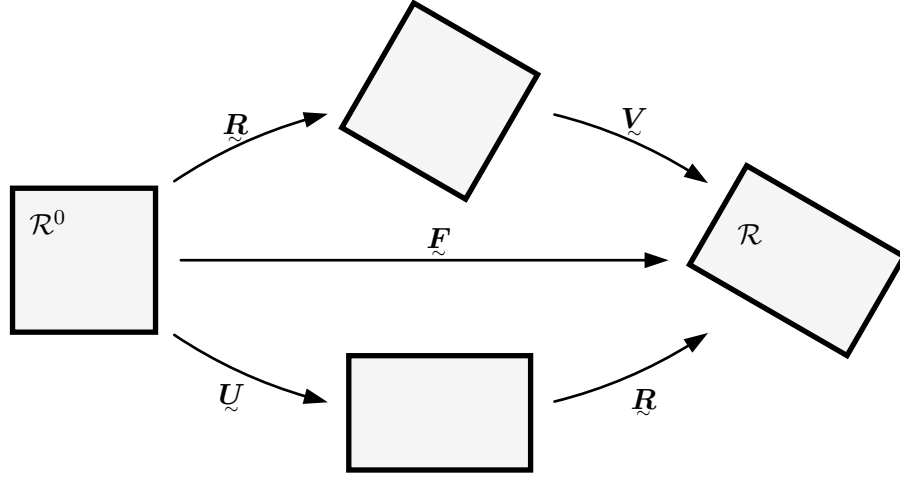


FIGURE 2.2: Using polar decomposition the deformation gradient $\tilde{\mathbf{F}}$ can be split up into a symmetric right stretch tensor $\tilde{\mathbf{U}}$ or a symmetric left stretch tensor $\tilde{\mathbf{V}}$ and a rotation tensor $\tilde{\mathbf{R}}$.

is positive definite, such that the transformation from \mathcal{R}^0 to \mathcal{R} is direction preserving. Assuming that no negative volumes appear, the Jacobi determinant J is positive definite

$$J = \det \tilde{\mathbf{F}} > 0. \quad (2.11)$$

If no deformation has occurred, the deformation gradient $\tilde{\mathbf{F}}$ is equal to the two field identity tensor $\tilde{\mathbf{I}} = \delta_{iJ}\underline{\mathbf{e}}_i \otimes \underline{\mathbf{E}}_J$, where δ_{iJ} denotes the Kroenecker symbol. In that case $\tilde{\mathbf{F}}$ maps a point in the reference configuration \mathcal{R}^0 to itself in the actual configuration \mathcal{R} : $\underline{\mathbf{x}} = \tilde{\mathbf{I}}\underline{\mathbf{X}}$. Further, the deformation gradient accounts for both rigid body rotation and stretching. It can be shown that $\tilde{\mathbf{F}}$ can be polar decomposed into a proper orthogonal rotation tensor $\tilde{\mathbf{R}}$, and either a symmetric left stretch tensor $\tilde{\mathbf{V}}$ or a symmetric right stretch tensor $\tilde{\mathbf{U}}$. See figure 2.2 for a schematic representation.

$$\tilde{\mathbf{F}} = \tilde{\mathbf{R}}\tilde{\mathbf{U}} = \tilde{\mathbf{V}}\tilde{\mathbf{R}} \quad (2.12)$$

As the rotation tensor $\tilde{\mathbf{R}}$ is proper orthogonal, $\tilde{\mathbf{R}}^\top \tilde{\mathbf{R}} = \tilde{\mathbf{I}}$ applies. In order to define strain measures, the rotation tensor is not of importance. This allows to define strain measures as functions of the left and the right stretch tensors, or as functions of multiplying the deformations gradient $\tilde{\mathbf{F}}$ with its transpose $\tilde{\mathbf{F}}^\top$, as the rotational part then cancels out. The right Cauchy-Green tensor is defined as

$$\tilde{\mathbf{C}} = \tilde{\mathbf{F}}^\top \tilde{\mathbf{F}} = \tilde{\mathbf{U}}\tilde{\mathbf{U}} = C_{IJ}\underline{\mathbf{E}}_I \otimes \underline{\mathbf{E}}_J \quad \text{or} \quad C_{IJ} = F_{kI}F_{kJ}. \quad (2.13)$$

A look at the right Cauchy-Green tensor shows that it is rooted in the reference configuration, or before the rotation $\tilde{\mathbf{R}}$ is applied. That means it describes the deformation in the undeformed state. The left Cauchy-Green tensor is defined as

$$\tilde{\mathbf{B}} = \tilde{\mathbf{F}}\tilde{\mathbf{F}}^\top = \tilde{\mathbf{V}}\tilde{\mathbf{V}} = B_{ij}\underline{\mathbf{e}}_i \otimes \underline{\mathbf{e}}_j \quad \text{or} \quad B_{ij} = F_{iK}F_{jK}. \quad (2.14)$$

Again, this tensor has its basis in the actual configuration, describing the deformation

in the deformed state, or after the rotation \mathbf{R} is applied (2.12). Both of the Cauchy-Green stretch tensors are symmetric and objective

$$\underline{\underline{C}}' = \underline{\underline{F}}'^{\top} \underline{\underline{F}}' = \underline{\underline{F}}^{\top} \underline{\underline{Q}}^{\top} \underline{\underline{Q}} \underline{\underline{F}} = \underline{\underline{F}}^{\top} \underline{\underline{F}} = \underline{\underline{C}}, \text{ and} \quad (2.15)$$

$$\underline{\underline{B}}' = \underline{\underline{F}}' \underline{\underline{F}}'^{\top} = \underline{\underline{Q}} \underline{\underline{B}} \underline{\underline{Q}}^{\top}, \quad (2.16)$$

where $\underline{\underline{Q}}$ is a transformation matrix. Common strain measures are the Green-Lagrange $\underline{\underline{E}}$ and the Euler-Almansi strain $\underline{\underline{\gamma}}$ tensor, which are based on the Green-Cauchy strain tensors

$$\underline{\underline{E}} = \frac{1}{2} (\underline{\underline{C}} - \underline{\underline{I}}), \quad (2.17)$$

$$\underline{\underline{\gamma}} = \frac{1}{2} (\underline{\underline{I}} - \underline{\underline{B}}^{-1}). \quad (2.18)$$

These strain tensors are commonly used to describe the deformation in a large or finite strain setting.

2.1.1 Linear theory

For a small or infinitesimal deformation it is useful to simplify the strain measures by linearizing. Let the displacement vector $\underline{\underline{u}} = u_i \underline{\underline{e}}_i = U_I \underline{\underline{E}}_I$ be the difference between the position of a particle in the reference and the current configuration

$$\underline{\underline{u}} = \underline{\underline{x}} - \underline{\underline{X}}. \quad (2.19)$$

By introducing a displacement gradient

$$\underline{\underline{H}} = \text{Grad} \underline{\underline{u}} = \underline{\underline{F}} - \underline{\underline{I}} \quad \text{or} \quad H_{iJ} = \frac{\partial u_i}{\partial X_J} = u_{i,J}, \quad (2.20)$$

the Green-Lagrange strain tensor can be expressed as

$$\underline{\underline{E}} = \frac{1}{2} \left(\underline{\underline{H}} + \underline{\underline{H}}^{\top} + \underline{\underline{H}}^{\top} \underline{\underline{H}} \right), \quad (2.21)$$

where the superscript $(\cdot)^{\top}$ denotes the transpose. The verbose notation of the Green-Lagrange strain tensor $\underline{\underline{E}}$ reads

$$E_{IJ} = \frac{1}{2} \left(\frac{\partial u_I}{\partial X_J} + \frac{\partial u_J}{\partial X_I} + \frac{\partial u_k}{\partial X_I} \frac{\partial u_k}{\partial X_J} \right). \quad (2.22)$$

In linear theory, the deformations are assumed to be small. Therefore, the displacement gradient is considered infinitesimal $H_{iJ} = u_{i,J} \rightarrow 0$, such that its square $u_{k,I} u_{k,J}$ is small of higher order. Using the basic kinematic relation $\underline{\underline{x}} = \underline{\underline{u}} + \underline{\underline{X}}$ (Eq. 2.19) the displacement gradient can be expressed

$$H_{iJ} = u_{i,J} = u_{i,k} x_{k,J} = u_{i,k} (\delta_{kJ} + u_{k,J}) \stackrel{\text{linear}}{=} u_{i,J}. \quad (2.23)$$

That means that in linear theory the material and the spatial derivative are equivalent, no distinction between the reference and the actual configuration is made. For instance, both the Green-Lagrange strain tensor $\underline{\underline{E}}$ and Euler-Almansi strain tensor

γ coincide in that case.

$$\underline{\varepsilon} = \underline{\mathbf{E}} \Big|_{\text{lin.}} = \underline{\gamma} \Big|_{\text{lin.}}, \text{ where } \varepsilon_{ij} = \frac{1}{2} (u_{i,j} + u_{j,i}) \quad (2.24)$$

The linearized or infinitesimal strain tensor $\underline{\varepsilon}$ is symmetric. Neglecting the distinction between the reference and the actual configuration from this point on, only small indices are used.

2.2 Balance Equations

Balance equations are fundamental to continuum mechanics, constituting the behavior of material continua. Here they are formulated in current configuration. Consider a field $q(t, \underline{x})$, which is distributed smoothly across a region \mathcal{R} in the material body \mathcal{B} with the outer boundary of the region $\partial\mathcal{R}$ and the corresponding outer normal vector \underline{n} . The field Q be may be a scalar, vector, tensor or a tensor of higher order, then let the field quantity be $Q(t) = \int_{\mathcal{R}} q(t, \underline{x}) dv$. The general form of the balance law is given by

$$\dot{Q}(t) = \frac{d}{dt} \left[\int_{\mathcal{R}} q(t, \underline{x}) dv \right] = \int_{\partial\mathcal{R}} \underline{q} \cdot \underline{n} da + \int_{\mathcal{R}} (p + s) dv, \quad (2.25)$$

relating the change $\dot{Q}(t)$ with the flux \underline{q} of a across the boundary $\partial\mathcal{R}$ into the region \mathcal{R} , the internal production p and the external source or sink s of the field quantity a .

2.2.1 Mass Conservation

The total mass m in a system is constant when assuming no flux of mass across the boundary, and with no internal volumetric production or external source. With ρ being the mass density the integral form of the mass balance over a material body \mathcal{R} is

$$\dot{m} = \frac{d}{dt} \int_{\mathcal{R}} \rho dv = 0. \quad (2.26)$$

Reynolds transport theorem relates the change of an integral quantity to the local change. Therefore the above mentioned mass balance can be rewritten by applying the material time derivative and subsequently the divergence theorem as

$$\frac{d}{dt} \int_{\mathcal{R}} \rho dv = \int_{\mathcal{R}} \left(\frac{d\rho}{dt} + \rho (\text{div } \underline{v}) \right) dv = 0, \quad (2.27)$$

where \underline{v} is the velocity. Since the control volume V can be chosen arbitrarily, the use of the localization theorem yields the local form of the mass balance

$$\frac{\partial \rho}{\partial t} + \rho (\text{div } \underline{v}) = 0, \quad (2.28)$$

which may be simplified further using the chain rule

$$\frac{\partial \rho}{\partial t} + \text{div}(\rho \underline{v}) = 0. \quad (2.29)$$

2.2.2 Linear and Angular Momentum Balance

Euler's balance laws of linear and angular momentum are essential for continuum mechanic calculations. The balance of linear momentum is analogous to Newton's second law of motion, stating that the change of a body's momentum is equal to the force acting on it. Consider a infinitesimal volume element dv with mass density ρ and the velocity \underline{v} . Assume two types of external forces, the contact force or traction \underline{t} per unit area which is acting on the boundary, and an external body force density \underline{f} per unit mass. The presence of a contact moment or body moment are neglected. Using the general form of the balance law in integral form, given in (2.25), the integral form of the linear momentum balance is established

$$\frac{d}{dt} \int_{\mathcal{R}} \underline{v} dm = \int_{\mathcal{R}} \underline{f} dm + \int_{\partial\mathcal{R}} \underline{t} da. \quad (2.30)$$

The rate of change of the momentum is equal to the flux of momentum or traction \underline{t} across the boundary ∂V and the external production \underline{f} . The local form of the linear momentum balance can be derived in the same matter as the local form of the mass balance with the use of Reynolds transport theorem. Additionally, applying the mass balance in the local form (2.28), another representation of the linear momentum balance is obtained

$$\int_{\mathcal{R}} \rho \underline{a} dv = \int_{\mathcal{R}} \rho \underline{f} + \int_{\mathcal{R}} \underline{t} da dv, \quad (2.31)$$

where the vector \underline{a} represents the acceleration. In a similar fashion, the angular momentum balance can be derived. Consider a volume element dv with an arbitrary location \underline{x} with a velocity \underline{v}

$$\frac{d}{dt} \int_{\mathcal{R}} \underline{x} \times \rho \underline{v} dv = \int_{\mathcal{R}} \underline{x} \times \rho \underline{f} dv + \int_{\partial\mathcal{R}} \underline{x} \times \underline{t} da. \quad (2.32)$$

The change of the angular momentum with respect to time is equal to the moment on the boundary of the region and within the region. Again, the above mentioned integral form of the angular momentum balance can be simplified by using Reynolds transport theorem and mass conservation (2.28)

$$\int_{\mathcal{R}} \underline{x} \times \rho \underline{a} dv = \int_{\mathcal{R}} \underline{x} \times \rho \underline{f} dv + \int_{\partial\mathcal{R}} \underline{x} \times \underline{t} da. \quad (2.33)$$

2.2.3 Stress

Until here, the kinematics, the motion of a body, its intrications in terms of deformation and balance equations have been discussed. So far, no assumption of the cause of this motion has been made. Here, the concept of stress is discussed. Figure 2.3 shows a region of a body with its volume \mathcal{R} cut in half. It is divided into two mutually disjoint subregions \mathcal{R}_1 and \mathcal{R}_2 that do not overlap, separated by an arbitrary smooth cut surface $\partial\mathcal{A}$. The boundary of the region \mathcal{R} is $\partial\mathcal{R}$, and it is made up of the outer boundaries of the subregions $\partial\mathcal{R}_1$ and $\partial\mathcal{R}_2$. In short, the following equations hold:

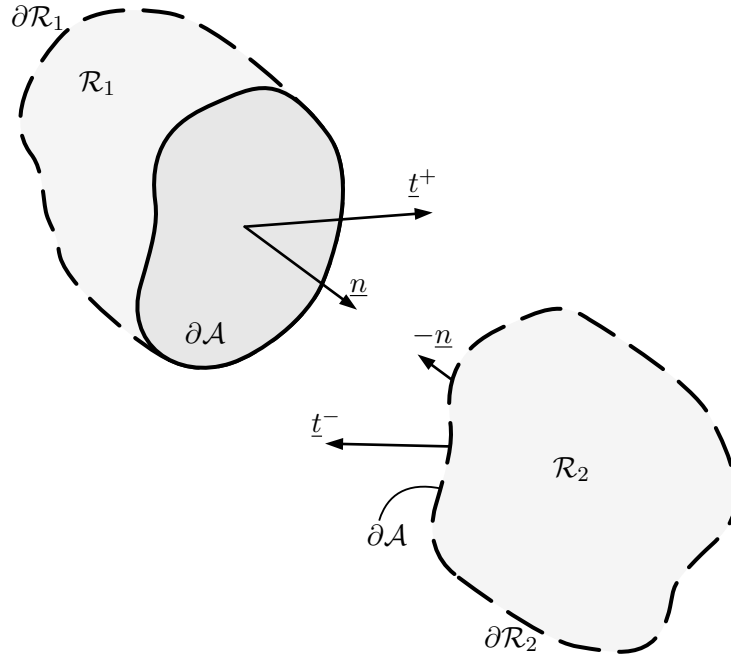


FIGURE 2.3: The region \mathcal{R} is split up into two parts, \mathcal{R}_1 and \mathcal{R}_2 . The cut surface ∂A is subject to the tractions \underline{t}^+ and \underline{t}^- .

$$\mathcal{R} = \mathcal{R}_1 \cup \mathcal{R}_2 \quad \text{and} \quad \mathcal{R}_1 \cap \mathcal{R}_2 = \emptyset, \quad (2.34)$$

$$\partial \mathcal{R}_1 = \partial \mathcal{R}_1^* \cup \partial A \quad \text{and} \quad \partial \mathcal{R}_1^* \cap \partial A = \emptyset, \quad (2.35)$$

$$\partial \mathcal{R}_2 = \partial \mathcal{R}_2^* \cup \partial A \quad \text{and} \quad \partial \mathcal{R}_2^* \cap \partial A = \emptyset, \quad (2.36)$$

$$\partial \mathcal{R} = (\partial \mathcal{R}_1 \cup \partial \mathcal{R}_2) / \partial A. \quad (2.37)$$

The boundary $\partial \mathcal{R}$ is subject to external traction and the region \mathcal{R} is subject to body forces. Corresponding points of the cut surface ∂A between the partial regions \mathcal{R}_1 and \mathcal{R}_2 have opposite normal vectors \underline{n} and $-\underline{n}$, respectively. The tractions \underline{t}^+ and \underline{t}^- are continuous on the cut surface ∂A . The linear momentum balance (2.31) holds for the region \mathcal{R} . Likewise the linear momentum balance holds for both subregions \mathcal{R}_1 and \mathcal{R}_2 . The difference of the linear momentum balance between the region \mathcal{R} and the sum of the subregions \mathcal{R}_1 and \mathcal{R}_2 lies in the surface integral of the tractions \underline{t}^- and \underline{t}^+ over the cut surface ∂A . The localization theorem yields Cauchy's lemma, which is equivalent to Newton's third law, stating that the tractions are opposed and of equal magnitude

$$\underline{t}^- = \underline{t}^+. \quad (2.38)$$

Consider a tetrahedron as shown in Figure 2.4. Three of its triangular surfaces A_1 , A_2 and A_3 lie within the x_1 , the x_2 and x_3 plane and are perpendicular to the corresponding axes. The inclined face A is subject to a surface traction \underline{t} , while the other triangular faces are subject to the surface tractions \underline{t}_1 , \underline{t}_2 , and \underline{t}_3 . Volumetric body forces \underline{f} may be present in the volume of the tetrahedron. Using Cauchy's lemma, the linear momentum balance is

$$\int_{\mathcal{R}} \underline{a} \rho dv = \int_{\mathcal{R}} \underline{f} \rho dv + \int_A \underline{t} da - \int_{A_1} \underline{t}_1 da - \int_{A_2} \underline{t}_2 da - \int_{A_3} \underline{t}_3 da. \quad (2.39)$$

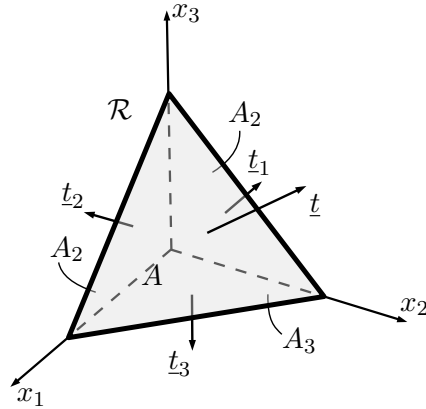


FIGURE 2.4: The Cauchy tetrahedron consists of the inclined face A subject to the surface traction \underline{t} and three faces A_i perpendicular to the respective coordinate axis x_i , subject to the surface tractions \underline{t}_i .

Let the tetrahedron shrink down to an infinitesimal volume. While the surface integrals decrease with the length scale squared, the volume integrals on the left side of the above equation decrease with the length scale cubed. Therefore volumetric and inertia forces may be neglected, leading to

$$\underline{t} = \frac{A_i}{A} \underline{t}_i. \quad (2.40)$$

Cauchy's integral theorem states that the traction vector \underline{t} can be related to the Cauchy stress tensor $\underline{\sigma}$ uniquely by projecting it into direction of the normal vector \underline{n} . In other words, the Cauchy stress tensor maps the normal vector of an infinitesimal area element da to the traction vector \underline{t}

$$\underline{t} = \underline{\sigma}^\top \underline{n}. \quad (2.41)$$

In order to identify the components of the Cauchy stress tensor $\underline{\sigma}$, it is useful to regard a infinitesimal cubic volume element with its faces oriented in the axis direction of the Cartesian coordinate system $\underline{e}_1, \underline{e}_2, \underline{e}_3$. The normal vectors of the faces coincide $\underline{n}_i = \underline{e}_i$ and the corresponding traction vectors are

$$\underline{t}_i = \underline{\sigma}^\top \underline{n}_i = \underline{\sigma}^\top \underline{e}_i. \quad (2.42)$$

where the components can be identified with

$$t_{ij} = \underline{\sigma}^\top \underline{e}_i \cdot \underline{e}_j = \sigma_{ij} \quad \text{and} \quad \underline{t}_i = \begin{bmatrix} \sigma_{i1} \\ \sigma_{i2} \\ \sigma_{i3} \end{bmatrix}. \quad (2.43)$$

This allows to represent the stress tensor in the form

$$\underline{\sigma} = \sigma_{ij} \underline{e}_i \otimes \underline{e}_j = \begin{bmatrix} \sigma_{11} & \sigma_{12} & \sigma_{13} \\ \sigma_{21} & \sigma_{22} & \sigma_{23} \\ \sigma_{31} & \sigma_{32} & \sigma_{33} \end{bmatrix}. \quad (2.44)$$

Using Cauchy's integral theorem on the traction vector \underline{t} (2.41), applying Greens identity on the boundary term, and with mass conservation established (2.28), the

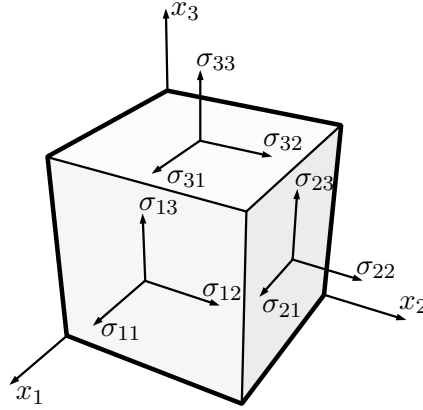


FIGURE 2.5: Infinitesimal volume element with components of the stress tensor $\underline{\sigma}$ on the positive faces

local form of the equilibrium balance in (2.31) can be expressed as

$$\rho \underline{a} = \rho \underline{f} + \operatorname{div} \underline{\sigma}. \quad (2.45)$$

In view of the linear momentum balance (2.31) and the localization theorem, the local form of the angular momentum balance of the Cauchy tetrahedron can be written with regard of Cauchy's integral theorem (2.41)

$$\underline{x}_{,i} \times \underline{t}_i = \underline{e}_i \times \left(\underline{\sigma}^\top \underline{e}_j \right) = \underline{0}. \quad (2.46)$$

The components σ_{ij} and σ_{ji} are equal and constitute the symmetry of the Cauchy stress tensor

$$\underline{\sigma} = \underline{\sigma}^\top. \quad (2.47)$$

3 Martensite Transformation

Iron and steels form crystal structures. That means they form an ordered crystal lattice. Allotropy is the occurrence of different physical manifestations tantamount to the crystal structure of a chemical material. The different crystal structures are allotropes, which exhibit different mechanical and chemical properties as shown by Yardley and Payton (2014), Kelly (2012), and Strangwood (2012). The different material properties are of importance in technical processes, including but not limited to, surface hardening (Brinksmeier, Garbrecht, and Meyer, 2008; Brinksmeier, Garbrecht, Meyer, and Dong, 2008), cryogenic turning (Aurich et al., 2014; Mayer, Skorupski, Smaga, Eifler, and Aurich, 2014), casting (Yamagata, 2005), and welding (Deng, 2009). Martensite is interesting for technical application as it remains the only nanostructured material that can be produced in bulk (Bhadeshia, 2017).

Martensite forms from the austenitic parent phase in a process called martensitic transformation. This transformation stands in contrast to diffusive processes, (Fick, 1855a; Fick, 1855b), such as the formation of ferrite, bainite and pearlite, which base the transformation on random particle movement and therefore change the makeup of the material locally (Bhadeshia, 2019). A diffusionless transformation is displacive due to small and orderly atom motion reordering atom bonds while retaining the chemical components. The martensitic transformation belongs to the latter. The atom movement is restricted to interatomic distances¹, resulting in a very fast transformation. Typical durations are in the order of magnitude 10^{-7} s. Modes of transformation can be grouped in ones, that do not change the shape and structure of the crystal, so called shuffle transformations, and those transformations, termed lattice-distortive which change the crystal lattice. The focus in this work lies on lattice-distortive transformations. They are not dominated by shuffles and induce a dilation (expansion or contraction) or a shear (Christian, Olson, and Cohen, 1995; Cohen, Olson, and Clapp, 1979). The martensitic transformation produces an eigenstrain due to the lattice mismatch, and can be induced by a combination of quenching and stress. Furthermore, dislocations introduced to the model can drive the nucleation of martensite (Zhang, Jin, and Khachaturyan, 2007; Olson and Cohen, 1986). The interested reader is referred to the works of Porter, Easterling, and Sherif (2009), Vvedensky (“Diffusionless transformations”), Banerjee and Mukhopadhyay (2010), and Bhadeshia (2017) for more information on the martensitic transformation.

In this work three effects of the formation of the martensite phase are of importance. First, the martensitic transformation distorts the lattice, resulting in a mismatch between the crystal lattice of the parent austenitic phase and the transformed martensitic phase. This mismatch can be described by the orientation relationship. Historically, the transformation mechanism proposed by Bain and Dunkirk, 1924 remains the case with the fewest possible ways of transformation. The arrangement of particles or atoms in a crystal lattice is typically described by the smallest non-repeating unit called the unit cell and the lattice parameters (West, 1999). Figure 3.1 depicts

¹distances smaller than the crystal constant

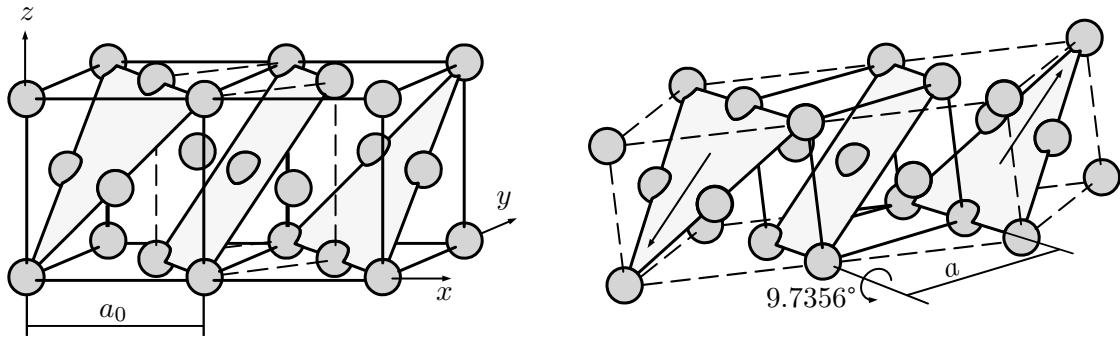


FIGURE 3.1: Two fcc unit cells contain a distorted bcc unit cell. The austenite lattice is depicted on the left. The bcc lattice after the martensitic transformation is depicted on the right. The Nishiyama-Wasserman OR is equivalent to transforming using the Bain OR and then applying a rotation of 9.7356° about the $[110]_{\text{fcc}}$ direction. The habit plane is drawn in grey. The Arrows indicate the direction of atom movement.

TABLE 3.1: Common orientation relationship

OR	plane	direction	var.	angle
Bain	$(001)_{\text{fcc}} \parallel (001)_{\text{bcc}}$	$[100]_{\text{fcc}} \parallel [110]_{\text{bcc}}$	3	-
NW	$(111)_{\text{fcc}} \parallel (110)_{\text{bcc}}$	$[110]_{\text{fcc}} \parallel [111]_{\text{bcc}}$	12	9.7356° about $[110]_{\text{fcc}}$
KS	$(111)_{\text{fcc}} \parallel (110)_{\text{bcc}}$	$[101]_{\text{fcc}} \parallel [001]_{\text{bcc}}$	24	9.7356° about $[110]_{\text{fcc}}$ and 5.2644° about $[111]_{\text{fcc}}$

two face-centered cubic (fcc) austenite cells, containing a distorted body-centered cubic (bcc) martensite cell. The Bain orientation relationship transforms from the austenitic to the martensitic phase by contraction in z -direction and expansion in x and y -direction, obtaining an undistorted bcc unit cell. Due to the symmetry, there are 3 possible ways of transforming. Even though being the case with the fewest ways of transformation, or orientation variants, the Bain orientation ship is not observed experimentally (Sandoval, Urbassek, and Entel, 2009; Kundu, Verma, and Sharma, 2012). Common orientation relationships have been identified for the transformation fcc to bcc. A comprehensive overview is given in Kelly (2012). Other orientation relationships include the Nishiyama-Wasserman (NW) (Nishiyama, 1934; Wassermann, 1935), the Kurdjumov-Sachs (KS) (Kurdjumov and Sachs, 1930), Greninger-Troiano (Greninger and Troiano, 1949) and the Headley-Brooks (Headley and Brooks, 2002). The mismatch can be described by matching preserved directions and planes in the fcc cell to those in the bcc cell. All orientation relationships can be derived by a full body rotation of the Bain orientation relationship, see, e.g., Koumatos and Muehlemann (2017), Wechsler, Lieberman, and Read (1953), Bowles and Mackenzie (1954), and Mackenzie and Bowles (1954). Table 3.1 shows common orientation relationships and their relation to one another.

Secondly, the martensitic transformation is driven by temperature. Quenching or rapid undercooling favors the martensitic phase. A characteristic variable is the martensite start temperature which strongly depends on the composition of the material. It can be observed experimentally or predicted using molecular dynamic simulations. Often weighted linear interpolation is employed when discussing the alloyed elements (Wang, Wolk, and Zwaag, 2000). The temperature dependency is typically

described with a chemical potential assumed to be proportional to a Landau polynomial.

Thirdly the martensitic transformation is influenced by stress. Nucleation can be both strain induced and stress assisted, which has been observed experimentally (Patel and Cohen, 1953). Dislocations and inhomogeneities can favor the martensitic transformation. The elastic energy is of importance here. Transforming from the austenitic to the martensitic phase can be energetically more stable. The combination of chemical and elastic potential is crucial for understanding this phase transformation (Olson and Cohen, 1976a; Olson and Cohen, 1976b; Olson and Cohen, 1976c).

3.1 Lattice Mismatch and Shape Strain

As discussed above the martensitic transformation leads to a lattice mismatch. The correspondence matches unrotated directions and planes before and after the transformation. The motion of single atoms is not tracked, rather the positions that correspond the untransformed lattice to the transformed one. While the presence of shuffles has to be admitted, they do not account for a shape change during the transformation and are therefore ignored (Christian, 1997). The lattice mismatch can be described by the Bain strain tensor (Koumatos and Muehleman, 2017; Wechsler, Lieberman, and Read, 1953). The Bain orientation relationship is obtained by assuming a so called least atom movement. Each atom in the austenitic lattice is matched with the closest atom in the martensitic lattice. The corresponding transformation matrices for the Bain orientation relationship read

$$\tilde{\mathbf{B}}_1 = \begin{bmatrix} \beta & 0 & 0 \\ 0 & \alpha & 0 \\ 0 & 0 & \alpha \end{bmatrix}, \tilde{\mathbf{B}}_2 = \begin{bmatrix} \alpha & 0 & 0 \\ 0 & \beta & 0 \\ 0 & 0 & \alpha \end{bmatrix}, \text{ and } \tilde{\mathbf{B}}_3 = \begin{bmatrix} \alpha & 0 & 0 \\ 0 & \alpha & 0 \\ 0 & 0 & \beta \end{bmatrix}, \quad (3.1)$$

where the parameters α and β are determined by the ratios of the lattice constants

$$\alpha = \sqrt{2} \frac{a}{a_0} \quad \text{and} \quad \beta = \frac{c}{a_0} = \frac{a}{a_0}. \quad (3.2)$$

In a more general case of a body centered tetragonal (bct) lattice, $c \geq a$. However, here the bcc lattice is considered, therefore $c = a$. The transformation for $\tilde{\mathbf{B}}_3$ can be derived by comparing lengths before the transformation in the fcc lattice to ones in the transformed bcc lattice (Figure 3.1). The z -direction is contracted by $\frac{a}{a_0}$. The edge in the $[100]_{\text{fcc}}$ -direction has the length a_0 and is transformed to the $[110]_{\text{bcc}}$ -direction with a length of $\sqrt{2}a$ thus obtaining α . Conversely, the $[110]_{\text{fcc}}$ -direction with a length of $\frac{\sqrt{2}}{2}a$ is transformed to the $[100]_{\text{fcc}}$ -direction. The three different transformation matrices $\tilde{\mathbf{B}}_i$ correspond to the three modes of transformation in the Bain model. In view of Equations (2.20), (2.21) and after linearizing according to Equation (2.23) the transformation strain tensor or eigenstrain for the Bain orientation relationship is obtained

$$\tilde{\mathbf{e}}_3^* = \begin{bmatrix} \sqrt{2} \frac{a}{a_0} - 1 & 0 & 0 \\ 0 & \sqrt{2} \frac{a}{a_0} - 1 & 0 \\ 0 & 0 & \frac{a-a_0}{a_0} \end{bmatrix}. \quad (3.3)$$

Analogously, the strain tensors $\underline{\xi}_1^*$ and $\underline{\xi}_2^*$ can be identified. Transformations within orientation relationships other than the Bain can be described by rotating the transformation matrices. They are of the form

$$\underline{T} = \underline{R}\underline{B}, \quad (3.4)$$

where \underline{R} is a proper rotation matrix. Considering the NW orientation relationship as an example (see Figure 3.1), the shear or gliding in $[112]_{\text{fcc}}$ direction in the $(111)_{\text{fcc}}$ habit plane corresponds to a rotation of 9.7356° about $[1\bar{1}0]$ after transforming with the Bain transformation tensor

$$\underline{T} = \underline{R}([1\bar{1}0], 9.7356^\circ)\underline{B}_3. \quad (3.5)$$

The circumstance above motivates the presence of an unrotated plane and an unrotated direction \underline{m} . More precisely, this planes normal \underline{n} maps onto itself

$$\lambda_n \underline{n} = \text{cof}(\underline{T}\underline{n}) \quad \text{and} \quad \lambda_m \underline{m} = \underline{T}\underline{m}. \quad (3.6)$$

Therefore, the vectors \underline{n} and \underline{m} are eigenvectors of the transformation and can be identified with the orientation relationship. Any transformation \underline{T} of the form given in equation (3.5) obtains the right crystal structure. Experimentally however, a conserved plane, the habit plane, is observed (Kim and Miyazaki, 2018). The shape strain \underline{S} within the habit plane is an invariant plane strain, consisting of an in-plane shear and a dilation (expansion or contraction) perpendicular to that plane as shown in Figure 3.2. The orientation, size and shape of the habit plane are conserved. While it is possible to transform a invariant plane strain \underline{S} with a rotation to a simple strain, the reverse is not true. The Bain transformation cannot be rotated to obtain a invariant plane strain \underline{S} . However, an invariant line strain can be obtained. Likewise, the macroscopic invariant plane strain \underline{S} obtains the wrong crystal structure when applied to the austenite lattice. Additionally, the habit plane and slip planes of austenite do not coincide in general.

Both the Wechsler-Lieberman-Read (WLR), and the Bowles-Mackenzie (BM) solve this discrepancy between the experimentally observed habit plane and the orientation relationship. They explain the presence of an invariant plane strain by applying a strain which is invariant to the crystal structure, a so called lattice invariant strain. Both theories are equivalent and constitute the phenomenological theory of martensite crystallography (PTMC) (Wechsler, Lieberman, and Read, 1953; Bowles and Mackenzie, 1954; Mackenzie and Bowles, 1954; Bilby and Christian, 1956; Ledbetter and Dunn, 2000). The WLR theory assumes a lattice invariant strain \underline{L} , which yields the invariant plane strain

$$\underline{S} = \underline{R}\underline{B}\underline{L}. \quad (3.7)$$

The BM theory assumes a homogeneous shape strain \underline{S} with a habit plane. Any vector within that plane is unrotated. An inhomogeneous invisible second shear \underline{H}^* is introduced that has to vanish when rotating the Bain strain tensor to account for the lattice deformations. As \underline{H}^* causes no observable change, the localized displacements have to counteract the shape change e.g. twinning and slip. The relation is given by

$$\underline{S}\underline{H}^* = \underline{R}\underline{B}. \quad (3.8)$$

Figure 3.3 sums up the relation between the invariant plane strain \underline{S} , the lattice correspondence $\underline{R}\underline{B}$ and the invisible shear \underline{H}^* of the BM theory and the lattice invariant

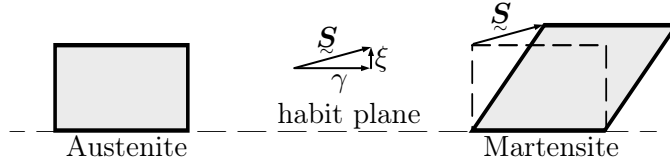


FIGURE 3.2: Rotated in plane view of the habit plane. The invariant plane strain \underline{S} consists of an in-plane shear γ and a dilation ξ perpendicular to the habit plane. During the MT the habit plane stays undistorted.

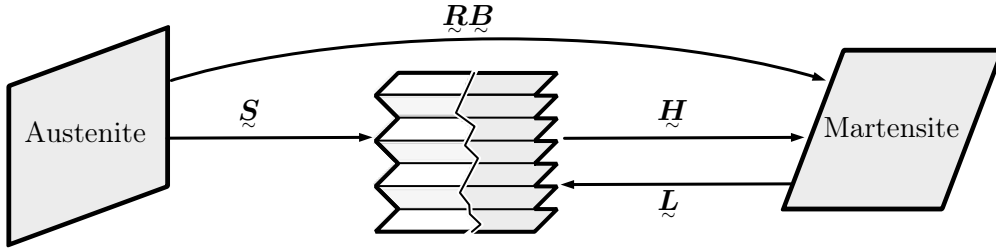


FIGURE 3.3: Applying \underline{RB} and the invariant plane strain \underline{S} to leads to a discrepancy in crystal structure (Martensite) and experimentally observed shape. The invisible shear \underline{H} and the lattice invariant strain \underline{L} close the gap and explain twinning and slip by introducing inhomogeneous displacements. Adapted from (Bhadeshia, 2017)

strain \underline{L} of the WLR theory. The correct shape is obtained by applying the invariant plane strain \underline{S} which is made up of the lattice correspondence \underline{RB} and a strain invariant to the lattice (the crystal structure is not changed) and therefore invisible when looking at the atom position without considering the atom motion by integer indexed lattice directions. The total strain is inhomogeneous as the mechanisms twinning and slip are predominantly observed. Simulations in two spatial dimensions require the transformation strain to be mapped to a plane. This can be done by considering the habit plane aligned with the planes normal and the shear perpendicular to that normal as shown in Figure 3.2. As the habit plane is undeformed and unrotated during the transformation plane strain is obtained. Every invariant plane strain can be transformed to a simple strain. In two dimensions, the inverse relation holds true: a simple strain can be transformed into an invariant plane strain. The invariant plane strain tensor can be expressed in its principal axis system according to Bhadeshia (2017) as

$$\underline{\epsilon}_S = \begin{bmatrix} \epsilon_1 & 0 & 0 \\ 0 & \epsilon_2 & 0 \\ 0 & 0 & 0 \end{bmatrix}, \text{ where } \epsilon_1 \geq 0 \text{ and } \epsilon_2 \leq 0. \quad (3.9)$$

Consider an invariant plane strain \underline{S} as described before. Chose a plane such that all deformations occur in that plane, for example as shown in Figure 3.2. The strain \underline{S} is now applied to an ellipsoid. In order to obtain a habit plane, a rotation is applied. This rotation is ambiguous, that means that two possible habit planes exist, obtaining two crystallographic twins.

In summary, the homogeneous Bain strain or any rotational variation therefrom explains the structural change from one lattice to the other, it is however not observed macroscopically. A combination of lattice invariant shear and twins can explain the invariant plane strain on the macro scale however.

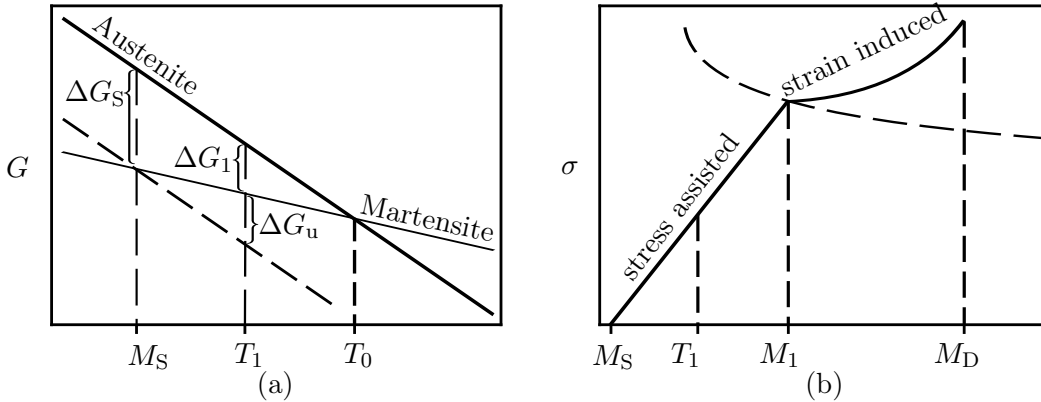


FIGURE 3.4: Gibbs free energy for the austenitic and the martensitic phases (a), Stress and strain inducing the martensitic transformation (b) according to Maalekian and Kozeschnik (2011)

3.2 Driving Forces

The martensitic transformation occurs because the martensitic phase is energetically more favorable. The energy landscape is defined by an interplay of the chemical and elastic potential. It is therefore possible to drive the transformation by both temperature, and stress or strain. Phenomenologically, there are four temperatures to characterize the martensitic transformation: The equilibrium temperature M_1 at which both phases are equally stable, and the martensite start temperature M_S at which the transformation is induced spontaneously, the martensite finish temperature M_F under which no further transformation happens, and a temperature M_D above which the chemical driving force is primarily causing the transformation. The martensitic transformation is athermal: The fraction of austenite transforming to martensite during cooling to a temperature below the martensite start temperature M_S is time independent (Maalekian and Kozeschnik, 2011). The characteristic temperatures depend on the chemical composition of the material (Kobasko, Aronov, Powell, and Vanas, 2009). The experimentally observed martensite finish temperature cannot be explained theoretically. For further reading the reader is referred to, e.g., Guggenheim (1993).

The Helmholtz free energy or simply free energy describes the amount of obtainable work, whereas the Gibbs free energy is the free enthalpy describing the amount of work that can be reversed at a constant temperature (Helmholtz, 1882; Gibbs, 1873). The Gibbs free energy takes the enthalpy into account. Typically, in the context of phase field modeling of the martensitic transformation, or in the context of martensitic transformations in general, those terms are used interchangeably. The work is thought to vanish, negating the difference between the Helmholtz and the Gibbs free energy at, e.g., constant pressure. In this work, to be precise, the terms free energy and chemical free energy are used in the same fashion as Gibbs free energy. The Gibbs free energy is crucial for the stability of phases in multi phase system. The diagram after Ellingham (1944) is useful to discuss the stability of the components making up this system. It shows the Gibbs free energy at a constant pressure in dependence of the temperature. They are a useful tool to predict equilibrium temperatures in, e.g., metallurgy.

Figure 3.4 (a) illustrates schematically the chemical free energy of the austenitic and martensitic bulk phases as a function of the temperature. The bulk energies of the

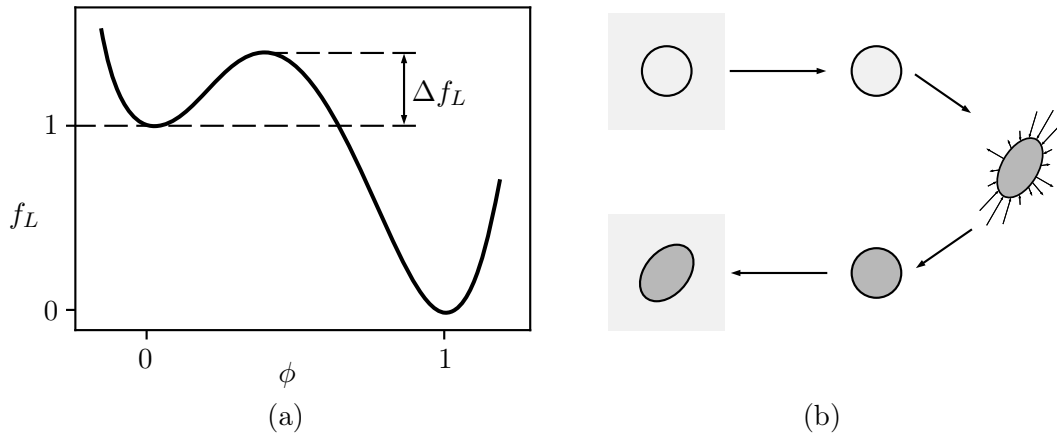


FIGURE 3.5: Normalized chemical energy (a) and Eshelby inclusion with parent matrix in light grey and transformed inclusion in dark grey, adapted from (Khachaturyan, 2013) (b)

austenitic and the martensitic phase are equal at the equilibrium temperature T_0 . However, martensite does not form spontaneously at temperatures below this equilibrium. It forms if the temperature falls below the martensite start temperature M_S . That is because the energy difference ΔG_S is high enough to overcome an activation energy, separating the bulk phases during the transformation. Both the austenitic and the martensitic phase are thought of as thermodynamically stable. Drawing a parallel to undercooled liquids, the austenite is in a metastable condition (Ishihara, Maeda, and Shingu, 1985). That means it is in an equilibrium state, however transformation to the martensitic phase minimizes the free energy globally. An aid in transforming is a mechanical energy contribution for example the elastic energy. It helps to overcome the activation energy such that transformations at temperatures T_1 above the martensite start temperature M_S and below the equilibrium temperature T_0 are possible. The energy difference ΔG_1 and the mechanically released energy ΔG_u add up to the energy difference ΔG_S at the martensite start temperature M_S .

Figure 3.4 (b) shows the temperature at which martensite starts to transform for different load states. At the martensite start temperature M_S , the martensitic transformation happens spontaneously. However, applying stress or strain, the temperature at which martensite forms can be increased considerably. Below M_1 , the stress required to start the martensitic transformation increases linearly with the temperature. In this region, the transformation is stress-assisted (Patel and Cohen, 1953). Martensite forms where stress is concentrated, such as grain boundaries, cracks, and other inhomogeneities. Above M_1 and below M_D , the martensitic transformation is strain induced. Plastic strain in the austenitic phase lowers the stress threshold for the martensitic transformation. The temperature M_D marks the point above which the chemical driving force is too small to allow for a transformation and the deformation occurs in the austenitic phase only.

The martensitic and the austenitic phase are the thermodynamically stable phases. A transformation from the austenitic to the martensitic phase can be modeled by, e.g., applying a transformation derived from the orientation relationship. Figure 3.5 (a) shows the chemical free energy in dependence of the state of the transformation. A transformation from the austenitic ($\phi = 0$) to the martensitic phase ($\phi = 1$) undergoes intermediate states ($0 < \phi < 1$). Those intermediate states arise from the positions the atoms occupy during the transformation while switching from the fcc atom lattice to

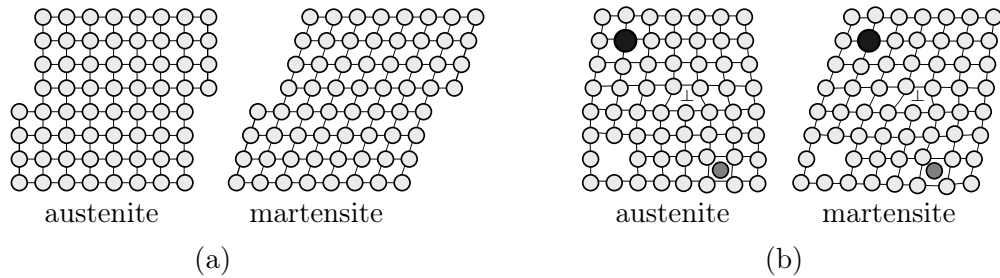


FIGURE 3.6: inheritance of plastic deformation (a), and crystallographic defects (b), such as vacancies, dislocations (\perp), interstitials (black), and antisites (dark grey) during the martensitic transformation.

the bcc atom lattice. In a modeling context, the transformation strain is interpolated and acts as a function of the order parameter ϕ indicating the state of the material. The way how the atoms move from the fcc to the bcc lattice can be characterized by, e.g., molecular dynamics simulations (Sandoval, Urbassek, and Entel, 2009; Song and Hoyt, 2012; Song and Hoyt, 2013). However, no matter how the atoms move, the intermediate atom positions represent energetically non stable states, such that the atoms eventually fall in the austenitic or the martensitic phase. Here, the austenitic phase is considered metastable. It is locally stable, however a transformation to the martensitic phase releases energy. The martensitic phase can be considered stable. The difference between the maximum and the metastable minimum is the activation energy Δf_L needed to trigger the martensitic transformation. This is in accordance with the Ellingham diagram discussed above and explains why the martensite start temperature M_S is considerably lower than the equilibrium temperature T_0 . The chemical free energy is temperature dependent (Schmidt, Dornisch, and Müller, 2017a; Schmidt et al., 2016; Wang and Khachaturyan, 1997).

In addition to the temperature aspect, another important driving force is the mechanical aspect. The martensitic transformation can be facilitated by applying a deformation to the work piece, thus leading to a stress assisted or strain induced transformation. Stress assisted means the activation energy is lowered by the mechanical energy as shown in Figure 3.4. Strain assisted means that plastic strain drives the transformation (Novelli, Maurel, Weiss, Grosdidier, and Bocher, 2017).

The Eshelby inclusion was first conceptualized and solved by Eshelby (1957). An ellipsoidal inclusion as shown in Figure 3.5 is transformed in order to introduce an inhomogeneity. The problem is depicted in Khachaturyan (2013). The resulting elastic field can be found by cutting the ellipsoid out of the surrounding matrix, then transforming it. The transformation is assumed to introduce a shape strain and a change of elastic constants. In order to re-insert it into the untransformed matrix after the transformation, stress has to be applied. After accommodating the ellipsoid back into the matrix and ensuring kinematic compatibility, it is relaxed. This leads to a deformation of both the matrix and the inclusion. The elastic field outside can be determined as well (Eshelby, 1959). The elastic energy of the ellipsoidal inclusion vanishes when a pure shape strain is applied (Kelly, 2006). The pure shape strain is tantamount to the existence of a habit plane. A further aspect are the different elastic constants of the austenitic and the martensitic phases (Persson, 2015). Martensite is stiffer and more brittle than austenite. Depending on the load situation, transforming to the martensitic phase can be energetically beneficial.

Plasticity is characterized by a permanent shape change. Typically an elastic threshold has to be passed, fulfilling a plastic yield criterion, in order for plastic deformation to occur. Figure 3.6 (a) shows a plastic deformation prior and after the transformation. The plasticity is retained and therefore inherited. Inhomogeneities are an other important factor of the martensitic transformation. A schematic representation of crystallographic defects is shown in Figure 3.6 (b). For example dislocations, interstitials, vacancies, and antisites persist throughout the transformation. That means the chemical composition is left unchanged and crystallographic defects remain.

Inheritance from the austenitic parent phase to the martensitic child phase is observed experimentally in, e.g., Li et al. (2016) and modeled theoretically in, e.g., Schmitt, Kuhn, and Müller (2017). In industry, the martensitic transformation is useful in the application of so called transformation induced plasticity (TRIP) steels. Metastable austenite is retained such that a sufficiently high deformation can trigger the martensitic transformation (Olson and Cohen, 1982). Twinning induced plasticity (TWIP) steels make use of the martensitic transformation as well. Given a high enough stacking fault energy to prevent an athermal martensitic transformation, a deformation of the TWIP steel induces crystallographic twins. Those twins are beneficial for the strength of the material (Cooman, Kwon, and Chin, 2012).

4 Phase Field Models

Phase field models are a versatile tool for a variety of interfacial problems, as they introduce a mathematical regularization of the sharp interface approach, scaling phase-dependent values with an additional degree of freedom, the order parameter (Qin and Bhadeshia, 2010). The order parameter is also referred to as phase field parameter. Phase field models are typically used to evolve structures. Possible scenarios include, but are not restricted to, the evolution of allotrope phases and phase transformations (Wang and Khachaturyan, 1997; Artemev, Wang, and Khachaturyan, 2000; Artemev, Jin, and Khachaturyan, 2001), solidification (Wang et al., 1993; Echebarria, Folch, Karma, and Plapp, 2004), the optimizing of material structures (Muench, Gierden, and Wagner, 2018), fracture (Kuhn and Müller, 2010; Miehe, Welschinger, and Hofacker, 2010), magnetic domains (Schrade, Mueller, Xu, and Gross, 2007; Dornisch, Schrade, Xu, Keip, and Müller, 2019; Nadgir, Dornisch, Müller, and Keip, 2019), and fluids (Diewald et al., 2018; Heida, 2013; Aihara, Takaki, and Takada, 2019). In contrast to sharp interface approaches, the domain is regularized by a smooth order parameter field, which is also called phase field. In the context of phase field modeling, the term phase is used synonymously with broken or unbroken materials, allotrope phases, and physical phases. Therefore, a phase represents a bulk domain with bulk properties and a material behavior unique to that phase. The interface is identified by intermediate values of the order parameter and thus by a presence of the gradient of the order parameter. This gradient can be used to define properties of the interface.

The order parameter is used to either classify or to quantify. Quantification occurs when e.g. liquid and vapor phases are present or in multi phase flows. Here the order parameter is tantamount to the concentration. In the case of solid-solid phase transformation or crack propagation the order parameter is used as a means of classification. Typically the order parameter is binary, thus identifying at most two phases, where the absence of one phase corresponds to the presence of another. Cases with a ternary order parameter are however possible (Schmitt, Kuhn, Müller, and Bhat-tacharya, 2014). A good review on phase field models is given by Steinbach (2009).

4.1 Multivariant Phase Field

A multivariant phase field is a phase field where a set of order parameters, e.g., a vector valued order parameter is used to identify a number of phases. This stands in contrast to a scalar value order parameter. Consider a scalar valued order parameter ϕ . The untransformed, or the parent phase is assumed if $\phi = 0$. A transformation to the child phase, or in this case the martensitic phase, is indicated if $\phi = 1$. One degree of freedom is used to identify two phases. Typically, the parent phase is described in dependence of the child phases. The absence of the child phase means the presence of the parent phase. In contrast to sharp interface models, the phase field presents a mathematical regularization by allowing interfacial values $0 < \phi < 1$, such that the order parameter ϕ is living on $[0, 1]$.

This allows the characterization of the energy density f as a function of the order parameter. However, as the model relies on energy minimization, a term dependent on the gradient is introduced. This so called gradient term widenes the interface. There are several ways of transforming from the austenitic parent phase to the martensitic child phases. The transformation strain introduced by the child phase can be identified by the orientation relationship. Therefore a vector valued order parameter is introduced

$$\underline{\phi} = \phi_\alpha \underline{e}_\alpha \in \mathbb{R}^n, \quad (4.1)$$

where Einstein summation convention applies. The vector \underline{e}_α is the basis vector. The index α identifies the phase or orientation variant and ranges from 1 to n , where n is the number of orientation variants. The components identify the state of the transformation. They are independent. If $\phi_\alpha = 1$ the child phase α is locally present, and if $\phi_\alpha = 0$ the phase α is locally absent. The admissible range of every component is $[0, 1]$, which is analogous to the scalar order parameter. However, the presence of two phases co-existing locally is not valid, as this would mean two transformation strains would have to be applied to the austenite lattice. An additional requirement has to be introduced. A dependent order parameter for the parent phases solves this issue. The order parameter ϕ_0 describes the presence of the parent phase. It is not a component of the vector valued order parameter $\underline{\phi}$, but it is defined by it

$$\phi_0 = 1 - \sum_{\alpha=1}^n \phi_\alpha. \quad (4.2)$$

Therefore, the sum of the components of the vector valued order parameter $\underline{\phi}$ plus the dependent order parameter ϕ_0 for the parent phase, or the sum of the order parameters ϕ_α for all phases $\alpha = 0 \dots n$ is constant

$$\phi_0 + \sum_{\alpha=1}^n \phi_\alpha = \sum_{\alpha=0}^n \phi_\alpha = 1. \quad (4.3)$$

The introduction of a vector valued order parameter simplifies the discussion in section 4.4. Using the basis vector and the null vector, the phases can be identified. The presence of the phase α can be written as

$$\underline{\phi} = \underline{e}_\alpha. \quad (4.4)$$

As stated above the parent phase is present when all other phases are absent, such that the vector valued order parameter becomes the null vector

$$\underline{\phi} = \underline{0}. \quad (4.5)$$

With this vector valued order parameter $\underline{\phi}$, the crystallographic state at any material point can be identified. A set of evolution equations (section 4.3) evolves each individual component ϕ_α . In the following chapters, a phase field model with a single martensitic variant (chapter 5) and a multivariant phase field model (chapter 6) are presented.

4.2 Energetic Setup

The phase field model relies on minimization of the total free energy as discussed above in section 3.2. For the chemical part of the problem, a chemical energy is introduced. This chemical energy is a function of the order parameter $\underline{\phi}$ and the temperature T . It therefore depends on the local chemical composition

$$f^{\text{ch}} = f^{\text{ch}}(\underline{\phi}, T). \quad (4.6)$$

With this potential, the stability of the phase is determined. The chemical energy strongly depends on the temperature, influencing the kinetics of the phase transformation and the stability of the phases (Schmidt, Dornisch, and Müller, 2017b). The chemical part of the model is coupled with the elastic energy. The elastic energy is a function of the order parameter $\underline{\phi}$, the elastic strain $\underline{\xi}^e$, and as thermal strain present in general, of the temperature T as well, reading

$$f^{\text{u}} = f^{\text{u}}(\underline{\xi}^e, \underline{\phi}, T). \quad (4.7)$$

Without further assumptions, it is not possible to determine either the chemical or the elastic energy. A possible choice for the chemical energy is a metastable double well potential as presented in chapter 5 of this work. The elastic energy depends on the choice of the homogenization method employed. Here, an interpolation of the effective material parameters, such as in the Khachaturyan model in chapter 5, is as viable as a homogenization of the elastic energy assuming a uniform strain across the individual phases, such as in the Voigt/Taylor model presented in chapter 6. However, further choices for either the chemical energy and the elastic energy exist. The interested reader is referred to the work of Ammar, Appolaire, Cailletaud, and Forest (2009) and Khachaturyan (2013).

Both the chemical and the elastic energy assume their respective bulk values within the phases. However their behavior in the interface region is not defined. In the case of the martensitic transformation, the chemical energy exhibits local minima for the bulk phase, ensuring stability for the bulk phases. That means that the chemical energy has to be at a maximum state in the interface region. Therefore minimizing the interface width would also minimize the free energy. In order to mitigate this, a gradient term is introduced. It attributes energy to the gradient of the phase field, therefore widening the interface

$$f^{\text{grad}} = f^{\text{grad}}(\nabla\phi_1, \dots, \nabla\phi_n) \propto \sum_{\alpha=1}^n (\nabla\phi_\alpha)^2. \quad (4.8)$$

Physically the combination of the chemical free energy and the gradient term constitute the interface energy. The free energy density is additively split up, consisting of the above mentioned chemical energy, the elastic energy, and the gradient term

$$f(\underline{\varepsilon}^e, \underline{\phi}, T) = f^{\text{ch}}(\underline{\phi}, T) + f^{\text{u}}(\underline{\varepsilon}^e, \underline{\phi}, T) + f^{\text{grad}}(\nabla\phi_1, \dots, \nabla\phi_n), \quad (4.9)$$

where the global free energy is given by

$$E = \int_V f dV. \quad (4.10)$$

The phase field model relies on minimization of the global free energy. Therefore the order parameter $\underline{\phi}$ has to evolve towards a minimum of the global free energy. Depending on the type of phase transformation there are a variety of suitable evolution equations, some of which are presented in the following section.

4.3 Evolution Equation

In a phase field model, evolution equations evolve the order parameter towards an equilibrium state. The evolution equations used can be chosen in dependence of the physical process underlying the phase transformation. The Allen-Cahn evolution equation (Allen and Cahn, 1979; Cahn and Allen, 1977) and the Cahn-Hilliard evolution equation (Cahn and Hilliard, 1958; Cahn, 1959) are reaction-diffusion equations. Using the Cahn-Hilliard equation, the order parameter is conserved over the domain, such that a balance law can be formulated (section 2.2). This equation models the process of spinoidal decomposition and has been applied, for example, to the cases of Oswald ripening (Fan, Chen, Chen, and Voorhees, 2002), topology optimization (Zhou and Wang, 2007), alloy solidification (Wheeler, Boettinger, and McFadden, 1993), and dendritic growth (Kobayashi, 1993). The order parameter in the Allen-Cahn equation is non-conserved, making it suitable for physical processes involving, for example, growth, relaxation and phase change. It has been applied for, e.g., the evolution of ferromagnetic domains (Choudhury, Li, Krill III, and Chen, 2005; Su and Landis, 2007; Wang and Zhang, 2013), crack growth (Schlüter, Willenbücher, Kuhn, and Müller, 2014; Kuhn and Müller, 2010), and phase transformations. In order to achieve a conserving behavior using the Allen-Cahn equation, a Lagrange multiplier can be introduced (Diewald et al., 2018). The Allen-Cahn equation is also known as the time dependent Ginzburg-Landau equation. Apart from the above mentioned evolution equations, in the case of magnetization evolution, the Landau-Lifshitz-Gilbert equation can be used (Jin, 2009).

Here, in the case of the martensitic transformation, the Allen-Cahn equation is chosen. In the works of Fried and Gurtin (1993) and Fried and Gurtin (1994), a generalized Ginzburg-Landau equation is derived based on the micro force balance (Gurtin, 1994). A good overview is given in Su and Landis (2007). Here, a scalar valued order parameter ϕ is assumed, without the loss of generality. Following Fried and Gurtin (1993), a vector stress $\underline{\xi}$ is introduced, acting on the rate $\dot{\phi}$. The expended power due to the change of the phase field in a subregion \mathcal{R} is equal to the power transferred over the boundary $\partial\mathcal{R}$, reading

$$\int_{\partial\mathcal{R}} \dot{\phi} \underline{\xi} \cdot \underline{n} dA = - \int_{\mathcal{R}} \pi dV. \quad (4.11)$$

Considering a constant ϕ for non-interface regions, the microforce balance can be formulated in integral form, reading

$$\int_{\partial\mathcal{R}} \underline{\xi} \cdot \underline{n} dA + \int_{\mathcal{R}} (\pi + \gamma) dV = 0. \quad (4.12)$$

The internal and external forces are represented by π and γ , respectively. With the microforce balance and the balance of linear and angular momentum in (2.31), the local form of the first law of thermodynamics reads

$$\int_{\mathcal{R}} \dot{e} = - \int_{\partial\mathcal{R}} \underline{q} \cdot \underline{n} dA + \int_{\mathcal{R}} r dV + \int_{\partial\mathcal{R}} \dot{\phi} \underline{\xi} \cdot \underline{n} dA + \int_{\mathcal{R}} \dot{\phi} \gamma dV + \int_{\mathcal{R}} \underline{\sigma} : \dot{\underline{\varepsilon}}_e dV. \quad (4.13)$$

The temperature is assumed to be constant, thus the heat flux \underline{q} , and the external heat supply r can be neglected. The free energy reads

$$f = e - TS, \quad (4.14)$$

where S is the entropy and e is the internal energy. The second law of thermodynamics reads

$$\int_{\mathcal{R}} T \dot{S} dV \geq - \int_{\partial\mathcal{R}} \underline{q} \cdot \underline{n} dA + \int_{\mathcal{R}} r dV \quad (4.15)$$

As the process is isothermal, the Clausius-Duhem inequality can be established. It reads, in local form

$$- \dot{f} - \gamma \dot{\phi} + \underline{\xi} \cdot \underline{\nabla} \phi + \underline{\sigma} : \dot{\underline{\varepsilon}}_e \geq 0. \quad (4.16)$$

The free energy is a function of the order parameter ϕ , its gradient $\underline{\nabla} \phi$ and the elastic strain $\underline{\varepsilon}_e$

$$f = f(\phi, \underline{\nabla} \phi, \underline{\varepsilon}_e). \quad (4.17)$$

Therefore, the total derivative yields

$$- \left(\gamma - \frac{\partial f}{\partial \phi} \right) \dot{\phi} + \left(\underline{\xi} - \frac{\partial f}{\partial (\underline{\nabla} \phi)} \right) \underline{\nabla} \dot{\phi} + \left(\underline{\sigma} - \frac{\partial f}{\partial \underline{\varepsilon}_e} \right) : \dot{\underline{\varepsilon}}_e \geq 0. \quad (4.18)$$

0 The equations of state can be identified using (4.18). The balance of linear and angular momentum holds. The field equation for the order parameter is the Allen-Cahn evolution equation

$$\dot{\phi} \propto \frac{\partial f}{\partial \phi} - \underline{\nabla} \cdot \left(\frac{\partial f}{\partial \underline{\nabla} \phi} \right). \quad (4.19)$$

The Gibbs free energy is modeled as a function of the order parameter $\underline{\phi}$. In the multivariant phase field the evolution equation is described component wise.

4.4 Interpolation

As mentioned above, phase field models rely on interpolating quantities across the interface. While a linear interpolation is sufficient in most cases, in some cases a linear interpolation yields wrong results or results in numerical instabilities. In this section different modes of interpolation are discussed and an example of how to interpolate correctly if using a multivariant phase field model is presented. Consider a quantity a which may be a scalar, vector, matrix, a tensor, or any quantity supporting scalar multiplication. This is an exception to the notation previously used. This quantity a

is generally dependent on the phase field, such that

$$a = a(\underline{\phi}). \quad (4.20)$$

The quantity can represent any parameter dependent on the state of the phase composition, including, but not limited to, chemical energy, mechanical energy, fluid density, elastic parameters, yield stress, material integrity, and transformation strain. A reasonable dependence can be found for some parameters. For example the chemical energy can be identified directly by the Gibbs free energy in molecular dynamics simulations, as can the fluid density (Diewald et al., 2018). It is either difficult or ambiguous to identify a function in dependence of the phase field for other parameters. Consider the martensitic transformation for example, where the phase field identifies the state of the transformation. In addition to the chemical energy, the elastic material parameters and the transformation strain have to be interpolated. The transformation strain can be identified by means of the orientation relationship (chapter 3), where the elastic material parameters for the bulk phases are determined (Persson, 2015). Using the PTMC it is not clear how the lattice mismatch can be described in the interface. Likewise, the determination of the elastic material parameters in this region is not feasible. However, any interpolation is required to assume the bulk values in the respective bulk phases

$$a(\underline{e}_\alpha) = a_\alpha, \quad (4.21)$$

where a is an arbitrary measure and a_α the value in the bulk phase α . Here, the idea is to use a scalar interpolation function h , with known first derivative h' and second order derivative h'' in order to construct a multivariant interpolation. Assume a scalar function $h \in \mathbb{R}$ which is continuous and smooth on $[0, 1]$, where

$$h(0) = 0 \quad \text{and} \quad h(1) = 1 \quad (4.22)$$

hold. Commonly, a linear interpolation function is used, however a cubic or a tangens hyperbolicus are further examples. They are given by

$$h_{\text{linear}}(\phi) = \phi, \quad (4.23)$$

$$h_{\text{cubic}}(\phi) = 3\phi^2 - 2\phi^3, \text{ and} \quad (4.24)$$

$$h_{\text{tanh}}(\phi) = \frac{1}{2} \tanh\left(\theta\left(\phi - \frac{1}{2}\right)\right) + \frac{1}{2}, \quad (4.25)$$

where it is shown easily that (4.22) holds. Numerical implementations often require first and second order derivatives with respect to the degrees of freedom, or in this case with respect to the degrees to the components of the order parameter. The function h can be used to construct an interpolation for the quantity a , dependent on the state of the chemical composition defined by the order parameter $\underline{\phi}$. In view of (4.21), a possible choice is the linear combination of the bulk phase values a_α , multiplied by a phase dependent interpolation function h_α , such that

$$a(\underline{\phi}) = \sum_{\alpha=0}^n h_\alpha(\underline{\phi}) a_\alpha. \quad (4.26)$$

Note, that the sum presented here ranges from $\alpha = 0 \dots n$, where a_0 represents the bulk value for the dependent parent phase (section 4.1). The phase dependent interpolation function h_α is 1, if $\underline{\phi}$ represents the corresponding phase α . If $\underline{\phi}$ represents

a phase β different from α , the phase dependent interpolation function h_α vanishes. This is related to (4.22) and can be expressed with

$$h_\alpha(\underline{e}_\beta) = \begin{cases} 1, & \text{if } \alpha = \beta \\ 0, & \text{otherwise.} \end{cases} \quad (4.27)$$

The behavior of h_α on the interface is yet to be determined. However, the choice of h_α is not trivial. In view of (4.22), a possibility is to define h_α analogously for all given phases $\alpha = 0 \dots n$ by using the same scalar interpolation function h and the identifier for the respective phase ϕ_α . The analogous approach reads

$$h_\alpha = h_\alpha^{\text{an}} = h(\phi_\alpha). \quad (4.28)$$

The interpolation function h_α for the respective phase is therefore dependent on the parameters for the specific phase ϕ_α , only. Furthermore, as there is no case dependency introduced, the implementation is straight forward. Here it is shown, that while this approach is present in many implementations, it is only valid for a certain number of phases or a linear interpolation function h . In the general case, this interpolation is unphysical and can lead to wrong solutions and numerical instabilities. An alternative is provided by introducing a case dependency, mitigating shortcomings of the approach presented above. The case dependent approach reads

$$h_\alpha(\underline{\phi}) = h_\alpha^{\text{if}}(\underline{\phi}) = \begin{cases} 1 - \sum_{\alpha=1}^n h(\phi_\alpha), & \text{if } \alpha = 0 \\ h(\phi_\alpha), & \text{if } \alpha > 0. \end{cases} \quad (4.29)$$

In the following, both approaches will be compared by considering a linear, a symmetric, and an arbitrary function h where (4.22) holds, while varying the numbers of phases present.

First, there is no restriction on the number of phases, and a linear interpolation function is assumed. In view of (4.28) and (4.29), it is sufficient to show that $h_0^{\text{if}} = h_0^{\text{an}}$. Recall equation (4.2), where the dependent order parameter for the parent phase is defined. In the case of a linear $h(\phi) = \phi$ the function can be rearranged

$$h_0^{\text{an}}(\underline{\phi}) = h(\phi_0) = h\left(1 - \sum_{\alpha=1}^n \phi_\alpha\right) \stackrel{h(\phi)=\phi}{=} h(1) - \sum_{\alpha=1}^n h(\phi_\alpha) \stackrel{(4.22)}{=} h_0^{\text{if}}(\underline{\phi}). \quad (4.30)$$

That means, if h^{if} is a valid choice, then h^{an} is valid as well for any number of phases present using a linear h .

Second, assume the presence of two phases only and a symmetric interpolation function h . A wide range of interpolation functions, for instance (4.23), (4.24), and (4.25), are point symmetric

$$h(\phi) = 1 - h(1 - \phi). \quad (4.31)$$

Considering two phases ($n = 1$), the interpolation function for the parent phase reads

$$h_0^{\text{an}}(\underline{\phi}) = h(\phi_0) = h\left(1 - \sum_{\alpha=1}^n \phi_\alpha\right) \stackrel{\text{symmetry}}{=} 1 - h\left(\sum_{\alpha=1}^n \phi_\alpha\right) \stackrel{n=2}{=} 1 - h(\phi_1) = h_0^{\text{if}}(\underline{\phi}). \quad (4.32)$$

Therefore both cases h^{an} and h^{if} are equivalent using a symmetric h with only two phases present. However, in general, the number of phases can be higher. Both cases differ for an arbitrary function h , even if assuming symmetry (4.31). This can

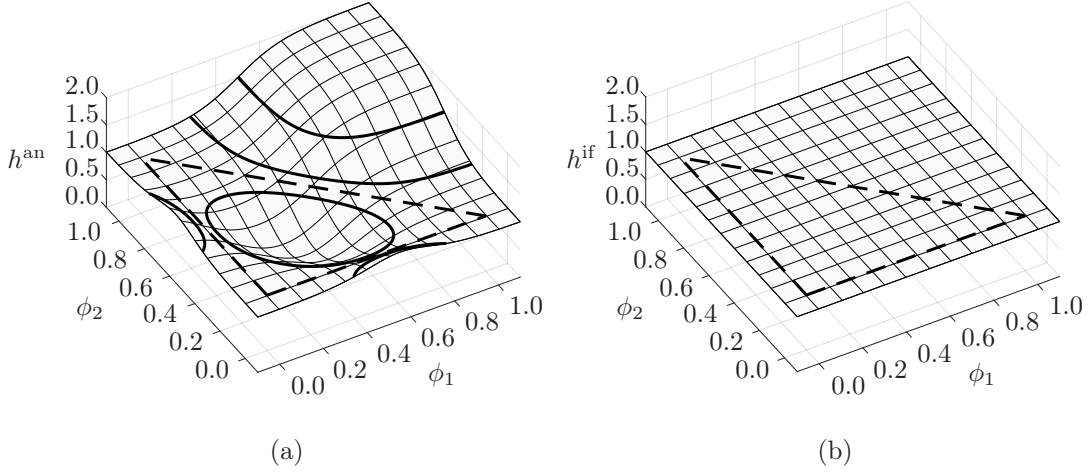


FIGURE 4.1: Comparison of the analogous interpolation approach h^{an} using a tanh interpolation, where $\theta = 5$ (a), and the case dependent interpolation approach h^{if} for any scalar interpolation function (b). The bulk values are constant, $a_\alpha = 1$. The dashed lines (-) indicate the boundary of the region where $\underline{\phi}$ is admissible. The thick lines are contour lines.

lead to mixtures exceeding bulk phase values such that drop-offs and local minima might occur. Thirdly, assume a system of n phases, with a non-linear interpolation function h . The validity of an interpolation function for a measure a will be discussed by the example of a three phase system, without loss of generality. Figure 4.1 shows the two interpolation methods, h^{an} and h^{if} for a system of three phases ($n = 2$). Here, the tanh interpolation using the analogous approach is compared to a case dependent interpolation. The bulk values are constant for all phases

$$a_\phi = 1. \quad (4.33)$$

The scalar interpolation function h chosen for the case dependent approach does not change the function shown in Figure 4.1 (b). For the sake of completeness, further examples are given in the appendix. The dashed lines indicate states where at most two phases are present. The presence of two phases α and β can be expressed mathematically with

$$\underline{\phi} = \underline{\phi}_{\alpha\beta} = \phi \underline{e}_\alpha + (1 - \phi) \underline{e}_\beta \quad , \text{ where } \phi \in [0, 1]. \quad (4.34)$$

Here, the parameter ϕ is the curve parameter. In view of equation (4.32), the equivalence of h^{an} and h^{if} can be shown for a system of n phases where locally at most two phases are present. This relation can be verified visually: both interpolation functions assume the value one when following the dashed lines where (4.34) holds

$$h^{\text{an}}(\underline{\phi}_{\alpha\beta}) = h^{\text{if}}(\underline{\phi}_{\alpha\beta}) \quad \text{for all } \alpha, \beta \in [0 \dots n]. \quad (4.35)$$

Considering (4.34) only, both interpolation methods are valid as they succeed to represent a constant value. This criterion is necessary for a valid interpolation, but not sufficient as Figure 4.1 (b) demonstrates. An interpolation should be able to represent a constant value for any valid $\underline{\phi}$. Coincidentally, the dashed lines mark the boundary of the triangle shaped area of an admissible order parameter $\underline{\phi}$. The analogous case h^{an} leads to a drop even if the order parameter moves within the valid range and even

TABLE 4.1: Applicability of the analogous and the case dependent approach for different number of phases. Where possible, literature references are provided. The x marks a successful calculation.

	$n = 2$		$n = 3$	
	h_{an}	h_{if}	h_{an}	h_{if}
h_{linear}	Schmitt, Müller, and Kuhn, 2012	$\equiv h_{\text{an}}$	Schmitt et al., 2013	$\equiv h_{\text{an}}$
h_{cubic}	x	x	wrong solution	x
h_{tanh}	Muench, Gierden, and Wagner, 2018	x	no convergence	x

though the symmetric, scalar interpolation function used here never exceeds the valid domain $[0, 1]$. A further downside is, that the choice of parameters effectively scales the drop as rearranging of (4.28) reveals

$$a^{\text{an}}(\underline{\phi}) = a_{\text{ct}} \sum_{\alpha=0}^n h_{\alpha}^{\text{an}}(\underline{\phi}). \quad (4.36)$$

This means for negative values a_{ct} minima are inverted to maxima, and vice versa, thus changing the stability. Therefore, depending on the given bulk phase values a_{ϕ} , $a(\underline{\phi})$ can be minimised by moving into the interface, or by exceeding the admissible range of $\underline{\phi}$. The case dependent interpolation function mitigates those problems, because the sum of all the individual interpolation functions h_{α}^{if} is one, reading

$$a^{\text{if}}(\underline{\phi}) = a_{\text{ct}} \sum_{\alpha=0}^n h_{\alpha}^{\text{if}}(\underline{\phi}) = a_{\text{ct}}. \quad (4.37)$$

To summarize, for the interpolation it is required that either

1. h is linear, or
2. at most two phases ($n < 2$) are present in the system at once, or
3. the sum of interpolation functions $h_{\alpha}(\underline{\phi})$ becomes one for all admissible $\underline{\phi}$.

Following from the latter, in addition to the sum of order parameters to be one (4.2), the partition of unity for the set of interpolation functions h_{α} has to hold

$$\sum_{\alpha=0}^n h_{\alpha}(\underline{\phi}) = 1. \quad (4.38)$$

The partition of unity is a concept employed in finite element modeling. Any ansatz function is bound to fulfill this criterion. In return, any set of ansatz functions can be used to construct a valid interpolation function. The partition holds automatically for any number of phases when using the case dependent interpolation approach h^{if} (4.37). It holds as well when using a linear interpolation function as a consequence of (4.30), or in view of (4.32) for at most two phases. Implementation wise both cases h^{if} and h^{an} coincide in the case of a linear h . Table 4.1 provides a summary of the two interpolation approaches presented here. Where possible, a literature reference is provided, otherwise, the test was conducted with the Voigt/Taylor homogenization phase field model presented in Chapter 6. In the case of a linear interpolation function, the two approaches are equivalent. They are successfully employed in, e.g., Schmitt,

Müller, and Kuhn (2012) and Schmitt, Müller, Kuhn, and Urbassek (2013a). A linear function, the case dependent approach h^{if} is equivalent to the analogous approach h^{an} . A tangens hyperbolicus interpolation is presented in Muench, Gierden, and Wagner (2018) for two phases present. A successful test using the Voigt/Taylor approach is marked with an x. In the case of three phases and a non-linear interpolation function, a correct solution is not obtained. In the case of a cubic interpolation function, convergence is obtained, however the solution is wrong. In the case of a tangens hyperbolicus interpolation function there is no convergence.

The linear interpolation function fails in the Voigt/Taylor approach, because its codomain is not limited, its first order derivative does not vanish in the bulk phases, and its second order derivative vanishes. A non vanishing first order derivative leads to a driving force. In combination with an unrestricted codomain this may lead to solutions outside the admissible range.

This behavior can be mitigated by using a non linear interpolation function with a non vanishing second order derivative, which either limits the functions codomain or with a vanishing first order derivative in the bulk phases. The cubic interpolation function fulfills the latter. Its first order derivative vanishes in the bulk phases

$$h'_{\text{cubic}}(\phi) = 0 \quad \text{for} \quad \phi = 0, 1. \quad (4.39)$$

Therefore no driving force appears in the bulk phases. The tangens hyperbolicus interpolation has a restricted codomain, given by

$$h_{\text{tanh}}(\phi) : \mathbb{R} \rightarrow [0, 1], \quad (4.40)$$

such that it stays within an admissible range. That means even if ϕ leaves its admissible range of $[0, 1]$, the interpolation h_{tanh} cannot assume inadmissible values. Using either of the interpolation functions, the problems of the linear interpolation can be mitigated. This, however, renders the implementation more complicated as this introduces a distinction between the case dependent and the analogous interpolation approach. The interested reader is referred to the appendix in 8.2, where more interpolation examples of the two approaches are presented.

5 A Temperature Dependent Separation Potential

As discussed in the previous chapters, the martensitic transformation is temperature dependent. The temperature dependency can be introduced by a temperature dependent separation potential. This potential is crucial for the formation of the martensitic phase. The martensitic phase is stable below the equilibrium temperature, but it does not form above the so called martensite start temperature. These features need to be represented by the separation potential. The separation potential is typically described using a Landau polynomial. Its parameters and their temperature dependence have been discussed in, e.g., Schmitt, Müller, and Kuhn (2012) and Urbassek and Sandoval (2012), such that here a function for the parameters is motivated and proposed. Using the Gibbs free energy obtained by molecular dynamics simulations, the parameters can be identified. As a consequence, the function yields the equilibrium temperature.

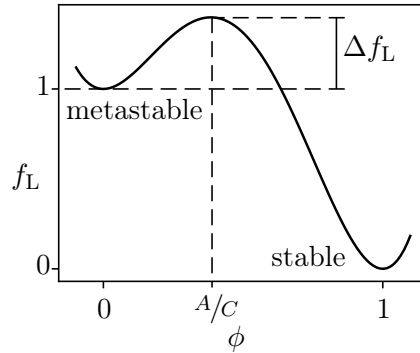


FIGURE 5.1: Landau polynomial where $A = 20$, $B = 72$, $C = 52$, and $D = 1$. The metastable ($\phi = 0$) and the stable phase ($\phi = 1$) are indicated for those parameters. The maximum is located at $\phi = \frac{A}{C}$.

5.1 Parameters of the Separation Potential

The separation potential, also termed chemical energy, is proportional to the Landau polynomial. It is crucial for the evolution of the order parameter

$$f^{\text{ch}}(\phi, T) = \frac{G}{L} f_L(\phi, T), \quad (5.1)$$

where G is the specific interface energy density. Here, a scalar valued order parameter is used, meaning one martensitic orientation variant is considered. The Landau polynomial is a function of the order parameter and the temperature. It is given by

$$f_L = \frac{A(T)}{2} \phi^2 - \frac{B(T)}{3} \phi^3 + \frac{C(T)}{4} \phi^4 + D(T). \quad (5.2)$$

The Landau polynomial is shown in Figure 5.1, where the parameters are $A = 20$, $B = 72$, $C = 52$, and $D = 1$. The Landau polynomial has a metastable and a stable minimum at $\phi = 0$ and $\phi = 1$, such that a transformation from the metastable to the stable minimum releases energy. The parameter D determines their location

$$D = \begin{cases} 1 & \text{if } \phi_{\min} = 1 \\ 0 & \text{if } \phi_{\min} = 0, \end{cases} \quad (5.3)$$

where ϕ_{\min} is the location of the stable minimum. Due to the location of the metastable minimum, the remaining parameters A , B , and C can be determined according to Yamanaka, Takaki, and Tomita (2008). The first derivative of the Landau polynomial reads

$$\frac{\partial f_L(\phi)}{\partial \phi} = f'_L(\phi) = A\phi - B\phi^2 + C\phi^3. \quad (5.4)$$

The second derivative can be used to determine if the extremal points are minima, maxima, or saddle points

$$\frac{\partial^2 f_L(\phi)}{\partial \phi^2} = f''_L(\phi) = A - 2B\phi + 3C\phi^2. \quad (5.5)$$

The derivative vanishes automatically for $\phi = 0$. The minimum at $\phi = 1$ can be achieved fulfilling the condition

$$f'_L(\phi = 1) = 0, \text{ yielding } C = B - A. \quad (5.6)$$

The Landau polynomial should be normalized, such that the difference between the stable and the metastable minimum becomes one. In view of (5.3), there are two different cases. The value for

$$f_L(\phi = 0) = D, \quad (5.7)$$

which is the stable minimum if D vanishes, and it is the metastable minimum of D is one. Therefore

$$f_L(\phi = 1) \stackrel{!}{=} 1 - D \quad (5.8)$$

should hold. Using (5.6), the parameter B can be determined.

$$B = 3A - 12 + 24D. \quad (5.9)$$

Thereby, the parameters B and C are dependent on A and D . The parameter D identifies the location of the stable and the metastable minimum. It can either be one or zero (5.7). In order to achieve a minimum, A needs to be positive. The magnitude of A scales the size of the global maximum. With the knowledge of the parameters A and D , the location of the global maximum and its height can be determined by solving

$$f'_L(\phi) = \phi(\phi - 1)(C\phi - A) \stackrel{!}{=} 0. \quad (5.10)$$

Therefore, the global maximum is located at $\phi = \frac{A}{C}$. Hence, the normalized energy barrier Δf_L , which has to be overcome in order to change from the metastable to the stable phase can be determined

$$\Delta f_L = f_L\left(\frac{A}{C}\right) - 1. \quad (5.11)$$

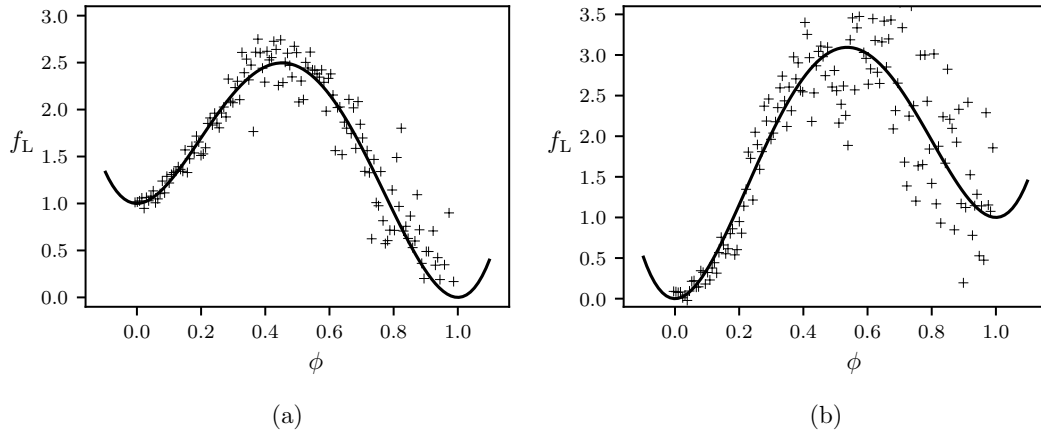


FIGURE 5.2: Landau polynomial (solid lines) and normalized free energy (+) from molecular dynamics simulations at $T = 700$ K (a) and $T = 900$ K (b) (Sandoval, Urbassek, and Entel, 2009).

5.1.1 Temperature Dependency

The parameters A , B , C , and D are temperature dependent as discussed, e.g., in Sandoval, Urbassek, and Entel (2009) or Schmidt et al. (2016). Parameter D influences which phase is stable and which phase is metastable. As lined out in chapter 3, martensite is stable below the equilibrium temperature T_0 . Conversely, above the equilibrium temperature, austenite becomes chemically stable. Figure 5.2 shows the Landau polynomial for a temperature $T = 700$ K and $T = 900$ K, where the pluses (+) indicate the normalized free energy obtained from molecular dynamics simulation of pure iron during phase transformation (Sandoval, Urbassek, and Entel, 2009). The free energy has been normalized such that the energy difference between the stable and the metastable phase is one.

Martensite is the stable phase for $T = 700$ K. Therewith, austenite is considered to be metastable. Therefore the temperature T is below the equilibrium temperature T_0 . The parameters can be fitted accordingly, for example

$$A(T = 700 \text{ K}) = 56.7504, \text{ and } D(T = 700 \text{ K}) = 1. \quad (5.12)$$

The remaining parameters B and C can be calculated according to (5.6) and (5.9). The energy barrier Δf_L increases when approaching the equilibrium temperature T_0 . For a temperature of $T = 700$ K, the dimensionless energy barrier is $\Delta f_L(T = 700 \text{ K}) = 2.4968$. The temperature $T = 900$ K in Figure 5.2 (b) is above the equilibrium temperature T_0 , as the martensitic phase is metastable and austenite is stable. Similarly, the parameters can be obtained

$$A(T = 900 \text{ K}) = 88.1414, \text{ and } D(T = 900 \text{ K}) = 1. \quad (5.13)$$

The parameter D specifies which phase is stable. Here, the Landau polynomial represents the normalized free energy, where the normalization is according to the energy difference between the stable and the metastable phase, such that

$$|f_L(0) - f_L(1)| = 1, \quad (5.14)$$

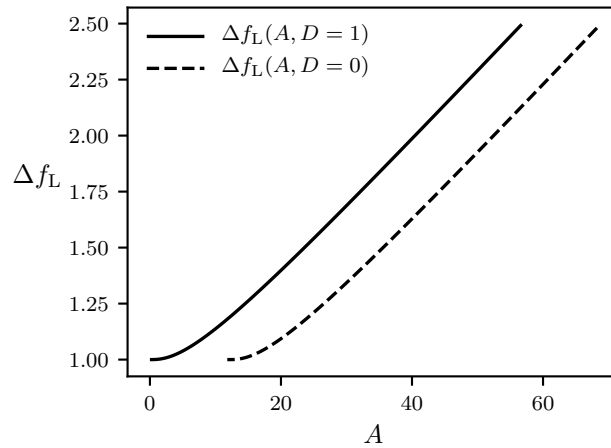


FIGURE 5.3: Energy barrier Δf_L as a function of A for $D = 1$ (solid line) and $D = 0$ (dashes, - -)

which can be achieved by either one of the conditions

$$(f_L(0) = 1 \wedge f_L(1) = 0) \quad \vee \quad (f_L(0) = 0 \wedge f_L(1) = 1). \quad (5.15)$$

Therefore, D has to be either one or zero, leading to the requirement in (5.7) with only assuming that f_L is normalized. With regard of the parameters in (5.12) and (5.13), a temperature dependent parameter D can be constructed

$$D(T) = \begin{cases} 1, & \text{if } T \leq T_0 \\ 0, & \text{if } T \geq T_0. \end{cases} \quad (5.16)$$

The parameter A directly influences the height of the energy barrier Δf_L for a constant D . Passing the equilibrium temperature T_0 , the parameter D changes from 1 to 0. This necessarily leads to a jump, as shown in Figure 5.3. While $\Delta f_L(A, D = 1)$ and $\Delta f_L(A, D = 0)$ are parallel for increasing A , their relative distance decreases, mitigating the influence of the jump in D

$$\lim_{A \rightarrow \infty} \frac{\Delta f_L(A, D = 1) - \Delta f_L(A, D = 0)}{\Delta f_L(A, D = 0)} \rightarrow 0. \quad (5.17)$$

In other terms, as A approaches infinity, so does the energy barrier without dependence on D , where

$$\lim_{A \rightarrow \infty} \Delta f_L \rightarrow \infty. \quad (5.18)$$

This leaves room for a discontinuous change of D , without affecting the Landau polynomial. Considering the previously discussed equations, a function $A(T)$ with the following assumptions is proposed

1. At a temperature $T = 0$ K, the parameter A is assumed to be zero, because the molecular dynamic simulations suggest it. With

$$A(T = 0) = 0, \quad (5.19)$$

the energy barrier vanishes (Figure 5.3), leading to a considerably fast transformation speed. As the temperature region in proximity of absolute zero are not of interest in this model, this behavior is ignored.

2. Conveniently, and due to sparse data above the equilibrium temperature T_0 , the parameter A is assumed to be symmetric, e.g.,

$$A(T_0 - T) = A(T_0 + T). \quad (5.20)$$

3. The parameter A goes to infinity approaching the equilibrium temperature T_0 (5.21), ensuring that no transformation takes place while simultaneously allowing the parameter D to change from 1 to 0 in view of (5.18). The following condition is imposed on the parameter A as it approaches the equilibrium temperature T_0 from either side

$$\lim_{T \rightarrow T_0^\pm} A(T) \rightarrow \infty. \quad (5.21)$$

Considering (5.19), (5.19), and (5.21), a possible choice for the function A is

$$A(T) = \theta \frac{T(2T_0 - T)}{|T_0 - T|^\gamma}, \quad (5.22)$$

where γ controls the curvature, and θ is a scaling factor. Note that the equilibrium temperature is not assumed here, but it drops out as a result when fitting $A(T)$ to values from the molecular dynamics simulations. The curvature γ influences the behavior of A exponentially. Already small changes in γ lead to big changes in A . It is therefore useful to choose the scaling factor θ such that it cancels out changes due to γ for an arbitrary temperature T_{fix}

$$\theta = \hat{\theta} |T_0 - T_{\text{fix}}|^\gamma, \quad (5.23)$$

where $\hat{\theta}$ is the adjusted scaling factor. Furthermore, this mitigates the unit problem of θ , simplifying (5.22) to

$$A(T) = \hat{\theta} T (2T_0 - T) \left(\frac{|T_0 - T_{\text{fix}}|}{|T_0 - T|} \right)^\gamma, \quad (5.24)$$

where $\hat{\theta}$ is dimensionless. Figure 5.4 shows the function A for different curvatures γ . Since the scaling factor is chosen in dependence of the curvature, the function does not vary for the temperature T_{fix} . Additionally, it exhibits a pole at T_0 , allowing for a change of the parameter D .

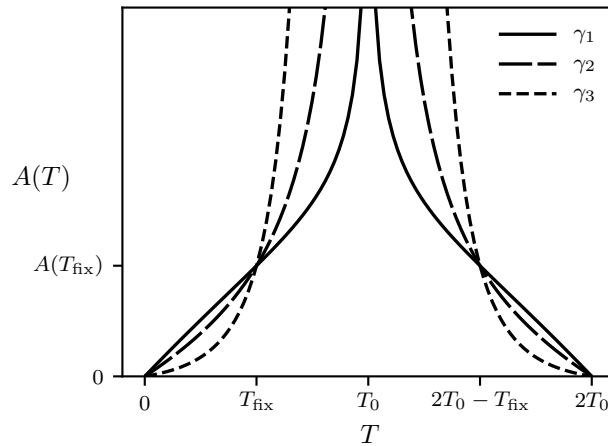


FIGURE 5.4: Parameter A as a function of the temperature T for varying curvatures where $\gamma_1 \leq \gamma_2 \leq \gamma_3$ according to (5.24)

5.1.2 Parameter Identification

In order to choose the parameters $\hat{\theta}$, γ , and T_0 properly, values for $A(T)$ are required. A molecular dynamics simulation provides the chemical energy at the temperatures $T = 100$ K, 300 K, 500 K, 700 K, 900 K, and 1300 K. As a first step, for each temperature, a sixth order polynomial has been fitted to the chemical free energy of the molecular dynamics simulation using the method of least squares, because it is the smallest order polynomial that approximates the data sufficiently well. The derivative of the polynomial yields the extremum points, its minima, and its maximum, as well as the energy barrier Δf_L . The energy difference in the stable and the metastable minima are used to normalize chemical free energy. Thereby, the molecular dynamics simulation can be fitted to the independent parameters A and D . As the relation between the stable and the metastable minimum is known, D is easily determined according to (5.16). The parameter A influences the height of the energy barrier Δf_L , and subsequently its location $\phi_{\max} = \frac{A}{C}$. Either one of those measures can be used to determine the remaining parameter A . With the addition of the method of least squares, this leads to three different methods to determine A for each given temperature:

1. using the location of the maximum $\phi_{\max} = \frac{A}{C}$ as given, yielding $A_{\phi_{\max}}$,
2. using the height of the energy barrier Δf_L as given, yielding $A_{\Delta f_L}$, or
3. the method of least squares, yielding A_{lsq} .

Keep in mind, while the first two methods seem to incorporate only one characteristic value of the molecular dynamics simulation, they have been determined after fitting a sixth order polynomial first. This is needed for the normalization. The implementation of the ϕ_{\max} method is straight forward. With parameter D already known, and the location of the maximum ϕ_{\max} obtained from the normalized chemical free energy, parameter A drops out directly using (5.6) and (5.11), yielding

$$A_{\phi_{\max}} = \phi_{\max} \frac{24D - 12}{1 - 2\phi_{\max}}. \quad (5.25)$$

TABLE 5.1: Parameter A over temperature T for different interpolation methods

T	0 K	100 K	300 K	500 K	600 K	700 K	900 K	1300 K
A_{lsq}	0.544	5.366	10.942	19.753	31.537	57.054	88.149	12.096
$A_{\Delta f_L}$	0.244	3.296	8.743	18.748	31.105	57.167	88.486	11.718
$A_{\phi_{\text{max}}}$	0	2.981	11.844	20.675	30.980	59.716	73.602	12.000

Using the energy barrier Δf_L as given is more difficult. In view of (5.11), the equation

$$A_{\Delta f_L} = f^{-1}(\Delta f_L + 1) \frac{D - 12}{1 - 2f^{-1}(\Delta f_L + 1)}. \quad (5.26)$$

requires to invert the Landau polynomial in order to find A . This is rather impractical as the inverse exists only for part of the functions domain. Implementation wise, the relation is represented as

$$R(A_{\Delta f_L}) = f_L \left(\frac{A_{\Delta f_L}}{C(A_{\Delta f_L})} \right) - \Delta f - 1 \stackrel{!}{=} 0, \quad (5.27)$$

where R denotes a residuum. It can be minimized using bisection. Consider two values $A_{i\Delta f_L}^+$, and $A_{i\Delta f_L}^-$, where

$$R(A_{i\Delta f_L}^+) > 0, \quad \text{and} \quad R(A_{i\Delta f_L}^-) < 0, \quad (5.28)$$

A new value $A_{i\Delta f_L}^\pm$ on the interval $I_i = (A_{i\Delta f_L}^-, A_{i\Delta f_L}^+)$ is arbitrary. The sign of residuum of this new value defines another interval

$$I_{i+1} = \begin{cases} (A_{i\Delta f_L}^-, A_{i\Delta f_L}^\pm), & \text{if } R(A_{i\Delta f_L}^\pm) > 0 \\ (A_{i\Delta f_L}^\pm, A_{i\Delta f_L}^+), & \text{if } R(A_{i\Delta f_L}^\pm) \leq 0, \end{cases} \quad (5.29)$$

leading to increasingly smaller intervals as i increases. In this implementation, $A_{i\Delta f_L}^\pm$ is determined using the bisection method

$$A_{i\Delta f_L}^\pm = \frac{A_{i\Delta f_L}^+ - A_{i\Delta f_L}^-}{2}. \quad (5.30)$$

Therefore the residuum R , a measure for the error in $A_{\Delta f_L}$, converges quadratically.

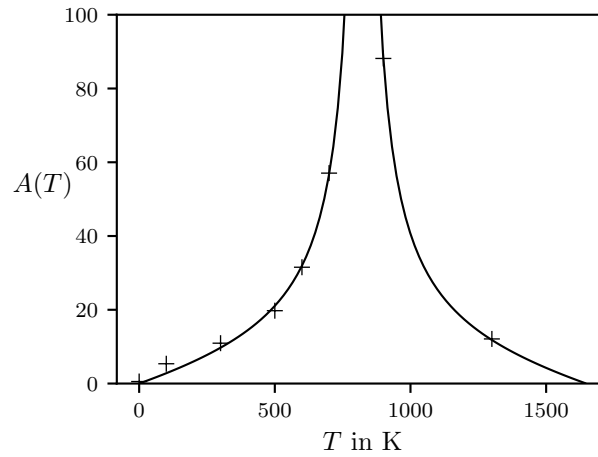
The third fitting method uses the method of least squares on the normalized chemical free energy. It relies on minimizing the squared residuals for all data points deviating from a model function. The interested reader is referred to the original work of Gauss (1823). In view of (5.2), (5.6), and (5.9), the model function can be expressed in the form

$$f_L(\phi) = A_{\text{lsq}} \left(\frac{1}{2}\phi^2 - \phi^3 + \frac{1}{2}\phi^4 \right) + D + (24D - 12) \left(\frac{1}{4}\phi^4 - \frac{1}{3}\phi^3 \right). \quad (5.31)$$

With the knowledge of parameter D , the only model parameter yet to determine is A_{lsq} . Table 5.1 is a summary of the parameter A applying the different fitting methods outlined above. The difference in the fitting methods is marginal. Each data set is a good fit. One may choose between these three data sets in order to determine the parameters of the function $A(T)$ described in 5.24.

TABLE 5.2: Parameters γ , $\hat{\theta}$ and T_0 determined using the method of least squares

	γ	$\hat{\theta} \cdot 10^2$	T_0 in K
start	0.8	0.8	800
lower limit	0.1	0.1	700
upper limit	2.0	2.0	900
fit	0.8799	1.0321	823.748

FIGURE 5.5: Parameter A as a function of T (solid line) fitted to value pairs (T, A_{lsq}) in Table 5.1 (+)

The data pairs (T, A_{lsq}) in Table 5.1 have been used to determine the parameters of the function in (5.24). The scaling factor is chosen in dependence of γ (5.23), where the difference $|T_0 - T_{\text{fix}}|$ is held constant

$$|T_0 - T_{\text{fix}}| = 100 \text{ K}. \quad (5.32)$$

The model parameters are the adjusted scaling factor $\hat{\theta}$, the curvature γ , and the equilibrium temperature T_0 . That means, as a result, the equilibrium temperature is obtained. Conversely, if assuming an equilibrium temperature a priori, it has to lie between 700 K and 900 K, as the parameter D changes from 1 to 0 (5.7). Here, the method of least squares is used to fit the function. Table 5.2 displays the starting values, the lower and upper limit, and the result for the fit. Hence, the chemical potential is a function of both the order parameter ϕ and the temperature T . Figure 5.5 shows the graph for A as a function of the temperature T . The function is in good agreement with the value pairs (T, A_{lsq}) .

5.2 Model Equations

Following the work of Schmitt, Müller, and Kuhn (2012), the model has been implemented in the finite element framework FEAP in two spatial dimensions. The above mentioned temperature dependent chemical energy f^{ch} is used to describe the chemical driving force of the phase field model. For the mechanical part, small strain elasticity is used, where the effective material parameters, the transformation strain $\underline{\underline{\boldsymbol{\varepsilon}}^*}$ and the elastic constants $\underline{\underline{\boldsymbol{C}}}$ are interpolated linearly

$$\underline{\underline{\boldsymbol{\varepsilon}}^*}(\phi) = \phi \underline{\underline{\boldsymbol{\varepsilon}}_1^*}, \quad \text{and} \quad \underline{\underline{\boldsymbol{C}}}(\phi) = \underline{\underline{\boldsymbol{C}}}_0 + \phi \left(\underline{\underline{\boldsymbol{C}}}_1 - \underline{\underline{\boldsymbol{C}}}_0 \right). \quad (5.33)$$

Therewith, the elastic strain and the elastic energy can be calculated, reading

$$\underline{\underline{\boldsymbol{\varepsilon}}^e} = \underline{\underline{\boldsymbol{\varepsilon}}}(\underline{\boldsymbol{u}}) - \underline{\underline{\boldsymbol{\varepsilon}}^*}(\phi), \quad \text{and} \quad f^{\text{u}} = \frac{1}{2} \underline{\underline{\boldsymbol{\varepsilon}}^e}(\underline{\boldsymbol{u}}, \phi) : \underline{\underline{\boldsymbol{C}}}(\phi) : \underline{\underline{\boldsymbol{\varepsilon}}^e}(\underline{\boldsymbol{u}}, \phi), \quad (5.34)$$

respectively. The infinitesimal strain tensor is determined according to (2.18). The material law is given by

$$\underline{\underline{\boldsymbol{\sigma}}} = \frac{\partial f^{\text{u}}}{\partial \underline{\underline{\boldsymbol{\varepsilon}}}} = \underline{\underline{\boldsymbol{C}}} \underline{\underline{\boldsymbol{\varepsilon}}^e} \quad (5.35)$$

The energy is additively split up

$$f = f^{\text{u}}(\underline{\underline{\boldsymbol{\varepsilon}}}, \phi) + f^{\text{ch}}(\phi) + f^{\text{grad}}(\underline{\nabla}\phi), \quad \text{where} \quad f^{\text{grad}}(\underline{\nabla}\phi) = \frac{1}{2} GL |\underline{\nabla}\phi|^2. \quad (5.36)$$

The field equations read

$$\underline{\nabla} \cdot \underline{\underline{\boldsymbol{\sigma}}} = \underline{\mathbf{0}}, \quad \text{and} \quad (5.37)$$

$$\frac{1}{M} \dot{\phi} + \frac{\partial f^{\text{u}}}{\partial \phi} + \frac{\partial f^{\text{ch}}}{\partial \phi} - \underline{\nabla} \cdot \frac{\partial f^{\text{grad}}}{\partial \underline{\nabla}\phi} = 0. \quad (5.38)$$

The elastic energy f^{ch} is proportional to the Landau polynomial given in (5.1).

5.3 Implementation

Applying the flux-divergence and using Green's identity, the weak forms can be determined

$$\int_V (\nabla \otimes \eta_{\underline{u}}) : \underline{\sigma} dV = \int_{\partial V} \eta_{\underline{u}} \cdot (\underline{\sigma} \underline{n}) dV_t, \quad (5.39)$$

$$\int_V \frac{1}{M} \dot{\phi} \eta_\phi + \frac{\partial f^u}{\partial \phi} \eta_\phi + \frac{\partial f^{\text{ch}}}{\partial \phi} \eta_\phi + (\underline{\nabla} \phi) \cdot (\underline{\nabla} \eta_\phi) dV = \int_{\partial V} \eta_\phi (\underline{\nabla} \cdot \underline{n}) dV_q. \quad (5.40)$$

The outer normal vector is \underline{n} . The test functions are denoted by $\eta_{\underline{u}}$ and η_ϕ . The discretizations for the phase field ϕ and the displacements \underline{u} are

$$\underline{u}^h = \sum_{I=1}^N N_I \hat{\underline{u}}_I, \quad \text{and} \quad \phi^h = \sum_{I=1}^N N_I \hat{\phi}_I, \quad (5.41)$$

where N is the number of element nodes, I is the nodal index, and N_I is the ansatz function. Discretized quantities are denoted with a superscript h (\cdot^h), and nodal quantities with a superset hat ($\hat{\cdot}_I$). The discretizations for the strain tensor and the gradient of the phase field read

$$\underline{\varepsilon}^h = \sum_{I=1}^N \underline{\mathbf{B}}_I^u \cdot \hat{\underline{u}}_I, \quad \text{and} \quad \underline{\nabla}^h \phi = \sum_{I=1}^N \underline{\mathbf{B}}_I^\phi \hat{\phi}_I, \quad (5.42)$$

where $\underline{\varepsilon}$ is the strain in Voigt notation. The matrices in two dimensions read

$$\underline{\mathbf{B}}_I^u = \begin{bmatrix} N_{I,1} & 0 \\ 0 & N_{I,2} \\ N_{I,2} & N_{I,1} \end{bmatrix} \quad \text{and} \quad \underline{\mathbf{B}}_I^\phi = \underline{\nabla} N_I. \quad (5.43)$$

5.3.1 Residual and Elemental Stiffness Matrix

The nodal residual vector and the elemental tangent matrix can be determined using the weak forms in equation (5.41), t. The nodal degrees of freedom $\hat{\underline{d}}_I$, and their rates $\dot{\hat{\underline{d}}}_I$ at each node I are the displacements and the scalar valued order parameter,

$$\hat{\underline{d}}_I = \begin{bmatrix} \hat{\underline{u}}_I \\ \hat{\phi}_I \end{bmatrix}, \quad \text{and} \quad \dot{\hat{\underline{d}}}_I = \begin{bmatrix} 0 \\ \dot{\hat{\phi}}_I \end{bmatrix}. \quad (5.44)$$

The nodal residual vector is a function of the nodal degrees of freedom and their rate, consisting of a residual vector for the mechanical problem and a scalar residual for the chemical part

$$\underline{R}_I = \begin{bmatrix} \underline{R}_I^u \\ R_I^\phi \end{bmatrix}. \quad (5.45)$$

The residual for the mechanical problem is

$$\underline{R}_I^u = \int_V \left(\underline{\mathbf{B}}_I^{u\top} \underline{\sigma} \right) dV, \quad (5.46)$$

where the stress $\underline{\sigma}$ is in Voigt notation. The residual for the evolution of the order parameter is

$$R_I^\phi = \int_V \frac{\dot{\phi}}{M} N_I + \frac{\partial f^u}{\partial \phi} N_I + \frac{\partial f^{\text{ch}}}{\partial \phi} N_I + GL(\nabla \phi) \underline{B}_I^\phi dV. \quad (5.47)$$

The tangent matrices can be obtained by deriving the residual vector with respect to \underline{d} . Here, a symmetric tangent matrix is obtained

$$\underline{\mathbf{K}}_{IJ} = \frac{\partial R_I}{\partial \hat{d}_J} = \begin{bmatrix} \underline{\mathbf{K}}_{IJ}^{uu} & \underline{\mathbf{K}}_{IJ}^{u\phi} \\ \underline{\mathbf{K}}_{IJ}^{\phi u} & \underline{\mathbf{K}}_{IJ}^{\phi\phi} \end{bmatrix}. \quad (5.48)$$

In order to determine the entries of the tangent matrix, several first and second order derivatives are needed. The derivatives of the chemical energy are given in (5.1), (5.4), and (5.5). The derivatives of the elastic energy read

$$\begin{aligned} \frac{\partial f^u}{\partial \phi} &= \frac{\partial f^u}{\partial \underline{\mathbf{C}}} \frac{\partial \underline{\mathbf{C}}}{\partial \phi} + \frac{\partial f^u}{\partial \underline{\boldsymbol{\varepsilon}}^e} \frac{\partial \underline{\boldsymbol{\varepsilon}}^e}{\partial \phi} \\ &= \frac{1}{2} \underline{\boldsymbol{\varepsilon}}^e : [\underline{\mathbf{C}}_1 - \underline{\mathbf{C}}_0] : \underline{\boldsymbol{\varepsilon}}^e + \underline{\boldsymbol{\varepsilon}}^e : \underline{\mathbf{C}} : [-\underline{\boldsymbol{\varepsilon}}_1^*], \end{aligned} \quad (5.49)$$

$$\frac{\partial^2 f^u}{\partial \phi^2} = -2 \underline{\boldsymbol{\varepsilon}}^e : [\underline{\mathbf{C}}_1 - \underline{\mathbf{C}}_0] : \underline{\boldsymbol{\varepsilon}}_1^* + \underline{\boldsymbol{\varepsilon}}_1^* : \underline{\mathbf{C}} : \underline{\boldsymbol{\varepsilon}}_1^*, \text{ and} \quad (5.50)$$

$$\frac{\partial^2 f^u}{\partial \underline{\boldsymbol{\varepsilon}} \partial \phi} = \frac{\partial \underline{\boldsymbol{\sigma}}}{\partial \phi} = [\underline{\mathbf{C}}_1 - \underline{\mathbf{C}}_0] : \underline{\boldsymbol{\varepsilon}} - \underline{\mathbf{C}} : \underline{\boldsymbol{\varepsilon}}_1^*. \quad (5.51)$$

The matrix entries are

$$\underline{\mathbf{K}}_{IJ}^{uu} = \frac{\partial R_I^u}{\partial \hat{u}_J} = \frac{\partial R_I^u}{\partial \underline{\boldsymbol{\varepsilon}}} \frac{\partial \underline{\boldsymbol{\varepsilon}}}{\partial \hat{u}_J} = \int_V (\underline{\mathbf{B}}_I^u)^\top \underline{\mathbf{C}} (\underline{\mathbf{B}}_J^u) dV, \quad (5.52)$$

where $\underline{\mathbf{C}}$ are the material constants in Voigt notation. The stiffness matrix entry for the phase field problem is a scalar

$$K_{IJ}^{\phi\phi} = \frac{\partial R_I^\phi}{\partial \hat{\phi}_J} = \int_V N_I \left(\frac{\partial^2 f^u}{\partial \phi^2} + \frac{\partial^2 f^{\text{ch}}}{\partial \phi^2} \right) + GL \underline{B}_I^\phi \cdot \underline{B}_J^\phi dV. \quad (5.53)$$

The mixed entries read

$$K_{IJ}^{u\phi} = \frac{\partial R_I^u}{\partial \hat{\phi}_J} = \int_V (\underline{\mathbf{B}}_I^u)^\top \frac{\partial \underline{\boldsymbol{\sigma}}}{\partial \phi} N_J dV, \quad (5.54)$$

$$K_{IJ}^{\phi u} = \frac{\partial R_I^\phi}{\partial \hat{u}_J} = (K_{IJ}^{u\phi})^\top. \quad (5.55)$$

Hence the field equations can be solved using a finite element scheme.

5.4 Interface Propagation

In order to test the temperature dependent separation potential, the interface propagation on a two dimensional beam is determined. The material parameters for pure iron are used in order to compare it to molecular dynamics simulation. Recalling chapter 3, the martensitic transformation is temperature dependent. This leads to a temperature dependent chemical energy as outlined in section 5.1.

Two examples are presented here. First, no load is applied to the beam, such that the interface between the austenitic and the martensitic phase can progress unobstructedly. Furthermore, the influence of the mobility is discussed. In the second example, a load is applied to the far ends of the beam, which influences the propagation speed of the martensitic phase.

Consider a beam of 176 nm length and 35.2 nm height. The parameters for the temperature dependent chemical potential are chosen according to Table 5.2. They read

$$\gamma = 0.8799, \quad \hat{\theta} = 1.0321 \cdot 10^2, \quad T = 823.748 \text{ K}, \quad \text{and} \quad T_{\text{fix}} = 723.748 \text{ K}. \quad (5.56)$$

In order to ensure comparability, the material parameters are according to (Schmitt, Müller, Kuhn, and Urbassek, 2013a). The transformation strain is determined according to the Bain orientation relationship in (3.3), yielding

$$\boldsymbol{\varepsilon}_1^* = \begin{bmatrix} -0.2217 & 0 \\ 0 & 0.1007 \end{bmatrix} \quad (5.57)$$

The parameters for the elastic constants in the austenitic and the martensitic phase in Voigt notation are

$$\mathcal{C}_0 = \begin{bmatrix} 2.219 & 1.498 & 0 \\ 1.498 & 2.219 & 0 \\ 0 & 0 & 0.3 \end{bmatrix} \cdot 10^5 \text{ N mm}^{-2}, \quad \text{and} \quad (5.58)$$

$$\mathcal{C}_1 = \begin{bmatrix} 2.927 & 1.062 & 0 \\ 1.062 & 2.927 & 0 \\ 0 & 0 & 0.932 \end{bmatrix} \cdot 10^5 \text{ N mm}^{-2}, \quad (5.59)$$

respectively. The parameters for the phase field problem are fitted by Schmitt, Wang, and Urbassek (2013b) to the molecular dynamics simulation by Sandoval, Urbassek, and Entel (2009). They read accordingly

$$G = 0.97 \text{ J m}^{-2}, \quad L = 10 \text{ nm}, \quad \text{and} \quad M = 9.6 \text{ m N}^{-1} \text{ s}^{-1}. \quad (5.60)$$

Calculations at two hundred different temperatures have been conducted. In order to accommodate for the change in the parameter A , the temperatures have been chosen according to

$$T_k = T_0 + 8T_0 \left(\frac{k-1}{N} - \frac{1}{2} \right)^3, \quad \text{where } k = 1, 2, \dots, N. \quad (5.61)$$

This ensures that temperatures close to the equilibrium temperature, where the change in A is bigger, are spaced closer together. Consequently temperatures further from the equilibrium temperature are spaced further apart as the change in A is minor.

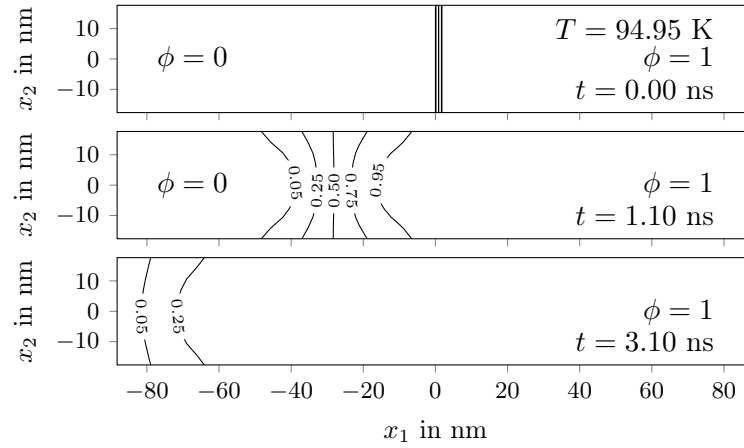
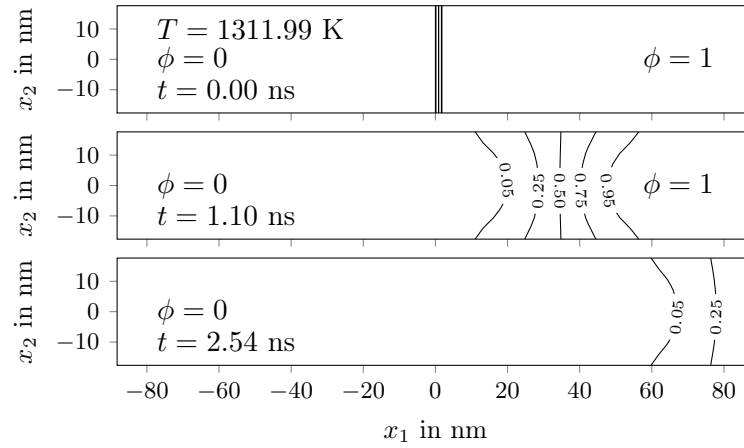
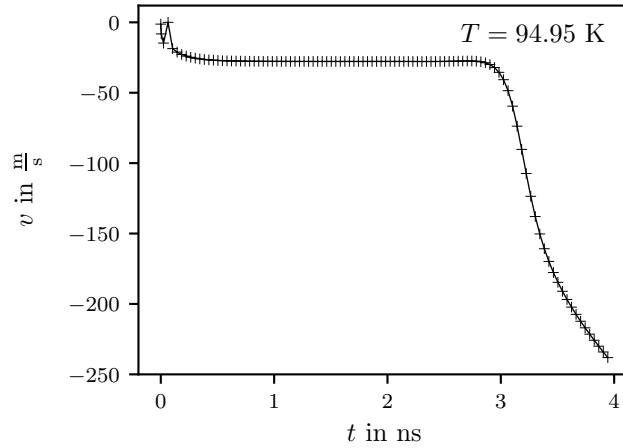
FIGURE 5.6: Interface motion for $T = 94.95$ KFIGURE 5.7: Interface motion for $T = 1311.99$ K

Figure 5.6 shows the interface motion for a temperature of $T = 94.95$ K. At this temperature, the martensitic phase is stable. That means, austenite forms into martensite. The initial configuration is shown at the time $t = 0$. The left half of the beam is initialized with austenite ($\phi = 0$), whereas the right side of the beam is initialized with martensite ($\phi = 1$). The bottom left node is pinned and the bottom right node is a simple support allowing movement in x_1 -direction only. There is no load applied on the far end of the beam.

As austenite transforms into martensite, the interface moves to the left. A snapshot for $t = 1.1$ ns is shown. The curvature of the interface is due to the introduction of the transformation strain $\underline{\epsilon}_1^*$ and the phase dependent material constants \underline{C} . The interface position is identified where $\phi = 0.5$, or in other terms where austenite and martensite have a 50% share of the chemical composition. At $t = 3.1$ ns, the interface is at the left end of the beam. This allows to manually calculate the interface velocity to $v_{\text{man}}(T = 94.95 \text{ K}) = -28.46 \text{ m s}^{-1}$. The minus sign is equivalent to a motion to the left against the x_1 -direction. Given this specific initial configuration, it is also tantamount to a transformation from the austenitic to the martensitic phase.

In Figure 5.7 the same initial configuration and boundary conditions as in example prior are used, where only the temperature has been changed to $T = 1311.99$ K. The

FIGURE 5.8: Interface velocity over time for $T = 94.95$ K

temperature above the equilibrium temperature causes the austenitic phase to be stable. Therefore the interface motion is to the right. At the time $t = 2.54$ ns, the interface reaches the far right end of the beam. The interface velocity was manually determined to be $v_{\text{man}}(T = 1311.99 \text{ K}) = 34.74 \text{ m s}^{-1}$. The positive sign indicates a motion to the right. Consequently, in view of the initial setup, this is synonymous to a transformation from the martensitic to the austenitic phase. Manually calculating the interface velocity is tedious, and with an increasing number of simulations not feasible. Typically, post-processing is automated in order to determine quantities unrelated to the solution of the problem. Here, the use of configurational forces is employed, allowing for an ad-hoc evaluation of the velocity (and also further quantities) during the solution process without potentially computationally expensive post-processing. Kuhn (2013) uses configurational forces in her work to get a better insight into the energetic driving mechanisms in a phase field model for fracture. The works of Gurtin (1999), and Kuhn and Müller (2010) give a good introduction into the realm of configuration forces. Following Kuhn (2013), the dissipative part of the configurational forces balance reads

$$\underline{G}_{\text{dis}} = \int_V -g_{\text{dis}} dV = \int_V -\frac{\dot{\phi}}{M} \underline{\nabla} \phi dV. \quad (5.62)$$

The phase field $\phi(\underline{x}, t)$ is thought to be translated. This is for example true in the examples above, as the interface progresses either to the right, or left, however there is no change in topology, size, or shape. With that assumption, the configuration at a time t can be expressed in terms of its initial state $\phi(\underline{x}, 0)$, therefore

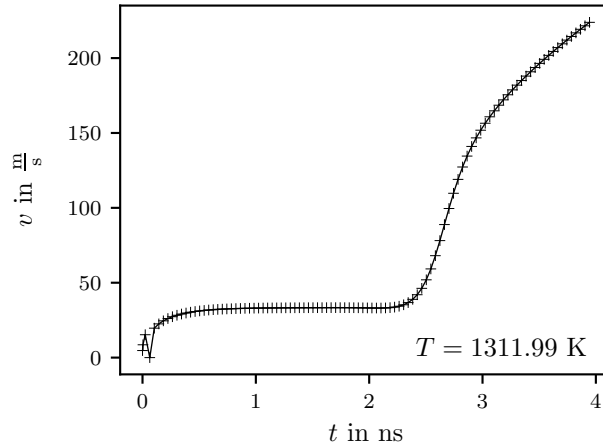
$$\phi(\underline{x}, t) = \phi(\underline{x} - x_1^{\text{pos}}(t)\underline{e}_1, 0), \quad (5.63)$$

where $x_1^{\text{pos}}(t)$ denotes the x_1 -position of the interface at time t . Differentiation of ϕ yields

$$\underline{\nabla} \phi = \frac{\partial \phi}{\partial x_1} \underline{e}_1 \quad (5.64)$$

Furthermore, the time derivative of the phase field can be determined.

$$\dot{\phi} = \frac{\partial \phi}{\partial t} = \frac{\partial \phi}{\partial \underline{x}} \frac{\partial \underline{x}}{\partial t} = \underline{\nabla} \phi \cdot \frac{\partial \underline{x}}{\partial t} = -\underline{\nabla} \phi \frac{\partial x_1^{\text{pos}}(t)}{\partial t} \underline{e}_1 = \frac{\partial \phi}{\partial x_1} \dot{x}_1^{\text{pos}}, \quad (5.65)$$

FIGURE 5.9: Interface velocity over time for $T = 1311.99$ K

where $\dot{x}_1^{\text{pos}} = v$ is the velocity of the interface. Substituting (5.65) and (5.64) back into (5.62), the interface velocity reads

$$\underline{v}(t) = \frac{M\underline{G}_{\text{dis}}}{\int_V \left(\frac{\partial\phi}{\partial x_1}\right)^2 dV}, \quad \text{where} \quad v(t) = \underline{v}(t) \cdot \underline{e}_1 \quad (5.66)$$

is the velocity in x_1 -direction. Using the above relation a time dependent velocity can be determined as for example shown in Figure 5.8 for a temperature of $T = 94.95$ K, or as shown in Figure 5.9 for a temperature of $T = 1311.99$ K. As previously discussed, the negative sign means a transformation from the austenitic to the martensitic phase takes place. Conversely, in this example, the positive sign indicates a transformation from the martensitic to the austenitic phase. Initially, until about $t = 0.7$ ns for $T = 94.95$ K, and $t = 1$ ns for $T = 1311.99$ K, the interface velocity speeds up. That is because in this stage the interface forms.

After that, the interface velocity is constant. Here, the interface translates, such that the assumption in (5.63) still holds. The interface motion is in a steady state. This phase is until $t = 2.8$ ns and 2.2 ns for the temperatures $T = 94.95$ K and 1311.99 K, respectively. In this steady state the mean interface velocity can be calculated. The interface during the transformation from austenite to martensite progresses at -27.87 m s^{-1} ($T = 94.95$ K), and the interface for the reverse transformation progresses at 33.26 m s^{-1} .

After the steady state, the absolute value of the velocity rapidly increases. However, here there should be no speed at all. The term in the denominator of (5.66) is a measure for the gradient term. The term decreases faster than the dissipative configurational force $\underline{G}_{\text{dis}}$, eventually reaching 0, which causes a virtual increase in the velocity. Therefore the value for the interface velocity in the final stage cannot be used for evaluation.

Table 5.3 compares interface velocities, which have been obtained manually, by using configurational forces, and from literature. The manually obtained velocity validates the velocity obtained from the dissipative part of the configurational forces balance. Furthermore, they are in the same order of magnitude as the velocities calculated in Schmitt, Wang, and Urbassek (2013b). The appendix provides further plots for

TABLE 5.3: Comparison of the interface velocities obtained manually (v_{man}), using configuration forces (\bar{v}_{cf}), and from literature (Schmitt, Wang, and Urbassek, 2013b)

T	v_{man}	\bar{v}_{cf}	Schmitt, Wang, and Urbassek, 2013b
94.95 K	-28.46 m s^{-1}	-27.78 m s^{-1}	-25.11 m s^{-1} (at 100 K)
1311.99 K	34.74 m s^{-1}	33.26 m s^{-1}	28.52 m s^{-1} (at 100 K)

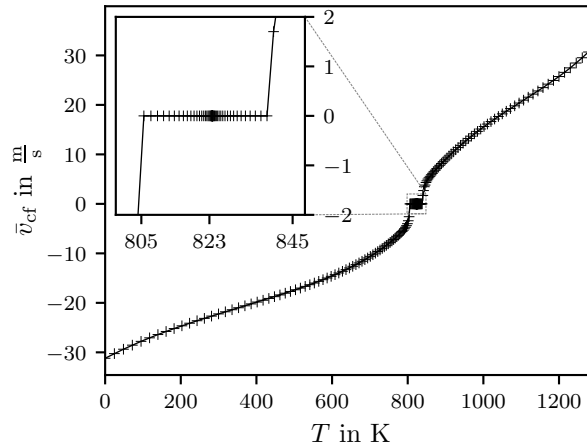


FIGURE 5.10: Mean interface velocity \bar{v}_{cf} obtained using configurational forces over the temperature. The inset on the top left shows the region around the equilibrium temperature in detail. The pluses (+) mark the data points.

the interface velocity for temperatures close to the equilibrium temperature, see Figures 8.1 and 8.2. The absolute velocities for the temperatures $T = 654.57 \text{ K}$ and 992.93 K is considerably higher. This is expected, as the energy barrier Δf increases while approaching the equilibrium, therefore slowing down the transformation.

5.4.1 Temperature Dependency of the Interface Propagation

As a consequence of using the dissipative part of the configurational force balance, the post-processing is redundant, and the calculation of the interface velocity is ad-hoc with measures already calculated during the simulation. This allows to represent the interface velocity in dependence of the temperature as in Figure 5.10. Again, velocities with a negative sign correspond to a transformation from the austenitic to the martensitic phase. The same applies in reverse for velocities with a positive sign. The inset shows a zoomed in view of the region around the equilibrium temperature $T_0 = 823.75 \text{ K}$. In its vicinity, between 805.66 K and 838.24 K , there is no motion of the interface at all, e.g., the interface velocity vanishes. The interface velocity goes to zero, as for one the parameter A goes toward infinity (5.24), and as a consequence the energy barrier Δf_L , grows indefinitely. While there is still an energy difference between the stable and the metastable phases, it is marginal small compared to the barrier Δf_L in proximity of the equilibrium temperature, such that numerical errors smooth the difference away. For temperatures far from the equilibrium temperature, the interface velocity is almost linear. While A is symmetric to T_0 , the energy barrier Δf_L is not, as illustrated in Figure 5.3. This leads to another representation of the interface velocity. In view of (5.11), the energy barrier is a function of A . Here, A is a function of the temperature, described in (5.24). Substituting the aforementioned

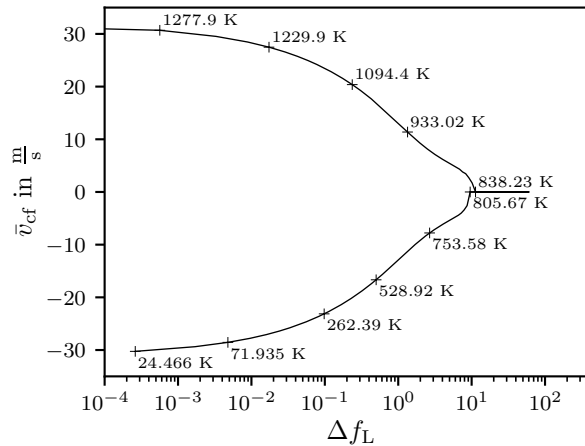


FIGURE 5.11: Mean interface velocity \bar{v}_{cf} obtained using configurational forces over the energy barrier Δf_L with temperatures corresponding to the respective velocities (+)

equations, each temperature can be mapped to the energy barrier Δf_L through the relation

$$\Delta f_L = \Delta f_L(A(T)). \quad (5.67)$$

With the results in Figure 5.10, a map from the temperature T to the velocity is given. Using the relation in (5.67), the temperature scale can be remapped to the energy barrier Δf_L . The corresponding plot is shown in Figure 5.11. This representation $v(\Delta f_L)$ has several advantages compared to the representation $v(T)$. It is symmetric for small $\Delta f_L < 0.5$, such that

$$\Delta f_L(\bar{v}_{cf}) = \Delta f_L(-\bar{v}_{cf}). \quad (5.68)$$

Furthermore, it is independent of T . However, if a function $A(T)$ is provided, the corresponding temperatures can be calculated. Here they are indicated with a plus (+). In addition, this allows to design a function $\Delta f_L(T)$ or $A(T)$, if the interface velocity v is known at specific temperatures T .

Secondly, the model parameters can be verified on the fly without re-running the simulation. For example Schmitt, Wang, and Urbassek (2013b) use $A = 6$ and $D = 1$ for a temperature of $T = 100$ K. At this temperature the martensitic phase is stable. In view of equation (5.11) the energy barrier Δf_L can be determined to be 0.0547. Using the graph in Figure 5.11, and with the knowledge that a transformation from the martensitic to the austenitic phase leads to a negative interface velocity, the determined interface velocity is $v_{\Delta f_L} = -24.64 \text{ m s}^{-1}$. This value corresponds well to the value of $v_{\Delta f_L} = -24.11 \text{ m s}^{-1}$ determined in the work of Schmitt, Wang, and Urbassek (2013b).

The same applies for a temperature of 1300 K. The parameters $A = 15$ and $D = 0$ have been used. The austenitic phase is stable. The value can be determined to be $\Delta f_L = 0.0127$, leading to an interface velocity of $v_{\Delta f_L} = -28.01 \text{ m s}^{-1}$, which is well in agreement with the literature value in Table 5.3.

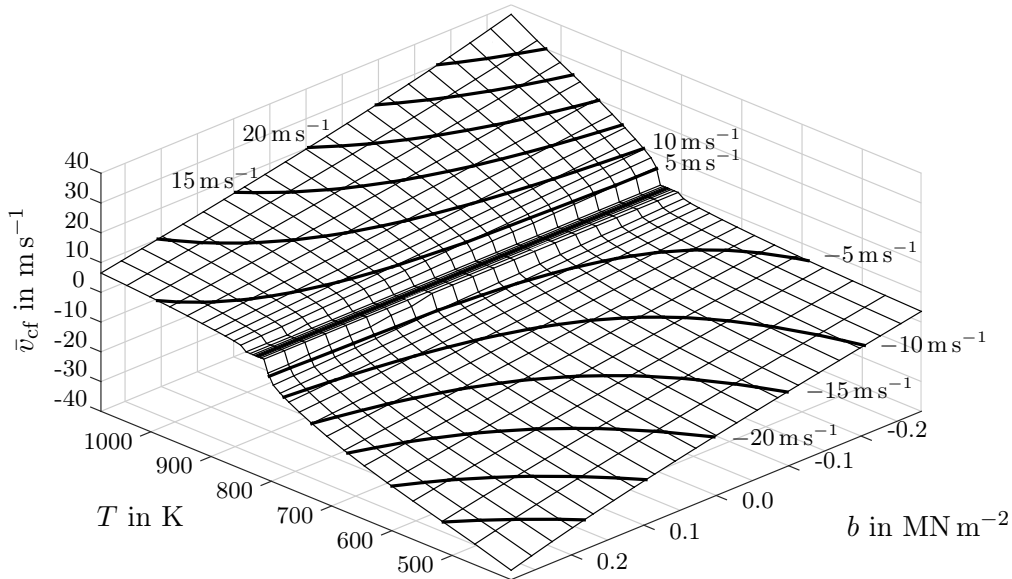


FIGURE 5.12: Mean interface velocity \bar{v}_{cf} over temperature T and load b . The thick solid lines are contour lines. Each grid point represents one simulation

5.4.2 Influence of Load on the Interface Propagation

The influence of load and temperature on the kinetics of the martensitic transformation has been discussed in e.g. Schmidt et al. (2016). Here, the same parameters as above have been used. However, a load b in x_1 -direction is applied to the far ends of the beam. In total, velocities from 777 simulations are represented in Figure 5.11 at 21 distinct loads and 37 distinct temperatures. The mean interface velocity is obtained through the use of configurational forces. The load influences the interface propagation. Here, a compression favors a transformation towards the austenitic phase, whereas a tensile load favors a transformation towards the martensitic phase. Hence, depending on the temperature, it is possible to increase or to decrease the interface velocity. That is with the exception of temperatures in the vicinity of the equilibrium as shown for example in Figure 5.10. Between $T = 805.66 \text{ K}$ and 838.24 K , there is no motion of the interface at all. Applying a load does not change this circumstance. That is due to the pole in the function $A(T)$ at the equilibrium temperature, causing the energy barrier Δf_L to increase indefinitely. Therefore the elastic energy in that temperature range is unimportant and does not influence the kinetics.

The thick contour lines show lines of constant velocity, spaced apart by 5 m s^{-1} . With temperatures further from the equilibrium temperature, the contour lines curve away from the load axis. Therefore the influence of the load on the velocity increases. Consider for example the contour line of $\bar{v}_{cf} = 10 \text{ m s}^{-1}$. This contour is exclusively below the equilibrium temperature. With no load applied, the temperature is about 700 K . In order to achieve the same velocity of 10 m s^{-1} at 400 K , a load of $b = -0.2 \text{ MN m}^{-2}$ has to be applied. However, in order to achieve the same velocity at 550 K , the load is about -0.16 MN m^{-2} . That means as the energy barrier Δf_L decreases, the influence of the load is higher. An explanation is the relation between the mechanical and the chemical energy.

5.5 Locally Varying Temperature Field

The process of cryogenic turning makes use of temperature effects. The cooling agent, for instance liquid nitrogen or carbon dioxide snow, cools down the workpiece and the tool near the surface. The observed effects are a reduction of the cutting temperature leading to higher machining accuracy, less tool wear, and lower cutting forces (Dhananchezian, Kumar, and Sornakumar, 2011). In the case of metastable austenitic steels, such as AISI 437, a phase transformation is possible, inducing an increase in martensite content in the near surface region (Mayer, Kirsch, and Aurich, 2014). The temperature for this process has been quantified locally and in time using a set of thermocouples. The work of Becker et al. (2018) supplements the measurements with a finite element model, yielding a transient temperature field.

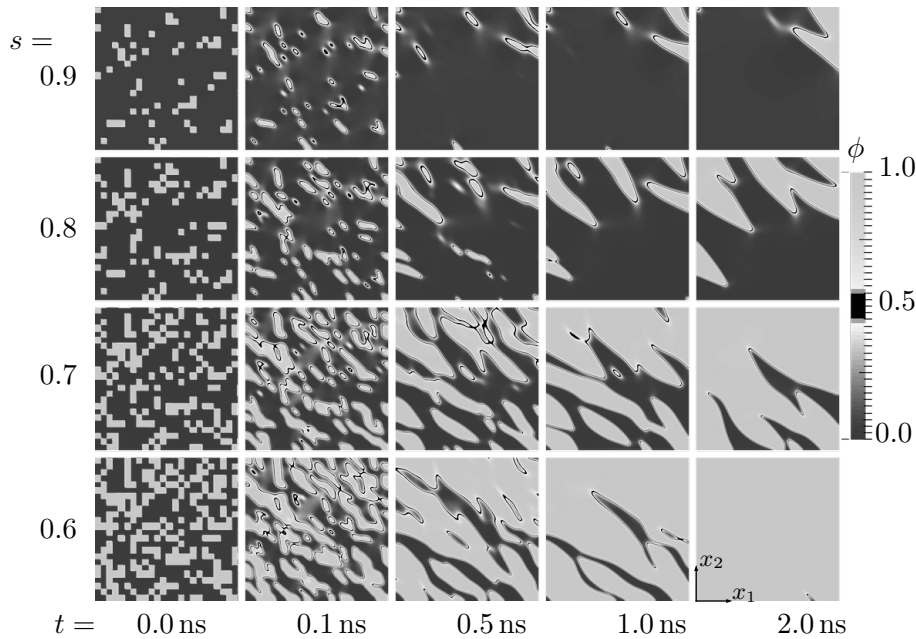


FIGURE 5.13: Martensitic transformation at different times t with different initializations s .

Using the temperature dependent chemical energy developed in the previous chapter, it is possible to vary the temperature field spatially. Hence the chemical energy changes depending on the spatial position. Consider a plate of 345 nm width and height, where the bottom left node is pinned and the bottom right node is a simple support allowing for displacement in x_1 -direction. This plate is divided up into a grid of $24 \cdot 24 = 576$ equally spaced quadratic subregions. Initially, each of these regions may either be austenite or martensite. A pseudo random number generator is used to determine value on the interval $[0, 1)$. A threshold s is chosen for the whole plate. Subregions endowed with a value above this threshold s are initialized as purely martensitic, otherwise they are austenite. Therefore this threshold s is a measure for the initial austenite content.

The temperature is considered to be constant in time, but varying locally in x_2 -direction. The temperature is scaled using a third degree polynomial with continuity

in the first order derivative

$$T(\zeta) = \begin{cases} T_{\text{bot}} & \text{if } \xi < 0 \\ T_{\text{top}} & \text{if } \xi > 1 \\ T_{\text{bot}} + (T_{\text{top}} - T_{\text{bot}})h_{\text{cubic}}(\xi) & \text{otherwise,} \end{cases} \quad (5.69)$$

where h_{cubic} is the cubic interpolation function defined in (4.24). The x_2 -coordinate is remapped to ξ

$$\xi = \frac{x_2 - 0.25 \cdot 345 \text{ nm}}{0.5 \cdot 345 \text{ nm}}. \quad (5.70)$$

Therefore in the bottom quarter the temperature is constant at T_{bot} , it is interpolated until reaching the top quarter where it is at T_{top} . The temperatures are $T_{\text{bot}} = 600 \text{ K}$, and $T_{\text{top}} = 300 \text{ K}$. The transformation strain ξ_1^* , as well as all further parameters such as the elastic constants for the austenitic and the martensitic phase, $\mathbf{C}_{\approx 0}$ and $\mathbf{C}_{\approx 1}$, the mobility M , the interface width L , and the interface energy G are chosen according to chapter 5.4.

Snapshots in Figure 5.13 at the distinct simulation times $t = 0 \text{ ns}$, 0.1 ns , 0.5 ns , 1 ns , and 2 ns for the initialization thresholds $s = 0.6$, 0.7 , 0.8 , and 0.9 are shown in Figure 5.13. The martensitic phase ($\phi = 1$) is displayed in light gray, and the austenitic phase ($\phi = 0$) is displayed in dark gray. The martensitic content almost exclusively increases with progressing time and decreasing s . This behavior is due to the chemical potential, as here the temperature is always below the equilibrium temperature T_0 . Another temperature dependent effect is the width of the transition zone. In the upper region where the temperature is at 600 K , the interface region in black is narrower than in the bottom region where the temperature is at 300 K . The energy barrier Δf_{L} is the cause of this issue, as it increases when the temperature reaches the equilibrium T_0 .

The martensite content is dependent on the temperature. In the top region, the martensite content is considerably higher than in the bottom region. As the time progresses, the martensite in the top region forms faster than in the bottom region, with the exception of $s = 0.9$. Here, martensite transform into austenite due to the small initial martensite content. As a conclusion, the martensitic transformation is temperature dependent. It can vary locally due to a changing temperature field.

6 A Homogenization Phase Field Approach

6.1 Motivation

A Voigt/Taylor homogenization phase field approach is presented in this chapter. The Voigt/Taylor approach shares many properties with the related Reuss/Sachs approach. In contrast with the Khachaturyan approach presented in the previous chapter, this model does not rely on a unified material law by assuming the behavior of the effective material parameters such as amongst others the material tangent and the transformation strain, see chapter 5 and the works of Schmitt, Kuhn, Müller, and Bhattacharya (2014), Ammar, Appolaire, Cailletaud, and Forest (2009), and Rancourt, Appolaire, Forest, and Ammar (2016). As an advantage, a different material law can be chosen for the individual phases. The flexibility of choosing material laws independently comes at a cost: the material laws in the individual phases need to be solved individually. However, as they are independent, e.g., there is no input from one phase to another, they can be solved separately. This makes parallelization straightforward, mitigating this issue partially.

Another important factor is the presence of history variables. Typically, structure and therefore plasticity and transformation history is retained. This phenomenon is referred to as inheritance and was discussed in section 3.2 above. It makes sense theoretically (Schmitt, Kuhn, Müller, and Bhattacharya, 2014) and is observed experimentally as well (Li et al., 2016). Implementation wise, in the purely elastic case, no history variables are needed at all. However when an individual material law for each individual phase is present, it is important to unify the history fields. When regarding similar plasticity theories for the individual phases, for example crystal plasticity, but with phase dependent yield strengths and slip directions, the same set of history variables is used to record the plastic deformation. Inheritance is implemented by accessing the same history variable field with no dependence of the phases. This is not the case if plasticity theories for the individual phases are assumed, like kinematic hardening in one and isotropic hardening in another phase. In order to inherit the plasticity, the kinematic hardening history variables need to be considered in the isotropic hardening material law and vice versa.

The effective material parameters follow from the state of the mixture indicated by the phase field parameter. Consequently, already existing and implemented materials laws can be used with no additional need for implementation, as long as they share a common interface with the homogenization phase field method presented here. Typical inputs for material routines are the total strain, and the history variables. Outputs include the stress, the material tangent, and the updated history variables. In the case of this phase field homogenization scheme, the elastic energy is a required output. Finite Element frameworks, such as ANSYS, FEAP and Comsol have material subroutines, where typically well-known material laws are provided out of the box

(Taylor, 2014; Pepper and Heinrich, 2017). Furthermore, users have the possibility to implement their custom material laws. This makes this homogenization phase field approach viable even for user defined material subroutines.

To sum up, the Voigt/Taylor and the Reuss/Sachs approach have the following features:

1. It is possible to chose individual material laws for the individual phases. This makes cases where plasticity occurs in the austenitic phase only, or transformed anisotropic material with different anisotropic directions easy to implement.
2. As a downside, it is necessary to solve the material laws of the phases individually. However, parallelization mitigates this issue. The implementation is straightforward.
3. The effective material parameters follow by assuming uniform strain (Voigt/-Taylor) or uniform stress (Reuss/Sachs). As a consequence already implemented material laws can be re-used as long as they interface with the homogenization scheme.
4. The implementation of individual and separate history variable fields for the individual phases is straightforward. However, when mixing, e.g., kinematic hardening and isotropic hardening plasticity, there is a need to translate the history variables.

Phase field models with homogenization schemes have first been proposed in Ammar, Appolaire, Cailletaud, and Forest (2009). They have been applied in, e.g., Rancourt, Appolaire, Forest, and Ammar (2016). For an extended introduction to phase field homogenization methods the interested reader is referred to the works of Mosler, Shchyglo, and Hojjat (2014).

6.2 Assumptions

In the Voigt/Taylor approach the strain is assumed to be uniform in each phase and in the diffuse interface, see e.g. (Hori and Nemat-Nasser, 1999; Ammar, Appolaire, Cailletaud, and Forest, 2009; Mosler, Shchyglo, and Hojjat, 2014; Rancourt, Appolaire, Forest, and Ammar, 2016)

$$\boldsymbol{\varepsilon} = \boldsymbol{\varepsilon}_1 = \dots = \boldsymbol{\varepsilon}_\alpha = \dots = \boldsymbol{\varepsilon}_n. \quad (6.1)$$

In contrast to the Reuss/Sachs model, this allows to formulate the material law within the phases with the elasticity tensor rather than the compliance tensor. The stress in a phase α is defined as the derivative of the energy with respect to the elastic strain

$$\boldsymbol{\sigma}_\alpha = \frac{\partial f_\alpha}{\partial \boldsymbol{\varepsilon}_\alpha^e} = \boldsymbol{C}_\alpha : \boldsymbol{\varepsilon}_\alpha^e. \quad (6.2)$$

In the interface region, the stress is interpolated. In view of (4.22), a scalar function h which can be used to interpolate within a vector valued phase field

$$\boldsymbol{\sigma} = \boldsymbol{\sigma}_0 h^0(\phi_1, \dots, \phi_n) + \sum_{\alpha=1}^n \boldsymbol{\sigma}_\alpha h(\phi_\alpha). \quad (6.3)$$

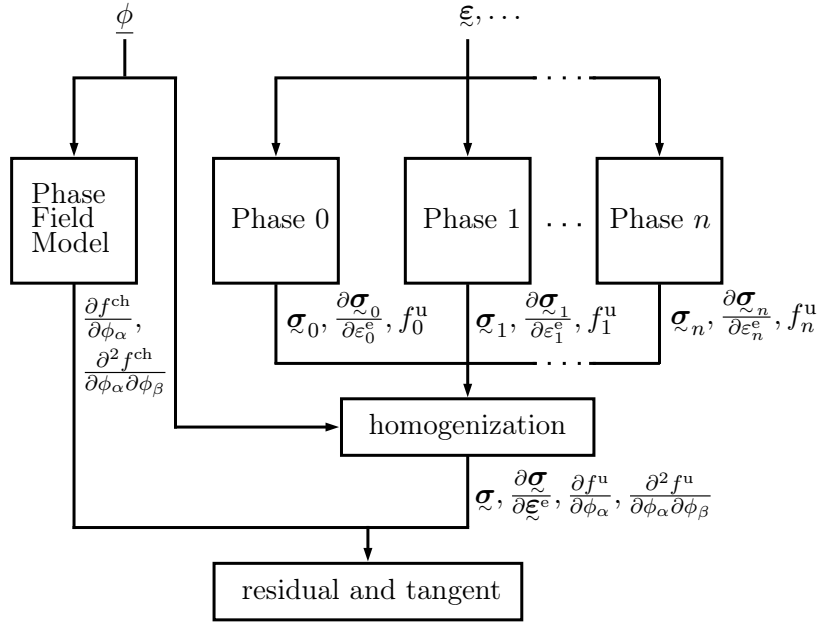


FIGURE 6.1: Flow chart of the Voigt/Taylor homogenization approach for a phase field for the martensitic transformation.

The local elastic energy is therefore

$$f_u = f_{u_0} h^0(\phi_1, \dots, \phi_n) + \sum_{\alpha=1}^n f_{u_\alpha} h(\phi_\alpha). \quad (6.4)$$

There are several advantages of interpolating the elastic energy directly. Choosing the proper interpolation functions as in (4.29) in view of (4.38), the elastic energy does not exceed the bulk values if $\phi \in [0, 1]$. This stands in contrast to the Khachatryan approach (see Figure 6.3 and Chapter 6.2.2). However, the elastic energy for $\phi < 0$ and $\phi > 1$ is not bounded in general.

A closer look at (6.4) and (6.3) reveals that the mechanical behavior within the phases can be chosen independently of how the phase field parameter evolves. Therefore the derivative of the elastic energy with respect to the elastic strain remains the sum of all the derivatives within the phases. The same applies for the derivatives of the stress with respect to the strain. Figure 6.1 shows the flow chart for the Voigt/Taylor approach. The inputs are the state of the phase field noted by the phase field parameter ϕ and the strain ξ , which is for example obtained from the displacement in a FEM calculation. Additional input parameters, such as the temperature or history variables are possible. Here they are neglected, without the loss of generalization. Furthermore, material parameters are not shown in this flow chart. Typically, they are constant for each phase and are therefore regarded as intrinsic. From an implementation standpoint however, they still need to be provided in the material routines. An individual material law is implemented for each individual phase from 0 (parent phase), 1, through n (child phases). Here, any material law that provides stress, the derivative of stress w.r.t elastic strain, and the elastic energy can be implemented. The phase field independence of the material laws makes it also versatile. Not only custom material laws can be used, the Voigt/Taylor scheme also provides an interface for already implemented material routines. The versatility comes at a cost: each individual material law needs to be solved individually. However, as the flow chart

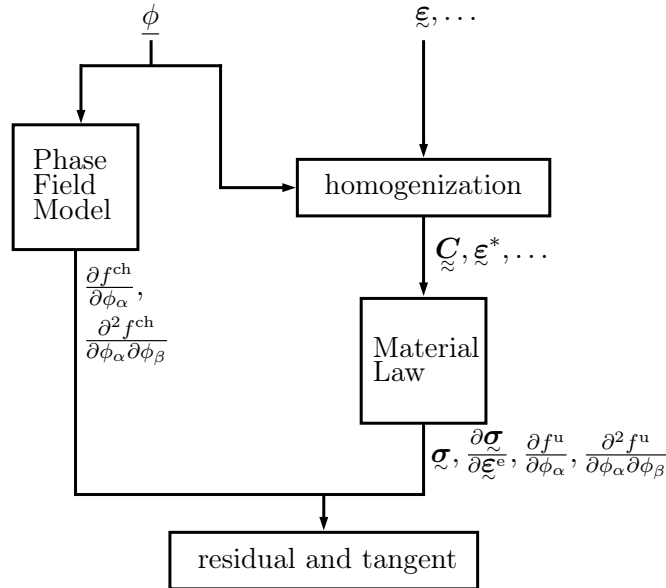


FIGURE 6.2: Flow chart of the Khachaturyan approach for a phase field for the martensitic transformation.

shows, they can be run in parallel. The output parameters of the individual phases are needed as input in the subsequent homogenization step. The phase field determines the homogenized quantities, such as stress, the derivative of stress w.r.t. elastic strain, and first and second order derivatives of the elastic energy w.r.t the phase field parameter. Only non-zero components contribute to the homogenized quantities. This offers a potential optimization of the flow chart by adding a preemptive homogenization step, where the material law is only solved in phases where the corresponding order parameter component is non-zero. This step would not change the dependency of the material law; it would just assign the program to skip phases which are not needed in the homogenization subsequent to solving the material law in the individual phases. It can't be compared to the homogenization in the Khachaturyan approach which happens prior to solving the material law. The phase field model provides the chemical free energy and its first and second order derivatives with respect to the order parameter components ϕ_α , where α assumes values from 1 through n . Given the quantities from the homogenization and the phase field model, the residual and the tangent can be formed.

Figure 6.2 shows a flow chart of the Khachaturyan approach. Here, the input parameters are the phase field parameter ϕ and the strain $\underline{\epsilon}$. Additional parameters for the homogenization step are possible. They are neglected, without losing generality. In the homogenization step, the effective material parameters are calculated driven by the phase field model. In contrast to the homogenization of the Voigt/Taylor approach, where the homogenization depends on the number of phases only, the homogenization in the Khachaturyan approach depends on the type of input parameters needed for the material law in addition to the number of phases, see for example Schmitt, Kuhn, Müller, and Bhattacharya (2014). That leads to a homogenization depending on the material law. However, only one material routine needs to be solved. This is an advantage to the Voigt/Taylor approach. In terms of implementation, there is no need to generalize for n number of phases. In fact, a generalization would require to account for different types of input parameters and numbers of phases and it is therefore not practicable. The homogenization is adapted depending on the material law and

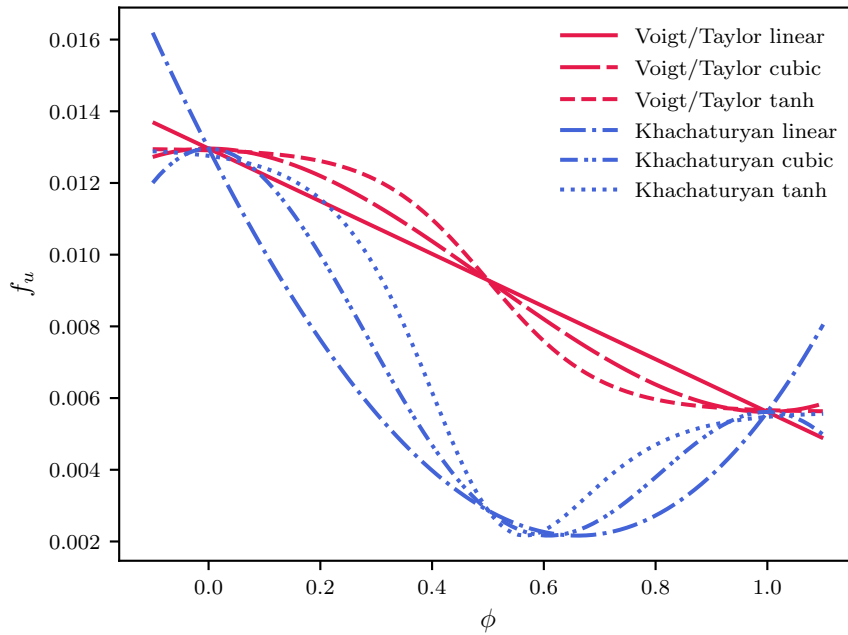


FIGURE 6.3: Elastic energy in a uniform strain setting for the Khachaturyan (blue) and the Voigt/Taylor approach (red), for a linear (small, dash-dot), a cubic (dashes, dash-dot-dot) and a scaled tangens hyperbolicus (small dashes, dots) interpolation function h

the number of phases. That makes the Khachaturyan approach more flexible because the interface between the homogenization step and the material law is not rigid as for example in the Voigt/Taylor approach. The material law provides the quantities stress, stress w.r.t. strain, and the first and second order derivatives of the elastic energy w.r.t. to the phase field parameter. The phase field model yields the first and second order derivatives of the chemical free energy w.r.t to the order parameter. Hence, the residual and the tangent can be formed. In the finite element code, the assembly of the residual and tangent matrices is the same for both the Khachaturyan and the Voigt/Taylor approach.

6.2.1 Constitutive Law and Field Equations

Until here, no assumptions about the material behavior within the phase has been made. The only requirement in (6.3) is the derivative of the stress w.r.t. strain. Following (2.18) in linear theory, the constitutive law in (6.2) with the individual phase α is formulated with

$$\underline{\varepsilon}_\alpha = \underline{\varepsilon}_\alpha^e + \underline{\varepsilon}_\alpha^*. \quad (6.5)$$

6.2.2 Elastic Energy

Figure 6.3 shows the elastic energy in a uniform strain setting of two phases ($\alpha = 0, 1$) with using different interpolation methods for the Voigt/Taylor (red) and the Khachaturyan (blue) approach as a function of the order parameter. In the following, the parameters and quantities are nondimensionalized and are chosen in order to point out the difference between the two approaches presented here. The Young's modulus is $E_0 = 1$ for the parent phase. The material reacts stiffer in the child phase, where $E_1 = 1.1$. As does martensite when compared to the austenitic parent phase (Persson,

2015). The Poisson's ratio is held constant at $\nu = 0.25$. The strain is uniform

$$\boldsymbol{\varepsilon} = \boldsymbol{\varepsilon}_{\text{uni}} = \boldsymbol{\varepsilon}_0 = \boldsymbol{\varepsilon}_1 = \begin{bmatrix} 0.09 & 0 \\ 0 & 0 \end{bmatrix}. \quad (6.6)$$

That is synonymous to a strain uniform across the phases for the Voigt/Taylor approach as in (6.1). The strain across the phases of the Khachaturyan approach, however, is not uniform in the general case. Furthermore, a transformation strain is present in the child phase only

$$\boldsymbol{\varepsilon}_0^* = \mathbf{0} \quad \text{and} \quad \boldsymbol{\varepsilon}_1^* = \begin{bmatrix} 0.02 & 0 \\ 0 & 0.05 \end{bmatrix}. \quad (6.7)$$

The elastic energy behaves as described in (6.4), where the elastic energy of the individual phases $\alpha = 1, 0$ is

$$f_\alpha^u = \frac{1}{2} [\boldsymbol{\varepsilon}_{\text{uni}} - \boldsymbol{\varepsilon}_\alpha^*] : \mathbb{C}_\alpha : [\boldsymbol{\varepsilon}_{\text{uni}} - \boldsymbol{\varepsilon}_\alpha^*]. \quad (6.8)$$

For the Voigt/Taylor case, using the linear interpolation function however, the first order derivative for $\phi = 0$ and $\phi = 1$ does not vanish as shown in Figure 6.3. This can lead to a driving force and does not ensure that an extremal point is reached in the bulk phases, neither at $\phi = 0$ nor at $\phi = 1$. That means solutions that exceed the valid range of $\phi \in [0, 1]$ can exist. However, with the coupling of the chemical free energy, providing metastable minima in the bulk phases, this can be partially mitigated. A better solution would be to choose an interpolation function with a vanishing first order derivative at $\phi = 0$ and $\phi = 1$, such as the cubic interpolation function proposed in (4.24). Another possibility is limiting the codomain of the interpolation function to $[0, 1]$, as for example with the scaled tangens hyperbolicus scaling function in (4.25). Numerical implementations can require second order derivatives, for example FEM. Using a linear interpolation function the second order derivative vanishes in the Voigt/Taylor case. For the reasons mentioned above, a non-linear interpolation function is more suitable. Here, however, one should take the partition of unity in (4.38) into consideration. A viable interpolation scheme is for example given in (4.29). The non-linear interpolation functions used here, the cubic and the scaled tangens hyperbolicus interpolation function, provide the model with a non-vanishing second order derivative of the elastic energy on the interface region. Additionally, for the bulk phases at $\phi = 0$ and $\phi = 1$, the first order derivative vanishes. Therefore, in the Voigt/Taylor homogenization approach, a non-linear interpolation function, such as the ones presented here, is the right choice.

In the Khachaturyan case, the energy is determined by the elastic strain and the elastic material moduli. In a uniform strain setting, the elastic strain $\boldsymbol{\varepsilon}^e$ is a function of the order parameter only, as are the elastic material moduli \mathbb{C} . The elastic energy is therefore given by

$$f^u = \frac{1}{2} \boldsymbol{\varepsilon}^e(\phi) : \mathbb{C}(\phi) : \boldsymbol{\varepsilon}^e(\phi) = [\boldsymbol{\varepsilon}_{\text{uni}} - \boldsymbol{\varepsilon}^*(\phi)] : \mathbb{C}(\phi) : [\boldsymbol{\varepsilon}_{\text{uni}} - \boldsymbol{\varepsilon}^*(\phi)]. \quad (6.9)$$

The choice of the interpolation function for the transformation strain $\boldsymbol{\varepsilon}^*$ and the material moduli \mathbb{C} is arbitrary, as long as they assume the bulk values in the respective phases (4.21) and satisfy (4.38). Following the interpolation scheme in (4.29), the scalar interpolation function h employed is linear. This is for example the case in, but not limited to Zhang and Chen (2005), Wang and Khachaturyan (1997), Schmidt,

TABLE 6.1: Summary of the interpolation function used for determining or interpolating the elastic energy in the Voigt/Taylor and the Khachaturyan approach

interpolation	condition	Voigt/Taylor	Khachaturyan
linear	$h(\phi) = \phi$	vanishing second order derivative non-vanishing first order derivative	non-vanishing second order derivative non-vanishing first order derivative
vanishing first order derivative	$\frac{\partial h}{\partial \phi} = 0 _{\phi=0,1}$	mitigates the driving force in the bulk phase	
restricted codomain	$h(\phi) : \mathbb{R} \rightarrow [0, 1]$	mitigates inadmissible order parameter	

Dornisch, and Müller (2017a), and Schmitt, Kuhn, Müller, and Bhattacharya (2014). A linear interpolation function, for instance, leads to a non-linear behavior of the elastic energy, where $h(\phi) = \phi$

$$\begin{aligned}
\frac{1}{2} [\boldsymbol{\varepsilon}_{\text{uni}} - h(\phi)\boldsymbol{\varepsilon}^*] : (\mathbb{C}_{\approx 0} + h(\phi)(\mathbb{C}_{\approx 1} - \mathbb{C}_{\approx 0})) : [\boldsymbol{\varepsilon}_{\text{uni}} - h(\phi)\boldsymbol{\varepsilon}^*] &= \frac{1}{2}\boldsymbol{\varepsilon}_{\text{uni}} : \mathbb{C}_{\approx 0} : \boldsymbol{\varepsilon}_{\text{uni}} + \\
&\frac{1}{2}h(\phi) \left[\boldsymbol{\varepsilon}_{\text{uni}} : (\mathbb{C}_{\approx 1} - \mathbb{C}_{\approx 0}) : \boldsymbol{\varepsilon}_{\text{uni}} - 2\boldsymbol{\varepsilon}_{\text{uni}} : \mathbb{C}_{\approx 0} : \boldsymbol{\varepsilon}^* \right] + \\
&\frac{1}{2}h(\phi)^2 \left[\boldsymbol{\varepsilon}^* : \mathbb{C}_{\approx 0} : \boldsymbol{\varepsilon}^* - 2\boldsymbol{\varepsilon}_{\text{uni}} : (\mathbb{C}_{\approx 1} - \mathbb{C}_{\approx 0}) : \boldsymbol{\varepsilon}^* \right] + \\
&\frac{1}{2}h(\phi)^3 \left[\boldsymbol{\varepsilon}^* : (\mathbb{C}_{\approx 1} - \mathbb{C}_{\approx 0}) : \boldsymbol{\varepsilon}^* \right].
\end{aligned} \tag{6.10}$$

This also shows when regarding Figure 6.3. This is an advantage to the Voigt/Taylor approach. Numerical implementations, such as the finite element method, require second order derivatives. With the Khachaturyan approach, those derivatives don't vanish. A disadvantage of the Khachaturyan approach is the drop of the elastic energy in the interface. Simplifying (6.10) the magnitude of the drop can be quantified

$$f^{\text{u}}(\phi) = A_{f^{\text{u}}} + B_{f^{\text{u}}}h(\phi) + C_{f^{\text{u}}}h(\phi)^2 + D_{f^{\text{u}}}h(\phi)^3. \tag{6.11}$$

Assuming an arbitrary monotonically increasing function $h(\phi)$ on $\phi \in [0, 1]$ and $\phi' \in [0, 1]$, there exists a map k with $k(h(\phi)) = \phi$. That means that for every interpolation function h and another interpolation function h' of the same type sharing the same codomain, for every $\phi \in [0, 1]$, there is at least one ϕ' such that $h(\phi) = h'(\phi')$. Therefore the magnitude of the drop in (6.10) does not depend on the choice of h and can be determined by any h , for example $h(\phi) = 0$, without loss of generality

$$\frac{\partial f^{\text{u}}(\phi)}{\partial \phi} \stackrel{!}{=} 0, \text{ and } \phi = \frac{-C_{f^{\text{u}}} \pm \sqrt{C_{f^{\text{u}}}^2 - 3D_{f^{\text{u}}}B_{f^{\text{u}}}}}{B_{f^{\text{u}}}}. \tag{6.12}$$

That means that the interpolation of the elastic energy in the Khachaturyan approach is not necessarily limited by its bulk values, even if ϕ stays within $[0, 1]$. Similar to the Voigt/Taylor approach the first order derivative of the elastic energy w.r.t. the order parameter does not vanish. Therefore there is no extremal point which can lead to a driving force. As Figure 6.3 shows, this can be mitigated by choosing a cubic interpolation function such that the first order derivative is zero for the bulk phases, or by choosing a scaled tangens hyperbolicus interpolation function, which ensures that the codomain of the interpolation function is in the admissible range $[0, 1]$. To

summarize, the linear interpolation function can lead in both the Voigt/Taylor and the Khachaturyan approach to an unwanted driving force in the bulk phase. In most cases, with the interplay of the chemical energy, the order parameter does not notably exceed the interval $[0, 1]$. Mitigation can take place by forcing the order parameter within the admissible domain by using an obstacle potential such as proposed by Tschukin et al. (2017). As this approach may lead to instabilities using implicit time integration schemes, the same concept can be employed by a more flexible interpolation, by either choosing a interpolation with vanishing first order derivatives for the bulk phases, or by restricting the codomain. The Voigt/Taylor approach does not allow a linear interpolation because of the non-vanishing second order derivatives of the elastic energy. Table 6.1 sums up the behavior of the elastic energy using different interpolation methods in the Voigt/Taylor and the Khachaturyan approach.

6.3 Implementation

The Voigt/Taylor approach is implemented as user routine in the finite element analysis program FEAP (Taylor, 2014). The degrees of freedom are the vector valued order parameter $\underline{\phi} \in \mathbb{R}^n$ and the displacement vector \underline{u} . The number of phases considered is n . The number of spatial dimensions is d . As discussed above, the components of the order parameter are ϕ_α and indicate the presence of a phase α . They are associated with the corresponding transformation strain $\underline{\epsilon}_\alpha^*$ within the individual phase. The number of phases n depends on the number of martensitic orientation variants to be considered, which is intertwined with the orientation relationship. The fewest number of variants is the Bain orientation relationship. One orientation variant is introduced with each spatial dimension.

The field equations are the balance of linear and angular momentum for the mechanical problem, and the Ginzburg Landau time dependent evolution equation for the phase field problem

$$\underline{\nabla} \cdot \underline{\sigma} = 0, \quad (6.13)$$

$$\frac{\dot{\underline{\phi}}}{M} + \frac{\partial f^u}{\partial \underline{\phi}} + \frac{\partial f^{\text{ch}}}{\partial \underline{\phi}} - \underline{\nabla} \cdot \frac{\partial f^{\text{grad}}}{\partial \underline{\nabla} \otimes \underline{\phi}} = 0. \quad (6.14)$$

Subsequently, the flux-divergence theorem can be applied. Using Green's identity, the weak form of the mechanical and the weak form of the phase field problem is obtained. They read

$$\int_V (\underline{\nabla} \otimes \underline{\eta}_u) : \underline{\sigma} dV = \int_{\partial V_t} \underline{\eta}_u \cdot (\underline{\sigma} \underline{n}) dS \quad (6.15)$$

$$\int_V \left[\frac{\dot{\phi}_\alpha}{M} \eta_{\phi_\alpha} + \frac{\partial f^u}{\partial \phi_\alpha} \eta_{\phi_\alpha} + \frac{\partial f^{\text{ch}}}{\partial \phi_\alpha} \eta_{\phi_\alpha} + (\underline{\nabla} \phi_\alpha) \cdot (\underline{\nabla} \eta_{\phi_\alpha}) \right] dV = \int_{\partial V_q} \eta_{\phi_\alpha} (\underline{\nabla} \phi_\alpha \cdot \underline{n}) dS \quad (6.16)$$

where \underline{n} is the outer normal vector. The test functions for the mechanical and the chemical problem are $\underline{\eta}_u$, and $\underline{\eta}_\phi$. The values \underline{u} and $\underline{\phi}$ are discretized with nodal ansatz functions N_I . The index of the node is represented with I . A superset h indicates a discretized quantity (\cdot^h). They can be calculated using the ansatz function and the nodal quantities. A nodal quantity is superset with a hat ($\hat{\cdot}_I$), where the index I

identifies the node. The discretizations read

$$\underline{u}^h = \sum_{I=1}^N N_I \hat{u}_I, \quad \text{and} \quad \underline{\phi}^h = \sum_{I=1}^N N_I \hat{\phi}_I, \quad (6.17)$$

where N is the number of element nodes. The discretizations for the strain and the gradient of the components of the order parameter ϕ_α are

$$\underline{\varepsilon} = \sum_{I=1}^N \underline{\mathcal{B}}_I^u \cdot \hat{u}_I \quad \text{and} \quad \underline{\nabla} \phi_\alpha = \int_{I=1}^N \underline{\mathcal{B}}_I^\phi \cdot \hat{\phi}_I, \quad (6.18)$$

respectively. The matrix $\underline{\mathcal{B}}_I^u$ can be determined by applying a discretization to the small strain tensor in (2.18). Analogously, the matrix $\underline{\mathcal{B}}_I^\phi$ is obtained by applying the gradient to both sides of the discretization for the order parameter in (6.17). The matrices read

$$\underline{\mathcal{B}}_I^u = \begin{bmatrix} N_{,1} & 0 & 0 \\ 0 & N_{,2} & 0 \\ 0 & 0 & N_{,3} \\ 0 & N_{,3} & N_{,2} \\ N_{,3} & 0 & N_{,1} \\ N_{,2} & N_{,1} & 0 \end{bmatrix}, \quad \text{and} \quad \underline{\mathcal{B}}_I^\phi = \underline{\nabla} N_I \in \mathbb{R}. \quad (6.19)$$

6.3.1 Residual and Elemental Stiffness Matrix

Using the weak forms, the nodal residual vector can be determined. The nodal degrees of freedom \hat{d}_J , and $\hat{\underline{d}}_J$ at a node J are the displacements and the order parameter, as well as the time derivatives, reading

$$\hat{d}_J = \begin{bmatrix} \hat{u}_J \\ \hat{\phi}_J \end{bmatrix}, \quad \text{and} \quad \hat{\underline{d}}_J = \begin{bmatrix} 0 \\ \hat{\phi}_J \end{bmatrix}, \quad (6.20)$$

where the problem is quasi static for the mechanical model. The nodal displacements \hat{u}_J , and the nodal phase field parameter $\hat{\phi}_J$ and its rates $\hat{\underline{\phi}}_J$ are vectors

$$\hat{u}_J \in \mathbb{R}^d, \quad \hat{\phi}_J \in \mathbb{R}^n, \quad \text{and} \quad \hat{\underline{\phi}}_J \in \mathbb{R}^n. \quad (6.21)$$

The number of martensitic phases is n . It depends on the number of martensitic variants to be considered. The number of spatial dimensions d is 2 in the 2D case, and 3 in the 3D case. The nodal residual of a node I is a function of the nodal degrees of freedom and their rates

$$\underline{R}_I = \begin{bmatrix} \underline{R}_I^u \\ \underline{R}_I^\phi \end{bmatrix}, \quad \text{where} \quad \underline{R}_I^\phi = \begin{bmatrix} \underline{R}_I^{\phi_1} \\ \vdots \\ \underline{R}_I^{\phi_n} \end{bmatrix} \in \mathbb{R}^n. \quad (6.22)$$

The residual \underline{R}_I^ϕ for the phase field problem is a vector of residuals $\underline{R}_I^{\phi_\alpha}$ of the components ϕ_α of the vector valued order parameter $\underline{\phi}$. The residuals for the mechanical

and the phase field problem are \underline{R}_I^u and $\underline{R}_I^{\phi\alpha}$, respectively. They read

$$\underline{R}_I^u = \int_V \left(\underline{B}_I^{u\top} \right) \underline{\sigma} dV \quad (6.23)$$

$$\underline{R}_I^{\phi\alpha} = \int_V \left[\frac{\dot{\phi}_\alpha}{M} N_I + \frac{\partial f_u}{\partial \phi_\alpha} N_I + \frac{\partial f_{ch}}{\partial \phi_\alpha} N_I + GL(\nabla \phi_\alpha) \cdot \underline{B}_I^\phi \right] dV. \quad (6.24)$$

The component wise notation in (6.24) can also be expressed with the vector valued order parameter $\underline{\phi}$, effectively summarizing (6.24) and the right side of (6.22)

$$\underline{R}_I^\phi = \int_V \left[\frac{\dot{\phi}}{M} N_I + \frac{\partial f_u}{\partial \underline{\phi}} N_I + \frac{\partial f_{ch}}{\partial \underline{\phi}} N_I + GL(\nabla \otimes \underline{\phi})^\top \cdot \underline{B}_I^\phi \right] dV. \quad (6.25)$$

The stiffness matrix represents the change of the nodal residual w.r.t the nodal degrees of freedom. The size of the elemental stiffness matrix \underline{K} depends on the number of element nodes N , and the number of degrees of freedom $n + d$

$$\underline{K} = \begin{bmatrix} \underline{K}_{11} & \cdots & \underline{K}_{1J} & \cdots & \underline{K}_{1N} \\ \vdots & \ddots & \vdots & \ddots & \vdots \\ \underline{K}_{I1} & \cdots & \underline{K}_{IJ} & \cdots & \underline{K}_{IN} \\ \vdots & \ddots & \vdots & \ddots & \vdots \\ \underline{K}_{N1} & \cdots & \underline{K}_{NJ} & \cdots & \underline{K}_{NN} \end{bmatrix} \in \mathbb{R}^{N(n+d) \times N(n+d)}. \quad (6.26)$$

The stiffness matrix \underline{K}_{IJ} for the node pair I and J can be divided up into a purely mechanical part K_{IJ}^{uu} , and a purely phase field dependent part $K_{IJ}^{\phi\phi}$ on the diagonal. The mixed terms $K_{IJ}^{u\phi}$, and $K_{IJ}^{\phi u}$, which arise due to the coupling of the phase field model with the material law through the elastic energy, are on the antidiagonal. The elemental stiffness matrix reads

$$\underline{K}_{IJ} = \frac{\partial \underline{R}_I}{\partial \underline{d}_J} = \begin{bmatrix} K_{IJ}^{uu} & K_{IJ}^{u\phi} \\ K_{IJ}^{\phi u} & K_{IJ}^{\phi\phi} \end{bmatrix}, \text{ where } K_{IJ}^{uu} \in \mathbb{R}^{d \times d}, \text{ and } K_{IJ}^{\phi\phi} \in \mathbb{R}^{n \times n}. \quad (6.27)$$

The stiffness matrix represents the change of the residual when varying the nodal degrees of freedom. The matrix entries can be determined by the derivative of the residual w.r.t the individual nodal degrees of freedom. The stiffness matrix entries for the mechanical problem are

$$K_{IJ}^{uu} = \frac{\partial \underline{R}_I^u}{\partial \underline{u}_J} = \frac{\partial \underline{R}_I^u}{\partial \underline{\varepsilon}} \frac{\partial \underline{\varepsilon}}{\partial \underline{u}_J} = \int_V \left(\underline{B}_I^u \right)^\top \frac{\partial \underline{\sigma}}{\partial \underline{\varepsilon}} \left(\underline{B}_J^u \right) dV. \quad (6.28)$$

Analogously, the entries of the stiffness matrix for the phase field problem can be determined. First, however, it is useful to determine their entries

$$K_{IJ}^{\phi\phi} = K_{IJ}^{\phi\alpha\phi\beta} \underline{e}_\alpha \otimes \underline{e}_\beta, \quad (6.29)$$

where \underline{e}_α and \underline{e}_β represent the unit vectors introduced in chapter 4.1. The entries read

$$\begin{aligned} K_{IJ}^{\phi\alpha\phi\beta} &= \frac{\partial \underline{R}_I^{\phi\alpha}}{\partial \hat{\phi}_{\beta J}} = \int_V \left[\frac{\partial^2 (f^{\text{ch}} + f^{\text{u}})}{\partial \phi_\alpha \partial \phi_\beta} N_I N_J + GL \underline{B}_I^\phi \frac{\partial (\nabla \phi_\alpha)}{\partial (\nabla \phi_\beta)} \frac{\partial (\nabla \phi_\beta)}{\partial \hat{\phi}_{\beta J}} \right] dV \\ &= \int_V \left[\frac{\partial^2 (f^{\text{ch}} + f^{\text{u}})}{\partial \phi_\alpha \partial \phi_\beta} N_I N_J + GL \underline{B}_I^\phi \delta_{\alpha\beta} \underline{B}_J^\phi \right] dV. \end{aligned} \quad (6.30)$$

Expressing (6.30) using a vector, the stiffness matrix becomes

$$K_{IJ}^{\phi\phi} = \int_V \left[\frac{\partial^2 f^{\text{ch}}}{\partial \underline{\phi}^2} N_I N_J + \frac{\partial^2 f^{\text{u}}}{\partial \underline{\phi}^2} N_I N_J + GL \underline{B}_I^\phi \underline{I} \underline{B}_J^\phi \right] dV. \quad (6.31)$$

The mixed entries follow symmetry in I and J , such that

$$K_{IJ}^{\underline{u}\phi} = \left(K_{IJ}^{\phi\underline{u}} \right)^\top = K_{JI}^{\phi\underline{u}} \quad (6.32)$$

holds. This can be shown by calculating both entries. The top-right antidiagonal entry can be expressed in vector notation directly, yielding

$$K_{IJ}^{\underline{u}\phi} = \frac{\partial \underline{R}_I^{\underline{u}}}{\partial \hat{\phi}_{\beta J}} = \int_V (\underline{B}_I^{\underline{u}})^\top \frac{\partial \underline{\sigma}}{\partial \hat{\phi}_{\beta J}} dV = \int_V (\underline{B}_I^{\underline{u}})^\top \frac{\partial \underline{\sigma}}{\partial \underline{\phi}} N_J dV. \quad (6.33)$$

The bottom-left antidiagonal entry is calculated using the component wise notation of the order parameter

$$\begin{aligned} K_{IJ}^{\phi\alpha\underline{u}} &= \frac{\partial \underline{R}_I^{\underline{u}}}{\partial \hat{\phi}_{\alpha J}} = \int_V \frac{\partial^2 (f^{\text{ch}} + f^{\text{u}})}{\partial \phi_\alpha \partial \hat{u}_J} N_I dV \\ &= \int_V \frac{\partial}{\partial \phi_\alpha} \left(\frac{\partial f^{\text{u}}}{\partial \underline{\varepsilon}} \frac{\partial \underline{\varepsilon}}{\partial \hat{u}_J} \right) N_I dV \\ &= \int_V \frac{\partial (\underline{\sigma}^\top \underline{B}_J^{\underline{u}})}{\partial \phi_\alpha} N_I dV = \int_V N_I \left(\frac{\partial \underline{\sigma}}{\partial \phi_\alpha} \right)^\top \underline{B}_J^{\underline{u}} dV. \end{aligned} \quad (6.34)$$

Replacing the derivative of the strain w.r.t the order parameter component ϕ_α with its vector notation counterpart, the symmetry can be shown

$$K_{IJ}^{\phi\underline{u}} = \left(K_{IJ}^{\underline{u}\phi} \right)^\top = \int_V N_I \left(\frac{\partial \underline{\sigma}}{\partial \underline{\phi}} \right)^\top \underline{B}_J^{\underline{u}} dV. \quad (6.35)$$

The elemental damping matrix \underline{D} contains the derivatives of the residual w.r.t to the nodal rates $\hat{\underline{d}}_J$. In view of (6.26) and (6.26), the elemental damping matrix entries are

$$\underline{D}_{IJ} = \frac{\partial \underline{R}_I}{\partial \hat{\underline{d}}_J} = \begin{bmatrix} \underline{0} & \underline{0} \\ \underline{0} & \underline{D}_{IJ}^{\phi\phi} \end{bmatrix}. \quad (6.36)$$

The terms concerned with the mechanical part of the problem vanish as they are considered to be quasi static. The pure phase field damping matrix is a diagonal matrix

$$\underline{D}_{IJ}^{\phi\phi} = \int_V \frac{N_I}{M} \underline{I} dV \in \mathbb{R}^{n \times n}. \quad (6.37)$$

With the nodal residual vector \underline{R}_I^ϕ , and the corresponding stiffness and damping matrices \underline{K}_{IJ} and \underline{D}_{IJ} , respectively, the field equations in (6.13) and (6.14) can be solved. The time integration is carried out with the backward Euler implicit method.

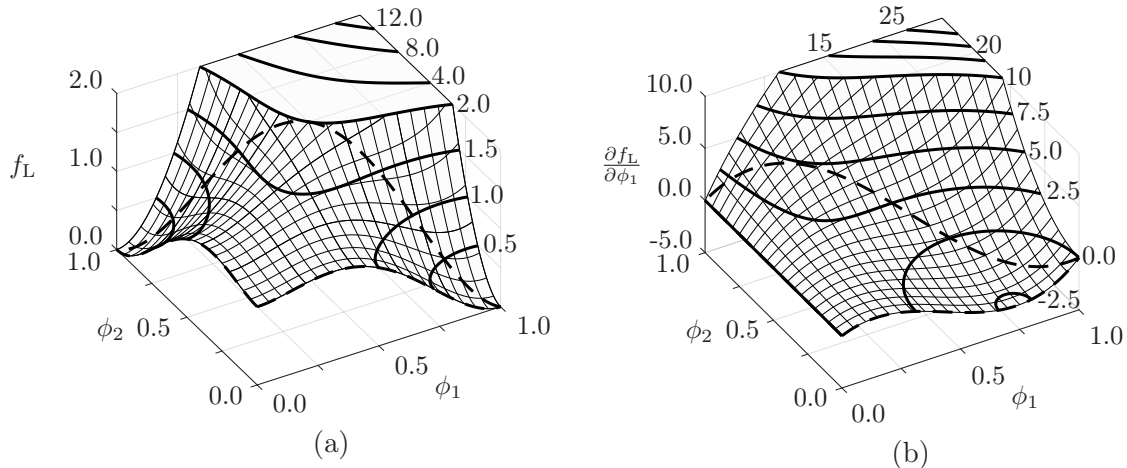


FIGURE 6.4: Landau polynomial f_L for $A = 10$ and $D = 1$ as a function of two order parameter components ϕ_1 and ϕ_2 (a). The derivative w.r.t. ϕ_1 is shown in (b). The thick lines indicate contour lines of constant height. Contour lines above 2 in (a) and above 10 in (b) are projected down to the height of 2 and 10, respectively. The boundary of the admissible range is indicated by the dashed lines (-).

6.3.2 Derivatives of the Elastic Energy

The elastic energy in the Voigt/Taylor approach is an interpolation of the elastic energies within the individual phases. In view of (6.3) and (6.4), derivatives of the elastic energy w.r.t the vector valued order parameter $\underline{\phi}$ can be provided with the knowledge of the stress $\underline{\sigma}_\alpha$, and the elastic energy f_α^u of the phases $\alpha = 0 \dots n$, as well as providing first and second order derivatives for the scalar interpolation function h . Using the case dependent approach in (4.29), the derivatives of the elastic energy w.r.t the order parameter read

$$\frac{\partial f^u}{\partial \phi_\alpha} = f_0^u \frac{\partial h^0(\underline{\phi})}{\partial \phi_\alpha} + \sum_{\alpha=1}^n f_\alpha^u \frac{\partial h(\phi_\alpha)}{\partial \phi_\alpha} = h'(\phi_\alpha)(f_\alpha^u - f_0^u), \quad \text{and} \quad (6.38)$$

$$\frac{\partial^2 f^u}{\partial \phi_\alpha \partial \phi_\beta} = \begin{cases} h''(\phi_\alpha), & \text{if } \alpha = \beta \\ 0, & \text{if } \alpha \neq \beta \end{cases}. \quad (6.39)$$

Using the case dependent interpolation for the mixed terms in (6.33) and (6.35), the derivative is given by

$$\frac{\partial \underline{\sigma}}{\partial \phi_\alpha} = \underline{\sigma}_0 \frac{\partial h^0(\underline{\phi})}{\partial \phi_\alpha} + \sum_{\alpha=1}^n \underline{\sigma}_\alpha \frac{\partial h(\phi_\alpha)}{\partial \phi_\alpha} = h'(\phi_\alpha)(\underline{\sigma}_\alpha - \underline{\sigma}_0). \quad (6.40)$$

6.3.3 Derivatives of the Chemical Energy

The chemical energy is a function of the vector valued order parameter. In contrast to the derivatives of the elastic energy, they need to be implemented individually. Following Schmitt, Kuhn, Müller, and Bhattacharya (2014) and Yamanaka, Takaki, and Tomita (2008), the chemical energy is proportional to a multivariant Landau polynomial

$$f^{\text{ch}}(\underline{\phi}) = GLf_L(\underline{\phi}), \quad (6.41)$$

where G is the specific interface energy density and L is a parameter related with the width of the smooth transition zone in the phase field model. The Landau polynomial is given by

$$f_L(\underline{\phi}) = D + \frac{1}{2}A \sum_{\alpha=1}^n [\phi_\alpha^2] - \frac{1}{3}B \sum_{\alpha=1}^n [\phi_\alpha^3] + \frac{1}{4}C \left[\sum_{\alpha=1}^n [\phi_\alpha^2] \right]^2. \quad (6.42)$$

Figure 6.4 (a) depicts the Landau polynomial for two phases ($n = 2$). As discussed in chapter 5, the parameter D identifies the stable and the metastable phases, whereas A scales the maximum of the Landau polynomial. As a consequence, the parameters of the Landau polynomial are temperature dependent. Here, a constant temperature is assumed. The multivariate Landau polynomial and its first order derivative are depicted in Figure 6.4. The Landau polynomial f_L exhibits three minima at $\underline{\phi} = [0, 0]$, at $\underline{\phi} = [0, 1]$, and at $\underline{\phi} = [1, 0]$, where the latter two are stable minima. The dashed lines indicate the boundary of the admissible region of the order parameter. The gradient outside this admissible region points towards the inside. That means there is no purely stable chemical state here. The derivative of the Landau polynomial $\partial f_L / \partial \phi_1$ w.r.t. the first order parameter ϕ_1 in Figure 6.4 (b) vanishes for the three minima. The same applies for the second order parameter ϕ_2 . That means there are no chemical driving forces in either of the stable and metastable minima. In Schneider, Schoof, Huang, Selzer, and Nestler (2016), a so called third phase term is introduced, in order to mitigate an unphysical minimum on a triple junction of the phase field. As both first order derivatives vanish only in the bulk phases, e.g.

$$\left. \frac{\partial f_L}{\partial \phi_1} \right|_{\underline{\phi}} \cdot \left. \frac{\partial f_L}{\partial \phi_1} \right|_{\underline{\phi}} \stackrel{!}{=} 0 \implies \phi \in [0, \underline{e}_1, \underline{e}_2], \quad (6.43)$$

it is not necessary to introduce a third phase term. Visually, that means that the height lines of the first order derivatives only intersect in the bulk phases.

6.3.4 Technical Details

The model has been implemented in the finite element framework FEAP (Taylor, 2014) and the finite element solver Zébulon for verification purposes. For the implementation in FEAP Fortran 95 was used. The advantage of Fortran 95 over Fortran 77 is the free form, making code more readable. Furthermore it allows for dynamic memory allocation and with the introduction of modules, it makes testing and development more versatile. For example Fortran modules interface with Python 3 using the f2py compiler. In order to compile Fortran 95 source code along with FEAP, the sources in the concerning makefiles need to be adjusted

```
SOURCES = $(sort $(wildcard $(FSOURCE)*.$(FEXT)) $(wildcard $(CSOURCE)
  ↪ *.$(CEXT)) $(wildcard $(FSOURCE)*.f95))
```

The \hookrightarrow indicates a line break. The Fortran 95 source files are selected with the wildcard expansion. Sorting the source files using $\$(sort \dots)$ and setting the system locale to C ensures a consistent order across systems. Prefixing the module with a 0 ensures that they are compiled prior to all the element files. In order to access the module subroutines within python, which is useful for plotting, testing and verification, the command

```
python3 -m numpy.f2py -c feap_sources -m python_module
```

can be used, where *feap_sources* is a list of the feap source module files, in order to create a python module of the name *python_module*.

The model has been implemented in 2D using 4 node quadrilateral element, and in 3D using 8 node brick elements. Three interpolation functions are available. The code has been generalized to accommodate n phases.

6.4 Basic Considerations

The Voigt/Taylor model should be able to reproduce the effects found in the Khachaturyan model. Therefore martensite is the metastable phase for temperatures below the equilibrium temperature. With no load applied, the martensitic phase is stable. However, depending on the load state, the austenitic face can be more favorable, as the martensitic transformation introduces an eigenstrain. However, the eigenstrain, depends on the martensitic orientation variant. Likewise, one martensitic orientation variant might be more favorable than another variant.

Here, a beam of 176 nm length and 35.2 nm height at a constant temperature of $T = 300$ K in two spatial dimensions is considered. With the temperature dependent separation potential presented in chapter 5, the parameters of the Landau polynomial can be determined according to Schmidt et al. (2016) and Schmidt, Dornisch, and Müller (2017a), where

$$A = 9.7187, \quad B = 41.1562, \quad C = 31.4375, \quad \text{and } D = 1. \quad (6.44)$$

correspond to a temperature of $T = 300$ K. The $D = 1$ indicates that martensite is the stable phase, and austenite is the metastable phase. The formulation in the residuals (6.24), and the tangent matrix entries (6.28), (6.30), and (6.33), require the stress $\boldsymbol{\sigma}_\alpha$, the derivative of the stress w.r.t. strain $\frac{\partial \boldsymbol{\sigma}_\alpha}{\partial \boldsymbol{\xi}_\alpha}$, and the elastic energy f_α^u of each individual phase α . Any material law, providing the aforementioned measures, can be chosen. Here, a linear elastic material law with constant eigenstrain is used. The material law can be expressed using the following equations

$$\boldsymbol{\xi}_\alpha^e = \boldsymbol{\xi}_\alpha - \boldsymbol{\xi}_\alpha^*, \quad (6.45)$$

$$f_\alpha^u = \frac{1}{2} \boldsymbol{\xi}_\alpha^e : \mathbb{C}_\alpha : \boldsymbol{\xi}_\alpha^e, \quad (6.46)$$

$$\boldsymbol{\sigma}_\alpha = \frac{\partial f_\alpha^u}{\partial \boldsymbol{\xi}_\alpha} = \mathbb{C}_\alpha : \boldsymbol{\xi}_\alpha^e, \quad \text{and} \quad (6.47)$$

$$\frac{\partial \boldsymbol{\sigma}_\alpha}{\partial \boldsymbol{\xi}_\alpha} = \mathbb{C}_\alpha, \quad (6.48)$$

where the material constants are represented by \mathbb{C}_α . For the austenitic parent phase ($\alpha = 0$), no eigenstrain is assumed. The eigenstrain in the martensitic phases varies. In order to discuss the influence of the eigenstrain in the results, they have been simplified

$$\boldsymbol{\xi}_1^* = \begin{bmatrix} 0.05 & 0 \\ 0 & 0 \end{bmatrix}, \quad \text{and} \quad \boldsymbol{\xi}_2^* = \begin{bmatrix} 0 & 0 \\ 0 & 0.05 \end{bmatrix}, \quad (6.49)$$

such that the first orientation variant imposes a strain in x_1 -direction, and the second strain imposes a strain in x_2 -direction. Therefore a strain, or force in x_1 -direction influences the elastic energy and therefore the formation of the first orientation variant strongly compared to the formation of the second orientation variant, which is unaffected, with the exception of effects like the lateral strain. The same applies for a strain, or force in x_2 -direction, and the second orientation variant, however, interchanged. Furthermore, a total strain of 5% is well within the small strain regime. Given such a strain setting, it is possible choosing the right load setting, to make either the austenitic or the martensitic phase energetically more stable.

Consider a beam under load, realized as displacement of the far ends of the beam

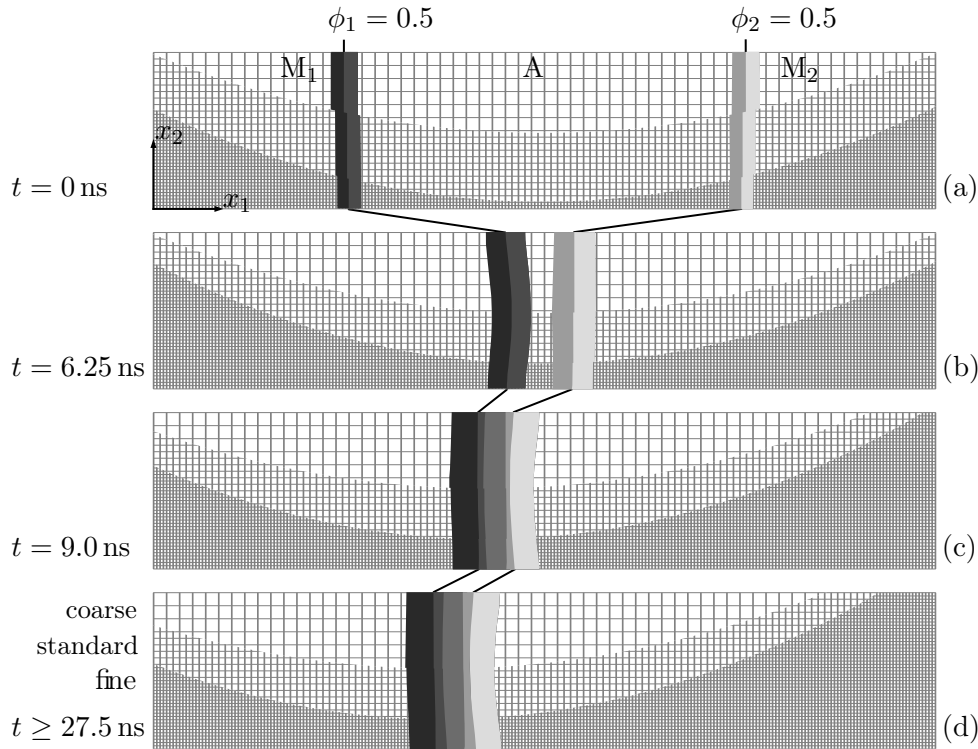


FIGURE 6.5: Time evolution for different levels of mesh refinements. The solid colored regions indicate the interface region where $0.8 > \phi_1 > 0.2$ (left, dark gray), and where $0.8 > \phi_2 > 0.2$ (right, light gray). The austenitic phase is present in the center (A), with the martensitic orientation variants to the left (M_1) and to the right (M_2).

about on another. The bottom left node is pinned. The bottom right node is a simple support allowing for movement in x_1 -direction only. The left side of the beam is held in place in x_1 -direction only, allowing for movement in x_2 -direction. The right side is displaced by a certain magnitude, however without restricting motion in x_2 -direction. The initial condition is shown in 6.5 (a). The middle section of the beam endowed with the austenitic phase, where the left quarter and the right quarter contain the pure martensitic orientation variant one and two, respectively.

Before discussing the simulation, some basic considerations for the stability of the phases are presented. First, disregard the elastic energy, or assume the elastic energy is equal for each individual phase. Therefore, in order to minimize the free energy, the chemical energy is to be minimized. Here, as a temperature of about 300 K is assumed, the martensitic phase is more stable. As the eigenstrain can no longer amount for differences, the martensitic phases are chemically and mechanically equal. Due to geometric symmetry, simulation wise, the interfaces M_1 -A and M_2 -A would progress at the same speed and eventually meet in the center.

Second, disregard the chemical energy, considering the mechanical energy only. Furthermore, assume no lateral strain, and no varying material constants $\underset{\approx}{\mathcal{C}}_{\alpha}$. Here, in terms of elastic energy, the austenitic phase and the second orientation variant are equal. The displacement on the right side of the beam is varied between 0 and 8.8 nm, which amounts to a total strain of 5%. If the displacement is 8.8 nm, the elastic energy in the first orientation variant is smaller than the elastic energy in the austenitic and the second orientation variant. Therefore the interface M_1 -A would proceed to evolve

to the right, passing the interface M_2 -A, and leading eventually to a beam of pure martensite M_1 . Any strain above or equal to 5% leads to the same final configuration. Given a total strain of 0, however, the austenitic phase is more stable than the first orientation variant. This leads to a motion of the M_1 -A to the left, while the M_2 -A interface does not move as the austenitic phase and the second orientation variant are energetically equal. The end configuration is a beam of austenite, with a portion of retained martensite M_2 beyond the M_2 -A interface. Therefore the end configuration can be determined by the position of the M_1 -A interface only. Any strain smaller or equal to 0 leads to the same final configuration. Given a displacement between 0 nm and 8.8 nm, however, the final configuration is determined by the position of the M_1 -A interface only. For example given a displacement of 4.4 nm (2.5%), the position of the M_1 -A interface would be at about 50% length of the beam, as then the eigen-strain within the first orientation variant amounts for the displacement. Therefore, in this case, the following relation for the position of the interface $x_{1(M_1-A)}$ can be determined

$$x_{1(M_1-A)} = \frac{d}{\varepsilon_{11}} l, \quad (6.50)$$

where l is the length of the beam, and d is the displacement applied on the right side. For example a strain of 2%, tantamount to a displacement of $d = 3.52$ nm, leads to a position of the M_1 -A interface of $x_{(M_1-A)} = 70.4$ nm, neglecting the chemical energy and the lateral strain. Likewise, a displacement of 5.28 nm (3% total strain) yields an interface position of $x_{1(M_1-A)} = 105.6$ nm.

The simulation in Figure 6.5 assumes the elasticity matrices of pure iron for the austenitic and the martensitic phase, given by

$$\mathcal{C}_0 = \mathcal{C}_{\text{Fe, fcc, simpl.}} = \begin{bmatrix} 2.2 & 1.5 & 0 \\ 1.5 & 2.2 & 0 \\ 0 & 0 & 0.3 \end{bmatrix} \cdot 10^5 \text{ N mm}^{-2}, \text{ and} \quad (6.51)$$

$$\mathcal{C}_1 = \mathcal{C}_2 = \mathcal{C}_{\text{Fe, bcc, simpl.}} = \begin{bmatrix} 2.9 & 1.6 & 0 \\ 1.6 & 2.9 & 0 \\ 0 & 0 & 0.6 \end{bmatrix} \cdot 10^5 \text{ N mm}^{-2}. \quad (6.52)$$

Please note, that in contrast to (Schmitt, Wang, and Urbassek, 2013b), the parameters have been simplified. However, they are in the right order of magnitude. That is in line with the transformation strain ε_α^* chosen in (6.49). As an initial guess, the parameters for the chemical energy and the time evolution are

$$G = 0.96 \cdot 10^{-6} \frac{\text{J}}{\text{mm}}, \quad L = 30 \text{ nm}, \quad \text{and} \quad M = 9.6 \cdot 10^{-3} \frac{\text{mm}}{\text{N ns}}, \quad (6.53)$$

In Figure 6.5 the initial configuration (a), and the time evolution (b, c), leading to the final configuration (d) are shown. The displacement is $d = 3.52$ nm. Initially, the motion of the interface M_1 -A is to the right, and of the interface M_2 -A to the left. This leads to a transformation of the austenitic phase to the first and the second orientation variant, respectively. That means, that both martensitic orientation variants are energetically more stable than the austenitic phase. This can be explained illustratively: Both the first and the second martensitic orientation variant are chemically more stable than the austenitic phase. As the strain of the beam is in x_1 -direction, the transformation strain entry $\varepsilon_{11\alpha}^*$ is of importance. In terms of the elastic energy, the second orientation variant and the austenitic phase are almost equal, where the

TABLE 6.2: Interface position

mesh	n_{el}	$n_{\text{el}x_1}$	$n_{\text{el}x_2}$	$n_{\text{el}x_1} \frac{L}{l}$	$x_{1(\text{M}_1-\text{A})}$
coarse	720	60	12	10.23	67.48 nm
standard	2880	120	24	20.45	67.54 nm
fine	11520	240	48	40.91	67.55 nm
analytic	-	-	-	-	70.4 nm

transformation strain entries vanish ($\varepsilon_{110}^* = \varepsilon_{111}^* = 0$). However due to the chemical energy, the second martensitic orientation variant is preferred to the austenite. The interface motion between the time frames is indicated schematically by the lines connecting the contours of constant $\phi_1 = 0.5$, and $\phi_2 = 0.5$.

The velocity of the M_2 -A interface is marginally higher than the velocity of the M_1 -A interface. That is because the second martensitic orientation variant is, in terms of the elastic energy, slightly more favorable than the first martensitic orientation variant. The phases move towards each other as depicted in Figure 6.5 (b). Eventually, they join, forming a mutual interface. Thereafter, they proceed to move towards the left as shown in Figure 6.5 (c). As both martensitic phases are chemically equally stable, equation (6.50) provides a good approximation for the final configuration. Considering the elastic energy only, with no lateral strain and without varying elasticity matrices, this leads to an interface position of 70.4 nm. The interface position in the simulations can be calculated by averaging the x_1 -position where $\phi_1 = \phi_2$ over the x_2 -coordinate. The simulation has been conducted with three differently refined meshes, termed coarse, standard, and fine. The standard mesh consists of 2880 elements, while the coarse mesh is four times coarser amounting to 720 elements. The fine mesh is at 11520 elements. The positions for the interface M_1 - M_2 are at 67.48 nm for the coarse mesh, 67.54 nm for the standard refined mesh, and 67.55 nm for the fine mesh. This is well in line with the prediction in (6.50). The results are summed up in Table 6.2, where in addition to the number of elements in x_1 and in x_2 direction, $n_{\text{el}x_1}$, and $n_{\text{el}x_2}$, respectively, the mesh density as elements per specific interface width L is given ($n_{\text{el}x_1} \frac{L}{l}$). The coarse mesh has about 10 elements per interface width L , where the values for the standard and the fine mesh are twofold and fourfold higher. As the result for the coarse mesh does not considerably vary from the fine mesh, even less so the result obtained using the standard mesh, a number of ten elements per interface width L is sufficient.

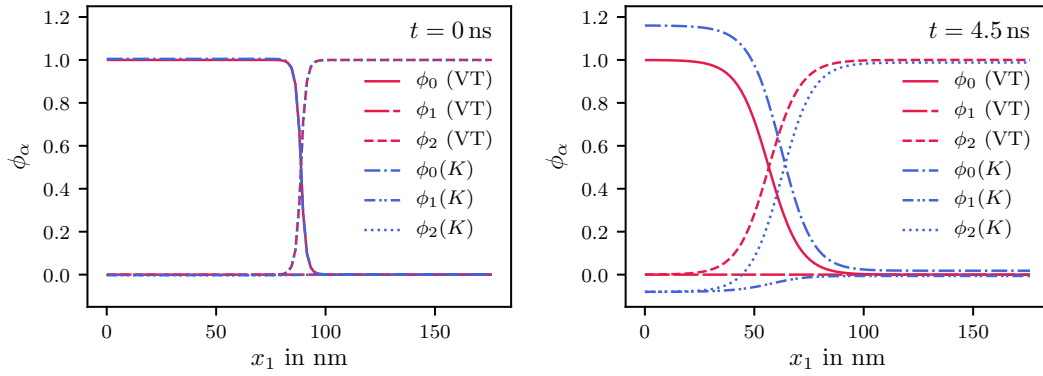


FIGURE 6.6: Example 1. Order parameter for the parent phase ϕ_0 (solid, dash-dot), and the martensitic orientation variants ϕ_1 (dashes-dash-dot-dot), and ϕ_2 (small dashes, dots) for the Khachaturyan (K, blue), and the Voigt/Taylor approach (VT, red). The static iteration is on the left, the evolution after $t = 4.5$ ns is on the right.

6.5 Comparison to the Khachaturyan Approach

In this chapter a comparison to the Khachaturyan in chapter 5 approach is presented. The material parameters are similar to the ones used in the previous section. As before, a beam of 176 nm length and 35.2 nm height at a constant temperature of $T = 300$ K in two spatial dimensions is considered, where the bottom left node is pinned, and the bottom right node is a simple support, allowing for motion in x_2 -direction only. A cubic interpolation function is used for the Voigt/Taylor approach.

Three examples with varying material parameters and boundary conditions are discussed in order to assert their influence. The first example is shown in Figure 6.6 and 6.7. Here, different elastic constants for the individual phases are used, they are given by

$$\mathcal{C}_0 = \mathcal{C}_{\text{Fe, fcc, simpl.}} \text{ and } \mathcal{C}_1 = \mathcal{C}_2 = \mathcal{C}_{\text{Fe, bcc, simpl.}} \quad (6.54)$$

where the parameters are given in (6.52). In order to attribute elastic constants, no transformation strain is assumed

$$\boldsymbol{\varepsilon}_0^* = \boldsymbol{\varepsilon}_1^* = \boldsymbol{\varepsilon}_2^* = \mathbf{0}. \quad (6.55)$$

A distributed load in x_1 -direction of $F = 1 \cdot 10^{-3}$ N is applied to the far ends of the beam, leading to a total strain within the order of magnitude of 3%. The initial configuration after the static iteration at $t = 0$ ns, and the evolution after $t = 4.5$ ns are shown in Figure 6.6. The distribution of the elastic and the chemical energy is shown in Figure 6.7, again after the static iteration and after evolving for 4.5 ns. After the static iteration, there is no difference between the Khachaturyan and the Voigt/Taylor case. The elastic energy reaches its bulk value in the bulk phases, given the local strain distribution. The chemical energy vanishes in the bulk child phases, where $\phi_0 = 0$ due to the nature of the Landau polynomial (6.4). In the austenitic phase, it reaches a value of $G/L = 0.32$ MJ m $^{-2}$. Both models rely on energy minimization. A transformation from any bulk phase to any other bulk phase introduces an interface, which is widened due to the gradient term. Once the interface is established, the energy contribution of the chemical energy wants to minimize the interface width, therefore counteracting the gradient term and thus stabilizing the interface. As does

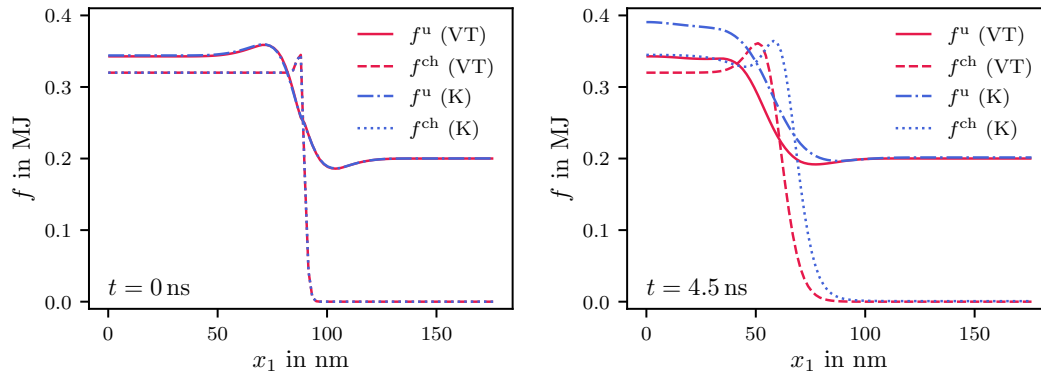


FIGURE 6.7: Example 1. Elastic energy f^u (solid, dash-dot) and chemical energy f^{ch} (dashes, dots) for the Khachaturyan (K, blue), and the Voigt/Taylor approach (VT, red). The static iteration is shown on the left, the evolution after $t = 4.5$ ns is on the right

the mechanical energy. As the terms counteract themselves on the interface, they are disregarded momentarily.

The elastic and the chemical energy, f^u and f^{ch} , respectively, are an indicator for the stable solution of this problem: The global minimum is a transformation from the austenitic to the martensitic phase. A transformation releases not only chemical, but also mechanical energy.

During the transformation, the interface widenes. At 4.5 ns, an intermediate state is reached. The interface position, where $\phi_0 = \phi_2$ is almost equal for the two approaches. In the Voigt/Taylor approach, the bulk values for both the elastic and the chemical energy are assumed. The chemical setup is austenitic to the left of the interface where $\phi_0 = \phi_2$, and it is martensitic to the right. The first orientation variant is absent. At all times prior and after this intermediate state, the respective bulk values for the elastic energy are reached. The phase field stays within the admissible range.

However using the Khachaturyan approach, the chemical and the elastic energy exceed the values for the bulk phases. A comparison with the phase field in Figure 6.7 at time $t = 4.5$ ns shows that the order parameter exceeds its valid range. That is due to the use of a linear interpolation function. This issue can be fixed, either by using a non-linear interpolation function, such as the cubic, ensuring that exceeding the values for the bulk phases leads to a bigger energy contribution than staying in the interface or the bulk. Likewise, a tangens hyperbolicus interpolation function could be used, limiting the codomain and thus extending the admissible range indefinitely. A third solution poses the obstacle potential (Tschukin et al., 2017).

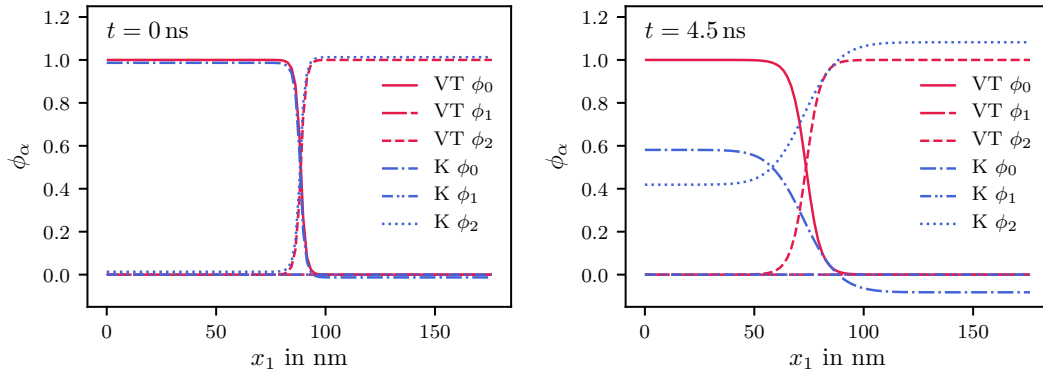


FIGURE 6.8: Example 2. Order parameter for the parent phase ϕ_0 (solid, dash-dot), and the martensitic orientation variants ϕ_1 (dashes-dash-dot-dot), and ϕ_2 (small dashes, dots) for the Khachaturyan (K, blue), and the Voigt/Taylor approach (VT, red). The static iteration is on the left, the evolution after $t = 4.5$ ns is on the right.

As a second test, in order to discuss the influence of the transformation strain, the material moduli are constant for all phases, e.g.

$$\mathcal{C}_0 = \mathcal{C}_1 = \mathcal{C}_2 = \mathcal{C}_{\text{Fe, fcc, simpl.}} \quad (6.56)$$

where the value for $\mathcal{C}_{\text{Fe, fcc, simpl.}}$ is in (6.52). A transformation strain is introduced for the second martensitic variant only

$$\boldsymbol{\varepsilon}_0^* = \boldsymbol{\varepsilon}_1^* = \mathbf{0}, \quad \text{and} \quad \boldsymbol{\varepsilon}_2^* = \begin{bmatrix} 0.05 & 0 \\ 0 & 0 \end{bmatrix}. \quad (6.57)$$

As discussed in chapter 6.4, a local strain, which is similar to the transformation strain, causes the transformation to be energetically beneficial. This example uses the same geometry as in the previous example, but the boundary conditions are modified. Instead of a load, a strain of 0.05 is applied to the far ends of the beam in x_1 -direction. In similar fashion, the phase composition in Figure 6.8 and the energy landscape in Figure 6.9 are discussed.

The static iterations of the Khachaturyan and the Voigt/Taylor approach differ slightly. Contrary to what was shown for the uniform strain case in Figure 6.3, the elastic energy of the Voigt/Taylor approach is exaggerated in the interface. Here, the strain is not uniform. That is due to the mismatch of the transformation strain and the interpolation of the elastic energy rather than interpolating the effective parameters as in the Khachaturyan approach. This is unfavorable for numerical implementations, as the interface needs to be resolved with a finer discretization. However, as shown in the previous chapter 6.4, a relatively coarse discretization leads to accurate results. A countermeasure would be to raise the parameter L , which scales the interface width. As the phases evolve, at 4.5 ns, an intermediate state is obtained. In the Khachaturyan approach, the interface is considerably wider. That is due to the lower and almost vanishing energy difference in the elastic energy. However, the order parameters ϕ_0 , and ϕ_2 exceed their valid range. This is not the case for the Voigt/Taylor approach.

The two examples shown in the Figures 6.6, 6.7, 6.8, and 6.9 all end with the same solution: a beam of pure martensite. In order to show that the results for the Khachaturyan and the Voigt/Taylor case may differ, the boundary condition of the previous

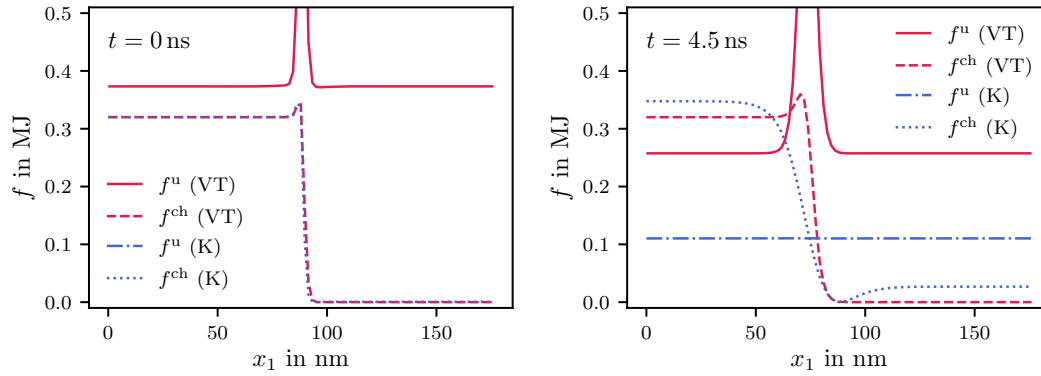


FIGURE 6.9: Elastic energy f^u (solid, dash-dot) and chemical energy f^ch (dashes, dots) for the Khachaturyan (K, blue), and the Voigt/Taylor approach (VT, red). The static iteration is shown on the left, the evolution after $t = 4.5$ ns is on the right

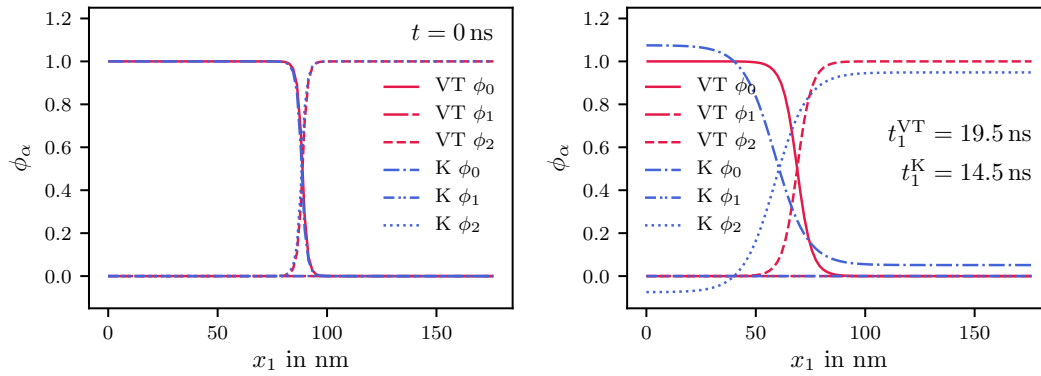


FIGURE 6.10: Example 3. Order parameter for the parent phase ϕ_0 (solid, dash-dot), and the martensitic orientation variants ϕ_1 (dashes, dash-dot-dot), and ϕ_2 (small dashes, dots) for the Khachaturyan (K, blue), and the Voigt/Taylor approach (VT, red). The static iteration is on the left, the stable state after the evolution is on the right.

example are modified. The strain is reduced to 0.025. Disregarding the chemical energy, the position of the interface can be calculated with (6.50). That means, in terms of the mechanical energy, the initial configuration is in a stable state with the interface in the center. Adding the chemical energy, the position should shift to the left, as martensite is chemically more stable. Figure 6.10 shows the phase field in the initial configuration and the final configuration. The Voigt/Taylor approach is converged at $t_1^{VT} = 19.5$ ns. The position of the interface is at 70.4 nm. The solution for the Khachaturyan model is obtained at $t_1^K = 14.5$ ns. The bulk phases exceed the valid range by approximately 6%. The interface position is 61.6 nm, which is a considerable difference from the Voigt/Taylor approach.

6.5.1 Using a Non-linear Interpolation Function

A downside of the Khachaturyan approach as presented in chapter 5.1.1 is the linear interpolation. This was shown illustratively above, and it is discussed in chapter 6.2.2 and in Schmidt, Dornisch, and Müller (2019). In order to mitigate this issue, a non-linear interpolation function is used. For the sake of completeness, the field equations, the residual and the tangent matrix for the multivariant Khachaturyan approach using an arbitrary interpolation function are explained in the following. The equations for the residual in (6.23) and (6.24), and the equations for tangent matrix (6.28), (6.30), (6.33), and (6.35) still hold. The mechanical energy f^u , and subsequently their derivatives are changed. The effective material parameters are given by

$$\underline{\mathcal{C}}(\underline{\phi}) = \sum_{\alpha=0}^n \underline{\mathcal{C}}_{\alpha} h_{\alpha}^{\text{if}}(\underline{\phi}) = \underline{\mathcal{C}}_0 h_0^{\text{if}}(\underline{\phi}) + \sum_{\alpha=1}^n h(\phi_{\alpha}) \underline{\mathcal{C}}_{\alpha}. \quad (6.58)$$

Consequently, the transformation strain reads

$$\underline{\xi}^*(\underline{\phi}) = \sum_{\alpha=0}^n \underline{\xi}_{\alpha}^* h_{\alpha}^{\text{if}}(\underline{\phi}) = \underline{\xi}_0^* h_0^{\text{if}}(\underline{\phi}) + \sum_{\alpha=1}^n h(\phi_{\alpha}) \underline{\xi}_{\alpha}^*. \quad (6.59)$$

The elastic strain is given by

$$\underline{\xi}^e = \underline{\xi} - \underline{\xi}^*. \quad (6.60)$$

Thereby, the elastic energy can be determined

$$f^u(\underline{\xi}, \underline{\phi}) = \frac{1}{2} [\underline{\xi} - \underline{\xi}^*(\underline{\phi})] : \underline{\mathcal{C}} : [\underline{\xi} - \underline{\xi}^*(\underline{\phi})]. \quad (6.61)$$

The derivatives read

$$\begin{aligned} \frac{\partial f^u}{\partial \phi_{\alpha}} &= \frac{1}{2} \underline{\xi}^e : \frac{\partial \underline{\mathcal{C}}}{\partial \phi_{\alpha}} : \underline{\xi}^e + \underline{\xi}^e : \underline{\mathcal{C}} : \frac{\partial \underline{\xi}^e}{\partial \phi_{\alpha}} \\ \frac{\partial^2 f^u}{\partial \phi_{\alpha} \partial \phi_{\beta}} &= \frac{\partial \underline{\xi}^e}{\partial \phi_{\beta}} : \frac{\partial \underline{\mathcal{C}}}{\partial \phi_{\alpha}} : \underline{\xi}^e + \frac{1}{2} \underline{\xi}^e : \frac{\partial^2 \underline{\mathcal{C}}}{\partial \phi_{\alpha} \partial \phi_{\beta}} : \underline{\xi}^e \\ &+ \frac{\partial \underline{\xi}^e}{\partial \phi_{\beta}} : \underline{\mathcal{C}} : \frac{\partial \underline{\xi}^e}{\partial \phi_{\alpha}} + \underline{\xi}^e : \frac{\partial \underline{\mathcal{C}}}{\partial \phi_{\beta}} : \frac{\partial \underline{\xi}^e}{\partial \phi_{\alpha}} + \underline{\xi}^e : \underline{\mathcal{C}} : \frac{\partial^2 \underline{\xi}^e}{\partial \phi_{\alpha} \partial \phi_{\beta}}. \end{aligned} \quad (6.62)$$

$$\quad (6.63)$$

The derivative of the stress w.r.t. the order parameter is

$$\frac{\partial^2 f^u}{\partial \underline{\xi}^e \partial \phi_{\alpha}} = \frac{\partial \underline{\sigma}}{\partial \phi_{\alpha}} = \frac{\partial \underline{\mathcal{C}}}{\partial \phi_{\alpha}} : \underline{\xi}^e + \underline{\mathcal{C}} \frac{\partial \underline{\xi}^e}{\partial \phi_{\alpha}}. \quad (6.64)$$

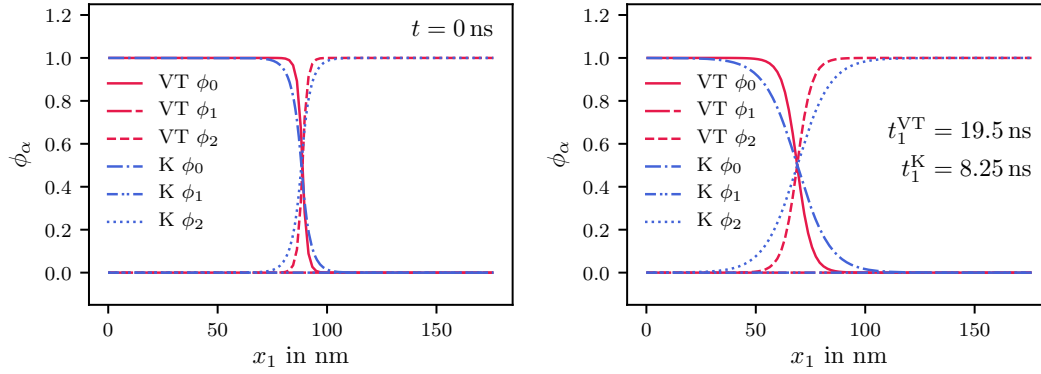


FIGURE 6.11: Example 4. Order parameter for the parent phase ϕ_0 (solid, dash-dot), and the martensitic orientation variants ϕ_1 (dashes-dash-dot-dot), and ϕ_2 (small dashes, dots) for the Khachaturyan (K, blue), and the Voigt/Taylor approach (VT, red). The static iteration is on the left, the stable state after the evolution is on the right.

The first and second order derivatives of the elastic strain and the effective material parameters are

$$\frac{\partial \underline{\mathcal{C}}}{\partial \phi_\alpha} = h'(\phi_\alpha) (\underline{\mathcal{C}}_\alpha - \underline{\mathcal{C}}_0), \quad \frac{\partial \underline{\xi}^e}{\partial \phi_\alpha} = -h'(\phi_\alpha) (\underline{\xi}_1^* - \underline{\xi}_0^*), \quad (6.65)$$

$$\frac{\partial \underline{\mathcal{C}}}{\partial \phi_\alpha} = \begin{cases} h''(\phi_\alpha) (\underline{\mathcal{C}}_\alpha - \underline{\mathcal{C}}_0), & \text{if } \alpha = \beta \\ 0, & \text{otherwise,} \end{cases} \quad \text{and} \quad (6.66)$$

$$\frac{\partial \underline{\xi}^e}{\partial \phi_\alpha} = \begin{cases} -h''(\phi_\alpha) (\underline{\xi}_\alpha^* - \underline{\xi}_0^*), & \text{if } \alpha = \beta \\ 0, & \text{otherwise.} \end{cases} \quad (6.67)$$

Here, h is a scalar interpolation function according to (4.22), for example linear (4.23), cubic (4.24) or tangens hyperbolicus (4.25). Figure 6.11 shows the evolution of the phase field at two distinct times. The initial configuration is shown for $t = 0$ ns. The phase field evolves. The final configuration is reached at 19.5 ns for the Voigt/Taylor approach where the interface is at $x_1 = 70.4$ nm. Using the cubic interpolation function in the Khachaturyan approach, the stable state is reached at 8.25 ns. The interface is located at $x_1 = 69.5$ nm. Using the same interpolation function in the two approaches, the same result within a margin of error is obtained.

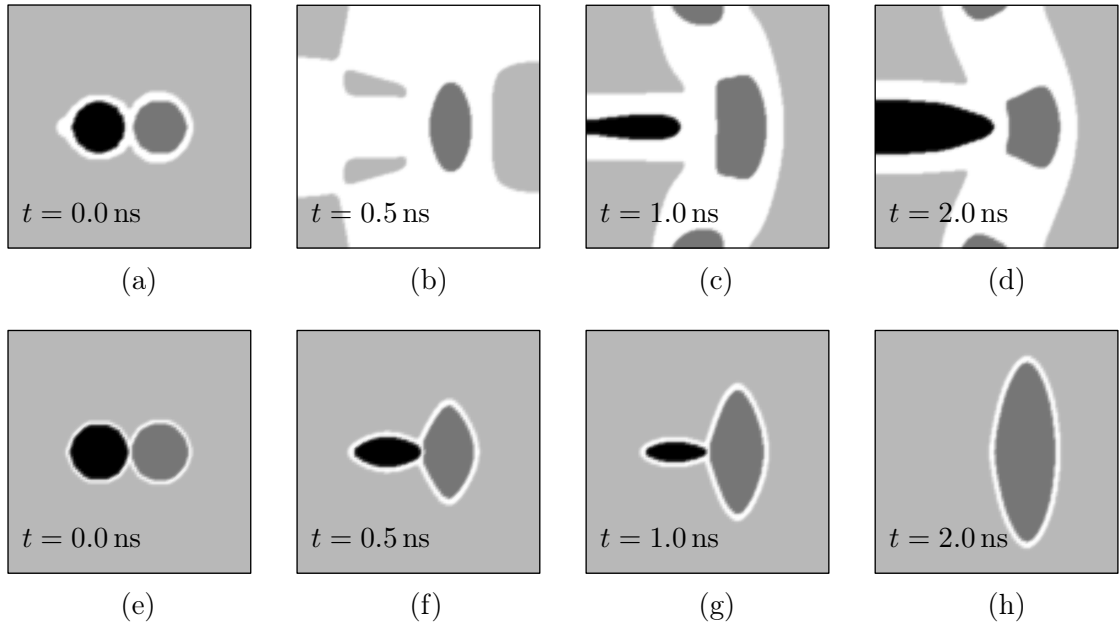


FIGURE 6.12: Time evolution of two spherical martensitic domains for the Khachaturyan approach (a), (b), (c), and (d), and for the Voigt/Taylor approach (e), (f), (g), (h). The first orientation variant (dark grey), the second orientation variant (black) and the austenitic parent phase (light grey), are separated by the interface region (white).

The example presented in Figure 6.12 shows the time evolution of two circular martensitic domains embedded in an austenitic matrix. The square region has an edge length of 176 nm. The number of elements is 200 in both x_1 and x_2 direction. The parameters are identical to the ones used in the examples above, with the exception of the specific length scale which is adjusted to $L = 10$ nm in order to resolve the interface more clearly. The parameter L is large enough to accommodate more than ten elements on the interface, leading to accurate result as shown in Table 6.2. The transformation strain for austenitic phase vanishes, but is present in the first and the second martensitic orientation variant

$$\boldsymbol{\varepsilon}_0^* = \mathbf{0}, \quad \boldsymbol{\varepsilon}_1^* = \begin{bmatrix} 0.1 & 0 \\ 0 & 0 \end{bmatrix}, \quad \text{and} \quad \boldsymbol{\varepsilon}_2^* = \begin{bmatrix} 0 & 0 \\ 0 & 0.1 \end{bmatrix}. \quad (6.68)$$

The bottom left node is fixed, and the bottom right node is a simple support. A displacement of 4.4 nm in x_1 -direction is applied to the right edge, which is equal to a total strain of 2.5 %.

No convergence was reached using a cubic or a tangens hyperbolicus interpolation function for the Khachaturyan approach. Therefore the snapshots for the Khachaturyan approach presented in Figure 6.12 (a), (b), (c), and (d) are obtained using the linear interpolation function. The respective snapshots for the Voigt/Taylor approach are conducted using a cubic interpolation function. The bulk regions are identified using the interpolation function. A bulk phase α is present, if its respective interpolation function reaches a threshold

$$h_\alpha(\phi) \stackrel{!}{\geq} h_{\text{thres}}. \quad (6.69)$$

Likewise, the interface region, which is represented in white, is identified with the absence of all bulk phases.

$$h_\alpha(\phi) \stackrel{!}{<} h_{\text{thres}}. \quad (6.70)$$

Here, h_{thres} was chosen to be 0.95.

Compare the static iteration for the Khachaturyan approach and the Voigt/Taylor approach, in Figure 6.12 (a) and (e), respectively. The interface width in Figure 6.12 (a) is larger than in (e). This is in line with the previous comparison, since the mismatch in the elastic energy causes a peak of the homogenized elastic energy in the interface region.

In the Voigt/Taylor approach, the second martensitic orientation variant de-evolves, as due to the load state the austenitic phase is energetically more stable. Both circular martensitic regions form a diamond shape in the direction of principal transformation strain in Figure 6.12 (b, c). After 2 ns, the second martensitic orientation variant vanishes, obtaining a structure consisting of the austenitic parent phase and the first orientation variant only as shown in Figure 6.12 (d).

In the Khachaturyan approach, initially, both phases de-evolve, forming a comparatively wide interface region in Figure 6.12 (f). However, the second martensitic orientation variant starts to form at the left side in order to mitigate the lateral strain, while the first orientation variant forms at top and bottom center region, as well as right to the center g). The configuration obtained in Figure 6.12 (h) consists of a plate with the second martensitic orientation variant to the left, and three patches of the second martensitic orientation variant.

The Voigt/Taylor approach produces a different result than the Khachaturyan approach. This is in line with the observations made in the previous examples. A linear interpolation function for the Khachaturyan approach is used, which causes the order parameter field to exceed its valid range locally. For the end solution at $t = 2.0$ ns, the excess was found to be 0.091 and 0.06 for the first and second martensitic orientation variant, respectively. The order parameter field in the Voigt/Taylor approach stays in the admissible range within a margin of error below machine precision. Therefore in this case, the latter provides a more accurate result than the Khachaturyan approach.

7 Conclusions

In chapter 5 the solid-solid phase transformation has been modeled with the phase field method. Using the Khachaturyan approach, a temperature dependent chemical potential has been presented. The potential uses data from molecular dynamics simulations. Hence, the martensitic transformation, and consequently the kinematics, depend on the temperature. Using finite element simulations, the model has been verified against the molecular dynamics simulation and an additional phase field model. The interface velocities obtained are well in agreement. At the equilibrium temperature, there is no phase transformation. With increasing distance from the equilibrium, the energy barrier is lower and thus the transformation, indicated by the interface velocity, is higher. Both, a metastable austenitic and a metastable martensitic phase can be modeled. Using finite element simulations, the influence of load on the martensitic transformation has been discussed. The temperature dependent chemical potential allows to assume a locally varying temperature field (chapter 5.1.1). Lower temperatures lead to a higher martensite content. However, the end result depends strongly on the initial configuration.

The Voigt/Taylor approach presented in chapter 6 has an advantage to the Khachaturyan approach. It is possible to choose individual material laws for each individual phase. As a consequence, the equations can be generalized to introduce an interface for constitutive laws of the individual phases. Here, a multivariant Voigt/Taylor scheme, modeling the martensitic transformation is presented. The interpolation method is crucial for the model. A generalized interpolation method, here called the case dependent interpolation method is presented, which works for any number of phases and any scalar interpolation function. In an initial test, several interpolation functions have been tested, or literature references are given where applicable. The Voigt/Taylor approach does not converge using a linear interpolation function. Instead a non-linear interpolation function, such as the cubic or a tangens hyperbolicus type function have to be used. The model has been verified using some basic energetic considerations. A relatively coarse mesh yields accurate results.

As a second step, the Voigt/Taylor approach has been compared to the Khachaturyan approach. In some cases, the same problem leads to the same results. However, due to the different energy landscapes, the models differ during the evolution. A downside of the Khachaturyan approach is, that its phase field can exceed its admissible range. In some of the examples shown, this is not an issue as the stable configuration does not exhibit this feature. Nonetheless, if the mechanical and the chemical energy are in interplay, the free energy is minimized by assuming inadmissible values or interface values for the bulk phases, since a linear interpolation was used in the Khachaturyan model. Therefore the Khachaturyan model has been modified in order to accommodate a scalar interpolation function. Using the cubic interpolation function in both models, for example, the same result was obtained as in the Voigt/Taylor model, thus cross-verifying the models.

The code has been implemented in the finite element analysis program FEAP and in the finite element solver Zébulon. Both models have been developed separately. The implementation in FEAP is presented in this thesis, the implementation in the finite element solver Zébulon was conducted by the group of Kais Ammar and Samuel Forest at the Ecole des Mines Paristech, Paris, France. The results of both implementations agree, which is a good indicator for their validity. The implemented models feature the linear elastic Khachaturyan approach with n number of phases and an interface to an arbitrary scalar interpolation function. The Voigt/Taylor approach features an interface to material routines for the individual phases, as well as an interface to an arbitrary scalar interpolation function.

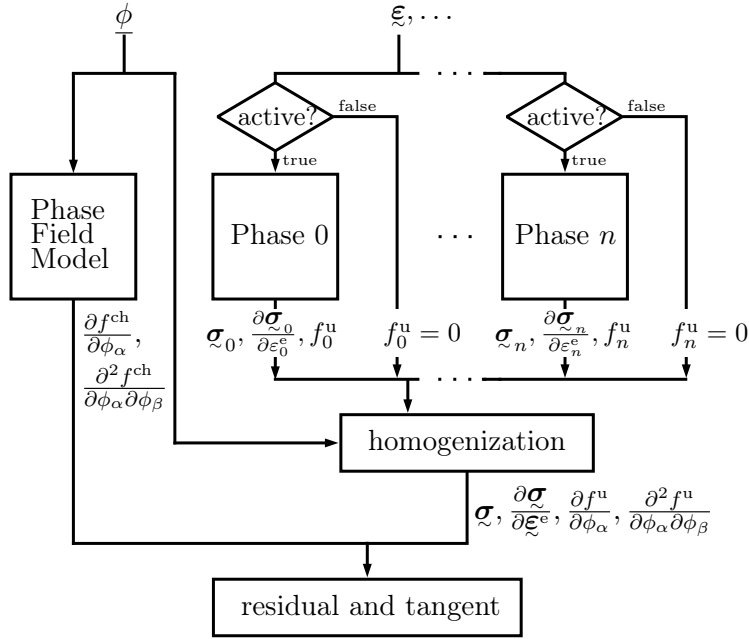


FIGURE 7.1: Flow chart of a modified Voigt/Taylor homogenization approach

7.1 Outlook

The Voigt/Taylor model presented here can be used to model the martensitic transformation. A more comprehensive test should be made in order to lay out the differences between the Khachaturyan and the Voigt/Taylor approach. Furthermore, the model can be used to determine the martensitic content in a more realistic setting. This has proven to work comparatively well for the Khachaturyan model (Schmidt, Dornisch, and Müller, 2019).

The Voigt/Taylor model is computationally expensive. Each individual phase contains an individual material law, which needs to be solved. A first step would be the parallelization of the individual phases. This is straightforward, as they are parallel in the algorithm as well. In an additional step, the phases could be determined to be either active, or inactive before entering the material routines as shown in Figure 7.1. A criterion if a phase is active or inactive needs to be developed. A possible indicator for the activity of a phase could be the phase composition.

Bibliography

- Aihara, S., T. Takaki, and N. Takada (2019). “Multi-phase-field modeling using a conservative Allen–Cahn equation for multiphase flow”. In: *Computers & Fluids* 178, pp. 141–151.
- Allen, S. M. and J. W. Cahn (1979). “A microscopic theory for antiphase boundary motion and its application to antiphase domain coarsening”. In: *Acta metallurgica* 27.6, pp. 1085–1095.
- Ammar, K., B. Appolaire, G. Cailletaud, and S. Forest (2009). “Combining phase field approach and homogenization methods for modelling phase transformation in elastoplastic media”. In: *European Journal of Computational Mechanics/Revue Européenne de Mécanique Numérique* 18.5-6, pp. 485–523.
- Artemev, A., Y. Jin, and A. G. Khachaturyan (2001). “Three-dimensional phase field model of proper martensitic transformation”. In: *Acta materialia* 49.7, pp. 1165–1177.
- Artemev, A., Y. Wang, and A. G. Khachaturyan (2000). “Three-dimensional phase field model and simulation of martensitic transformation in multilayer systems under applied stresses”. In: *Acta Materialia* 48.10, pp. 2503–2518.
- Aurich, J. C., P. Mayer, B. Kirsch, D. Eifler, M. Smaga, and R. Skorupski (2014). “Characterization of deformation induced surface hardening during cryogenic turning of AISI 347”. In: *CIRP Annals* 63.1, pp. 65–68.
- Bain, E. C. and N. Dunkirk (1924). “The nature of martensite”. In: *trans. AIME* 70.1, pp. 25–47.
- Banerjee, S. and P. Mukhopadhyay (2010). *Phase transformations: examples from titanium and zirconium alloys*. Elsevier.
- Becker, S., H. Hotz, B. Kirsch, J. C. Aurich, E. von Harbou, and R. Müller (2018). “A finite element approach to calculate temperatures arising during cryogenic turning of metastable austenitic steel AISI 347”. In: *Journal of Manufacturing Science and Engineering* 140.10.
- Becker, W. and D. Gross (2013). *Mechanik elastischer Körper und Strukturen*. Springer-Verlag.
- Bhadeshia, H. K. D. H. (2017). *Geometry of crystals, polycrystals, and phase transformations*. CRC press.

- Bhadeshia, H. K. D. H. (2019). *Bainite in steels: theory and practice*. CRC Press.
- Bilby, B. and J. W. Christian (1956). “Martensitic transformations”. In: *The mechanism of phase transformations in metals* 121.
- Bowles, J. and J. Mackenzie (1954). “The crystallography of martensite transformations I”. In: *Acta metallurgica* 2.1, pp. 129–137.
- Brinksmeier, E., M. Garbrecht, and D. Meyer (2008). “Cold surface hardening”. In: *CIRP annals* 57.1, pp. 541–544.
- Brinksmeier, E., M. Garbrecht, D. Meyer, and J. Dong (2008). “Surface hardening by strain induced martensitic transformation”. In: *Production Engineering* 2.2, pp. 109–116.
- Cahn, J. W. and S. M. Allen (1977). “A microscopic theory for domain wall motion and its experimental verification in Fe-Al alloy domain growth kinetics”. In: *Le Journal de Physique Colloques* 38.C7, pp. C7–51.
- Cahn, J. W. (1959). “Free energy of a nonuniform system. II. Thermodynamic basis”. In: *The Journal of chemical physics* 30.5, pp. 1121–1124.
- Cahn, J. W. and J. E. Hilliard (1958). “Free energy of a nonuniform system. I. Interfacial free energy”. In: *The Journal of chemical physics* 28.2, pp. 258–267.
- Choudhury, S., Y. L. Li, C. E. Krill III, and L.-Q. Chen (2005). “Phase-field simulation of polarization switching and domain evolution in ferroelectric polycrystals”. In: *Acta Materialia* 53.20, pp. 5313–5321.
- Christian, J. W. (1997). “Lattice correspondence, atomic site correspondence and shape change in “diffusional-displacive” phase transformations”. In: *Progress in materials science* 42.1-4, pp. 101–108.
- Christian, J. W., G. B. Olson, and M. Cohen (1995). “Classification of displacive transformations: What is a martensitic transformation?” In: *Le Journal de Physique IV* 5.C8, pp. C8–3.
- Cohen, M., G. Olson, and P. Clapp (1979). “On the classification of displacive phase transformations”. In: *Proceedings of the International Conference on Martensitic Transformations ICOMAT’79*, pp. 1–11.
- Cooman, B. C. de, O. Kwon, and K.-G. Chin (2012). “State-of-the-knowledge on TWIP steel”. In: *Materials Science and Technology* 28.5, pp. 513–527.
- Deng, D. (2009). “FEM prediction of welding residual stress and distortion in carbon steel considering phase transformation effects”. In: *Materials & Design* 30.2, pp. 359–366.
- Dhananchezian, M., M. P. Kumar, and T. Sornakumar (2011). “Cryogenic turning of AISI 304 stainless steel with modified tungsten carbide tool inserts”. In: *Materials and Manufacturing Processes* 26.5, pp. 781–785.

- Diewald, F., C. Kuhn, M. Heier, K. Langenbach, M. Horsch, H. Hasse, and R. Müller (2018). “Investigating the stability of the phase field solution of equilibrium droplet configurations by eigenvalues and eigenvectors”. In: *Computational Materials Science* 141, pp. 185–192.
- Dornisch, W., D. Schrade, B.-X. Xu, M.-A. Keip, and R. Müller (2019). “Coupled phase field simulations of ferroelectric and ferromagnetic layers in multiferroic heterostructures”. In: *Archive of Applied Mechanics* 89.6, pp. 1031–1056.
- Echebarria, B., R. Folch, A. Karma, and M. Plapp (2004). “Quantitative phase-field model of alloy solidification”. In: *Physical Review E* 70.6, p. 061604.
- Ellingham, H. J. T. (1944). “Reducibility of oxides and sulfides in metallurgical processes”. In: *J Soc Chem Ind* 63, pp. 125–133.
- Eshelby, J. D. (1957). “The determination of the elastic field of an ellipsoidal inclusion, and related problems”. In: *Proceedings of the royal society of London. Series A. Mathematical and physical sciences* 241.1226, pp. 376–396.
- (1959). “The elastic field outside an ellipsoidal inclusion”. In: *Proceedings of the Royal Society of London. Series A. Mathematical and Physical Sciences* 252.1271, pp. 561–569.
- Fan, D., S. Chen, L.-Q. Chen, and P. W. Voorhees (2002). “Phase-field simulation of 2-D Ostwald ripening in the high volume fraction regime”. In: *Acta Materialia* 50.8, pp. 1895–1907.
- Fick, A. (1855a). “Ueber diffusion”. In: *Annalen der Physik* 170.1, pp. 59–86.
- (1855b). “V. On liquid diffusion”. In: *The London, Edinburgh, and Dublin Philosophical Magazine and Journal of Science* 10.63, pp. 30–39.
- Fried, E. and M. E. Gurtin (1993). “Continuum theory of thermally induced phase transitions based on an order parameter”. In: *Physica D: Nonlinear Phenomena* 68.3-4, pp. 326–343.
- (1994). “Dynamic solid-solid transitions with phase characterized by an order parameter”. In: *Physica. D, Nonlinear phenomena* 72.4, pp. 287–308.
- Gauss, C. F. (1823). *Theoria combinationis observationum erroribus minimis obnoxiae*. Vol. 1. H. Dieterich.
- Gibbs, J. W. (1873). “A method of geometrical representation of the thermodynamic properties by means of surfaces”. In: *Transactions of Connecticut Academy of Arts and Sciences*, pp. 382–404.
- Greninger, A. B. and A. R. Troiano (1949). “The mechanism of martensite formation”. In: *Trans. AIME* 185.9, pp. 590–598.
- Guggenheim, E. (1993). *An Advanced Treatment for Chemists and Physicists*.

- Gurtin, M. E. (1982). *An introduction to continuum mechanics*. Academic press.
- (1994). “Generalized Ginzburg-Landau and Cahn-Hilliard equations based on a microforce balance”. In:
- (1999). *Configurational forces as basic concepts of continuum physics*. Vol. 137. Springer Science & Business Media.
- Headley, T. and J. Brooks (2002). “A new bcc-fcc orientation relationship observed between ferrite and austenite in solidification structures of steels”. In: *Metallurgical and materials transactions A* 33.1, pp. 5–15.
- Heep, T., C. Bickert, and E. Abele (2019). “Application of carbon dioxide snow in machining of CGI using an additively manufactured turning tool”. In: *Journal of Manufacturing and Materials Processing* 3.1, p. 15.
- Heida, M. (2013). “On the derivation of thermodynamically consistent boundary conditions for the Cahn–Hilliard–Navier–Stokes system”. In: *International Journal of Engineering Science* 62, pp. 126–156.
- Helmholtz, H. von (1882). “On the thermodynamics of chemical processes”. In: *Physical Memoirs Selected and Translated from Foreign Sources* 1, pp. 43–97.
- Hori, M. and S. Nemat-Nasser (1999). “On two micromechanics theories for determining micro–macro relations in heterogeneous solids”. In: *Mechanics of Materials* 31.10, pp. 667–682.
- Ishihara, K., M Maeda, and P. Shingu (1985). “The nucleation of metastable phases from undercooled liquids”. In: *Acta Metallurgica* 33.12, pp. 2113–2117.
- Jin, Y. M. (2009). “Domain microstructure evolution in magnetic shape memory alloys: phase-field model and simulation”. In: *Acta Materialia* 57.8, pp. 2488–2495.
- Kelly, P. (2006). “Martensite crystallography—The role of the shape strain”. In: *Materials Science and Engineering: A* 438, pp. 43–47.
- (2012). “Crystallography of martensite transformations in steels”. In: *Phase transformations in steels*. Elsevier, pp. 3–33.
- Khachaturyan, A. G. (2013). *Theory of structural transformations in solids*. Courier Corporation.
- Kim, H. Y. and S. Miyazaki (2018). “Chapter 1 - Martensitic Transformation Characteristics”. In: *Ni-Free Ti-Based Shape Memory Alloys*. Ed. by H. Y. Kim and S. Miyazaki. Butterworth-Heinemann, pp. 1–52.
- Kobasko, N, M Aronov, J Powell, and J Vanas (2009). “Intensive Quenching of Steel Parts: Equipment and Method”. In: *Proceedings of the 7th IASME/WSEAS International Conference on Health Transfer, Thermal Engineering and Environment, Moscow, Russia*, pp. 20–22.

- Kobayashi, R. (1993). “Modeling and numerical simulations of dendritic crystal growth”. In: *Physica D: Nonlinear Phenomena* 63.3-4, pp. 410–423.
- Koumatos, K. and A. Muehleemann (2017). “A theoretical investigation of orientation relationships and transformation strains in steels”. In: *Acta Crystallographica Section A: Foundations and Advances* 73.2, pp. 115–123.
- Kuhn, C. (2013). *Numerical and Analytical Investigation of a Phase Field Model for Fracture*.
- Kuhn, C. and R. Müller (2010). “A continuum phase field model for fracture”. In: *Engineering Fracture Mechanics* 77.18, pp. 3625–3634.
- Kundu, S., A. K. Verma, and V. Sharma (2012). “Quantitative analysis of variant selection for displacive transformations under stress”. In: *Metallurgical and Materials Transactions A* 43.7, pp. 2552–2565.
- Kurdjumow, G and G. Sachs (1930). “Über den Mechanismus der Stahlhärtung”. In: *Zeitschrift für Physik* 64.5-6, pp. 325–343.
- Ledbetter, H. and M. L. Dunn (2000). “Equivalence of Eshelby inclusion theory and Wechsler–Lieberman–Read, Bowles–Mackenzie martensite-crystallography theories”. In: *Materials Science and Engineering: A* 285.1-2, pp. 180–185.
- Li, Z., Y. Jiang, Z. Li, Y. Yang, B. Yang, Y. Zhang, C. Esling, X. Zhao, and L. Zuo (2016). “Texture inheritance from austenite to 7 M martensite in Ni–Mn–Ga melt-spun ribbons”. In: *Results in physics* 6, pp. 428–433.
- Maalekian, M. and E. Kozeschnik (2011). “Modeling mechanical effects on promotion and retardation of martensitic transformation”. In: *Materials Science and Engineering: A* 528.3, pp. 1318–1325.
- Mackenzie, J. and J. Bowles (1954). “The crystallography of martensite transformations II”. In: *Acta Metallurgica* 2.1, pp. 138–147.
- Mayer, P., B. Kirsch, and J. C. Aurich (2014). “Investigations on cryogenic turning to achieve surface hardening of metastable austenitic steel AISI 347”. In: *Advanced materials research*. Vol. 1018. Trans Tech Publ, pp. 153–160.
- Mayer, P., R. Skorupski, M. Smaga, D. Eifler, and J. C. Aurich (2014). “Deformation induced surface hardening when turning metastable austenitic steel AISI 347 with different cryogenic cooling strategies”. In: *Procedia CIRP* 14, pp. 101–106.
- Miehe, C., F. Welschinger, and M. Hofacker (2010). “Thermodynamically consistent phase-field models of fracture: Variational principles and multi-field FE implementations”. In: *International Journal for Numerical Methods in Engineering* 83.10, pp. 1273–1311.
- Mosler, J., O. Shchyglo, and H. M. Hojjat (2014). “A novel homogenization method for phase field approaches based on partial rank-one relaxation”. In: *Journal of the Mechanics and Physics of Solids* 68, pp. 251–266.

- Muench, I, C. Gierden, and W Wagner (2018). “A phase field model for stress-based evolution of load-bearing structures”. In: *International Journal for Numerical Methods in Engineering* 115.13, pp. 1580–1600.
- Nadgir, O., W. Dornisch, R. Müller, and M.-A. Keip (2019). “A phase-field model for transversely isotropic ferroelectrics”. In: *Archive of Applied Mechanics* 89.6, pp. 1057–1068.
- Nishiyama, Z. (1934). “X-ray investigation of the mechanism of the transformation from face centered cubic lattice to body centered cubic”. In: *Sci. Rep. Tohoku Univ.* 23, p. 637.
- Novelli, M., P. Maurel, L. Weiss, T. Grosdidier, and P. Bocher (2017). “Stress-assisted versus strain-induced martensites formed by cryogenic ultrasonic shot peening in austenitic stainless steels”. In: *International Conference of Shot Peening ICSP-13*.
- Olson, G. B. and M. Cohen (1976a). “A general mechanism of martensitic nucleation: Part I. General concepts and the FCC→ HCP transformation”. In: *Metallurgical Transactions A* 7.12, pp. 1897–1904.
- (1976b). “A general mechanism of martensitic nucleation: Part II. FCC→ BCC and other martensitic transformations”. In: *Metallurgical transactions A* 7.12, pp. 1905–1914.
- (1976c). “A general mechanism of martensitic nucleation: Part III. Kinetics of martensitic nucleation”. In: *Metallurgical Transactions A* 7.12, pp. 1915–1923.
- (1982). “Stress-assisted isothermal martensitic transformation: application to TRIP steels”. In: *Metallurgical Transactions A* 13.11, pp. 1907–1914.
- (1986). *Dislocations in Solids, edited by FRN Nabarro*.
- Patel, J. R. and M. Cohen (1953). “Criterion for the action of applied stress in the martensitic transformation”. In: *Acta metallurgica* 1.5, pp. 531–538.
- Pepper, D. W. and J. C. Heinrich (2017). *The finite element method: basic concepts and applications with MATLAB, MAPLE, and COMSOL*. CRC press.
- Persson, K. (Jan. 2015). *Materials Data on Fe (SG:229) by Materials Project*. An optional note.
- Porter, D. A., K. E. Easterling, and M. Sherif (2009). *Phase Transformations in Metals and Alloys, (Revised Reprint)*. CRC press.
- Qin, R. S. and H. K. Bhadeshia (2010). “Phase field method”. In: *Materials Science and Technology* 26.7, pp. 803–811. eprint: <https://doi.org/10.1179/174328409X453190>.
- Rancourt, V. de, B. Appolaire, S. Forest, and K. Ammar (2016). “Homogenization of viscoplastic constitutive laws within a phase field approach”. In: *Journal of the Mechanics and Physics of Solids* 88, pp. 35–48.

- Sandoval, L., H. M. Urbassek, and P. Entel (2009). “The Bain versus Nishiyama–Wassermann path in the martensitic transformation of Fe”. In: *New Journal of Physics* 11.10, p. 103027.
- Schlüter, A., A. Willenbücher, C. Kuhn, and R. Müller (2014). “Phase field approximation of dynamic brittle fracture”. In: *Computational Mechanics* 54.5, pp. 1141–1161.
- Schmidt, S., W. Dornisch, and R. Müller (2017a). “A phase field model for martensitic transformation coupled with the heat equation”. In: *GAMM-Mitteilungen* 40.2, pp. 138–153.
- (2017b). “A phase field model for martensitic transformation coupled with the heat equation”. In: *GAMM-Mitteilungen* 40.2, pp. 138–153.
- (2019). “Martensitic transformation at a crack under mode I and II loading”. In: *PAMM* 19.1, e201900465.
- Schmidt, S., C. Plate, R. Müller, R. Müller, J. Meiser, and H. M. Urbassek (2016). “A phase field model for martensitic transformations with a temperature-dependent separation potential”. In: *PAMM* 16.1, pp. 481–482.
- Schmitt, R., C. Kuhn, R. Müller, and K. Bhattacharya (2014). “Crystal Plasticity and Martensitic Transformations”. In: *Technische Mechanik. Scientific Journal for Fundamentals and Applications of Engineering Mechanics* 34.1, pp. 23–38.
- Schmitt, R., C. Kuhn, and R. Müller (2017). “On a phase field approach for martensitic transformations in a crystal plastic material at a loaded surface”. In: *Continuum Mechanics and Thermodynamics* 29.4, pp. 957–968.
- Schmitt, R., R. Müller, and C. Kuhn (2012). “A phase field model for martensitic transformations”. In: *PAMM* 12.1, pp. 261–262.
- Schmitt, R., R. Müller, C. Kuhn, and H. M. Urbassek (2013a). “A phase field approach for multivariant martensitic transformations of stable and metastable phases”. In: *Archive of Applied Mechanics* 83.6, pp. 849–859.
- Schmitt, R., B. Wang, and H. M. Urbassek (2013b). “Modeling of Martensitic Transformations in Pure Iron by a Phase Field Approach Using Information from Atomistic Simulation”. In: pp. 119–130.
- Schneider, D., E. Schoof, Y. Huang, M. Selzer, and B. Nestler (2016). “Phase-field modeling of crack propagation in multiphase systems”. In: *Computer Methods in Applied Mechanics and Engineering* 312, pp. 186–195.
- Schrade, D., R. Mueller, B. X. Xu, and D. Gross (2007). “Domain evolution in ferroelectric materials: A continuum phase field model and finite element implementation”. In: *Computer Methods in Applied Mechanics and Engineering* 196, pp. 4365–4374.

- Song, H. and J. J. Hoyt (2012). “A molecular dynamics simulation study of the velocities, mobility and activation energy of an austenite–ferrite interface in pure Fe”. In: *Acta materialia* 60.10, pp. 4328–4335.
- (2013). “An atomistic simulation study of the migration of an austenite–ferrite interface in pure Fe”. In: *Acta materialia* 61.4, pp. 1189–1196.
- Steinbach, I. (2009). “Phase-field models in materials science”. In: *Modelling and simulation in materials science and engineering* 17.7, p. 073001.
- Strangwood, M. (2012). “Fundamentals of ferrite formation in steels”. In: *Phase Transformations in Steels*. Elsevier, pp. 187–224.
- Su, Y. and C. M. Landis (2007). “Continuum thermodynamics of ferroelectric domain evolution: Theory, finite element implementation, and application to domain wall pinning”. In: *Journal of the Mechanics and Physics of Solids* 55.2, pp. 280–305.
- Taylor, R. L. (2014). *FEAP-A finite element analysis program*.
- Tschukin, O., A. Silberzahn, M. Selzer, P. G. Amos, D. Schneider, and B. Nestler (2017). “Concepts of modeling surface energy anisotropy in phase-field approaches”. In: *Geothermal Energy* 5.1, p. 19.
- Urbassek, H. and L Sandoval (2012). *Phase transformations in steels, vol. 2: Diffusionless transformations, high strength steels, modelling and advanced analytical techniques*.
- Vvedensky, D. D. “Diffusionless transformations”. In: ().
- Wang, B. and H. M. Urbassek (2012). “study CO TT”. In: ii.
- Wang, J., P. J. van der Wolk, and S. van der Zwaag (2000). “Determination of martensite start temperature in engineering steels part I. Empirical relations describing the effect of steel chemistry”. In: *Materials transactions, JIM* 41.7, pp. 761–768.
- Wang, J. and J. Zhang (2013). “A real-space phase field model for the domain evolution of ferromagnetic materials”. In: *International Journal of Solids and Structures* 50.22-23, pp. 3597–3609.
- Wang, S.-L., R. Sekerka, A. Wheeler, B. Murray, S. Coriell, R. Braun, and G. McFadden (1993). “Thermodynamically-consistent phase-field models for solidification”. In: *Physica D: Nonlinear Phenomena* 69.1-2, pp. 189–200.
- Wang, Y and A. Khachaturyan (1997). “Three-dimensional field model and computer modeling of martensitic transformations”. In: *Acta materialia* 45.2, pp. 759–773.
- Wassermann, G. (1935). “Über den Mechanismus der a-g Umwandlung des Eisens”. In: *Mitt. K-Wilh-Inst. Eisenforsch* 17, pp. 149–155.
- Wechsler, M. S., D. S. Lieberman, and T. A. Read (1953). “On the theory of the formation of martensite”. In: *Trans. Aime* 197.11, pp. 1503–1515.

- West, A. R. (1999). *Basic solid state chemistry*. John Wiley & Sons Incorporated.
- Wheeler, A. A., W. J. Boettinger, and G. B. McFadden (1993). “Phase-field model of solute trapping during solidification”. In: *Physical Review E* 47.3, p. 1893.
- Yamagata, H. (2005). “8 - The crankshaft”. In: *The Science and Technology of Materials in Automotive Engines*. Ed. by H. Yamagata. Woodhead Publishing, pp. 165–206.
- Yamanaka, A., T. Takaki, and Y. Tomita (2008). “Elastoplastic phase-field simulation of self- and plastic accommodations in Cubic-tetragonal martensitic transformation”. In: *Materials Science and Engineering: A* 491.1, pp. 378–384.
- Yardley, V. and E. Payton (2014). “Austenite–martensite/bainite orientation relationship: characterisation parameters and their application”. In: *Materials Science and Technology* 30.9, pp. 1125–1130.
- Zhang, J. X. and L. Q. Chen (2005). “Phase-field model for ferromagnetic shape-memory alloys”. In: *Philosophical Magazine Letters* 85.10, pp. 533–541.
- Zhang, W., Y. M. Jin, and A. G. Khachaturyan (2007). “Phase field microelasticity modeling of heterogeneous nucleation and growth in martensitic alloys”. In: *Acta Materialia* 55.2, pp. 565–574.
- Zhou, S. and M. Y. Wang (2007). “Multimaterial structural topology optimization with a generalized Cahn–Hilliard model of multiphase transition”. In: *Structural and Multidisciplinary Optimization* 33.2, p. 89.

8 Appendix

8.1 Additional Plots for the Interface Velocity

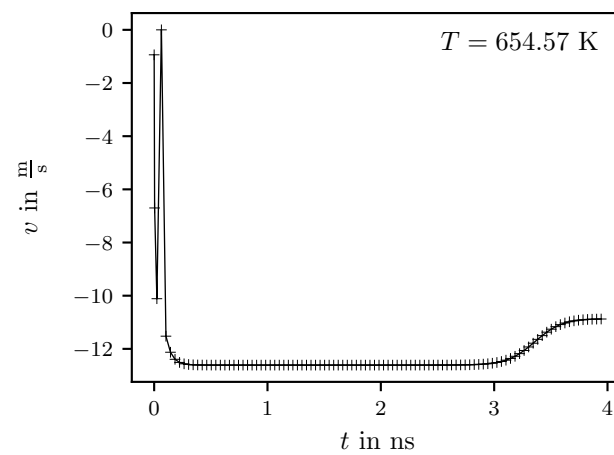


FIGURE 8.1: Interface velocity over time for $T = 654.57 \text{ K}$

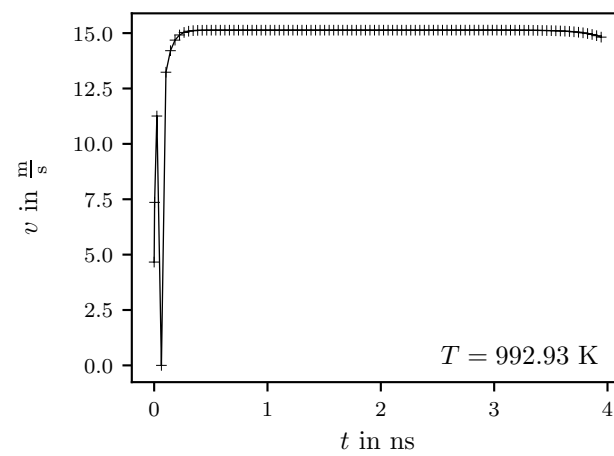


FIGURE 8.2: Interface velocity over time for $T = 992.92 \text{ K}$

8.2 Comparison of Interpolation Methods

This section complements chapter 4.4 with further illustrative examples. Figure 8.3 (a) shows the analogous approach using a cubic interpolation function. The triangular shaped admissible region of the order parameter, delimited by the dashed lines (-), contains a minimum. Depending on which value is to be interpolated, e.g., the elastic energy, or the transformation strain, the energy could be minimized by moving towards this minimum. However, this minimum is not as strongly represented as when using the tanh interpolation function (Figure 4.1 (a)). Furthermore, the cubic interpolation function is not bounded. This introduces another possible instability.

Figure 8.3 (b) shows the case dependent approach. The bulk values are constant, $a_\alpha = 1$. Therefore the representation coincides with any other scalar interpolation function. Here, the admissible region of the order parameter mitigates the unphysical minimum and the unbounded nature of the graph in Figure 8.3 (a).

The Figures 8.4, 8.5, and 8.6 show the linear, the cubic and the tangens hyperbolicus interpolation methods using the analogous h^{an} and the case dependent approach h^{if} . Here, the bulk values vary, $a_0 = 1$, $a_1 = 2$, and $a_2 = 3$. As discussed in chapter 4.4, the analogous and the case dependent approach are equivalent when using the linear interpolation. A downside of the linear interpolation is, however, that the second order derivatives vanish. This results in a non-converging behavior using the Voigt/Taylor homogenization approach (chapter 6). Furthermore, the non-vanishing first order derivatives lead can lead to a driving force in the bulk phases where $\underline{\phi} \in [\underline{0}, \underline{e}_1, \underline{e}_2]$. Additionally, the codomain of the linear interpolation is not limited. Therefore solutions outside the admissible range can exist.

With a non-linear interpolation function, such as the cubic and the tangens hyperbolicus, the choice between the analogous and the case dependent approach matters. Non-linear interpolation functions can be classified into two groups: ones with a limited codomain, and those ones with a vanishing first order derivative. The cubic interpolation function shown in Figure 8.5 belongs to the latter, mitigating the occurrence of a driving force in the bulk phases. The codomain of the tangens hyperbolicus interpolation is limited to the interval $[0, 1]$. Therefore even if the order parameter exceeds its admissible range, the value of the tangens hyperbolicus interpolation stays admissible.

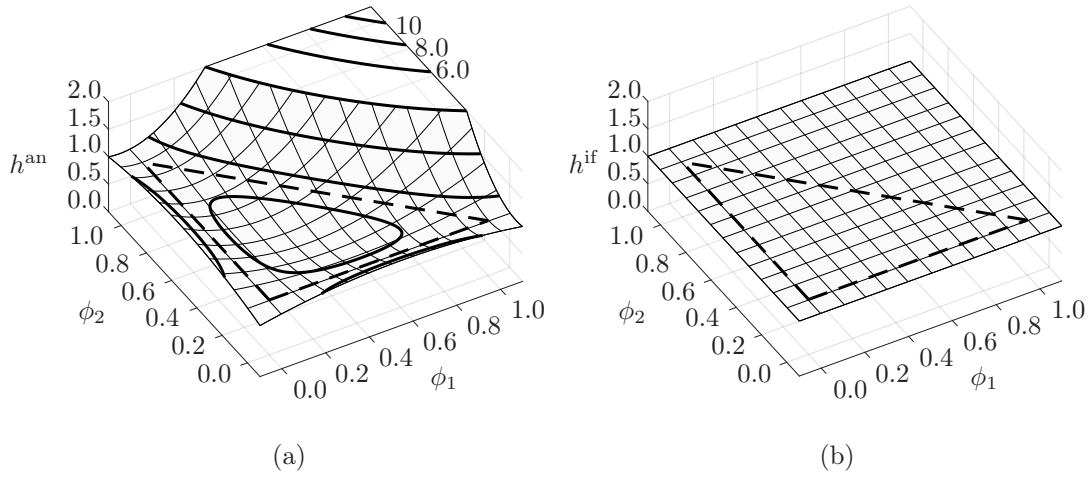


FIGURE 8.3: Comparison of the analogous interpolation approach h^{an} using a cubic interpolation, where $\theta = 5$ (a), and the case dependent interpolation approach h^{if} for any scalar interpolation function (b). The bulk values are constant, $a_\alpha = 1$. The dashed lines (-) indicate the boundary of the region where $\underline{\phi}$ is admissible. Contour lines (thick) above 2 are projected down to 2.

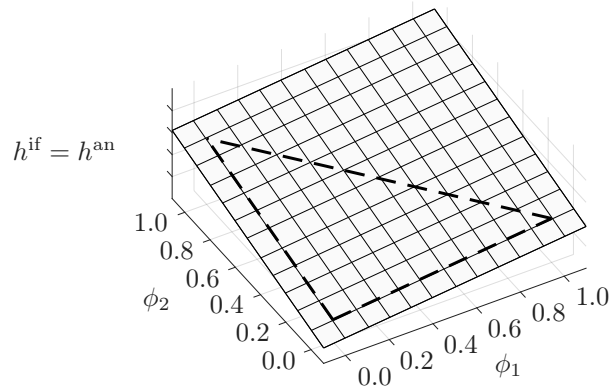


FIGURE 8.4: Linear interpolation, where $h^{\text{if}} = h^{\text{an}}$, with varying bulk values vary, $a_0 = 1$, $a_1 = 2$, and $a_2 = 3$. The dashed lines (-) indicate the boundary of the region where $\underline{\phi}$ is admissible.

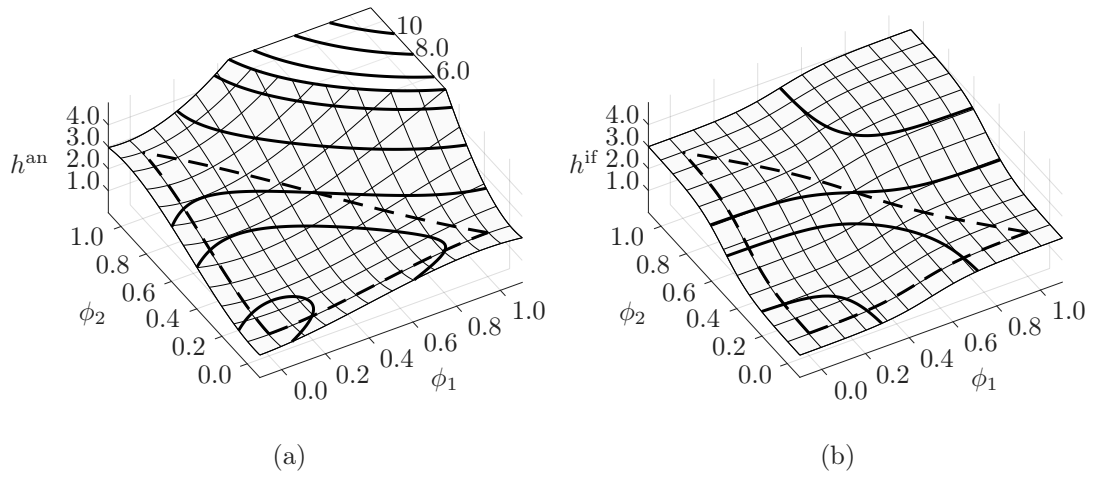


FIGURE 8.5: Comparison of the analogous interpolation approach h^{an} using a cubic interpolation, where $\theta = 5$ (a), and the case dependent interpolation approach h^{if} for any scalar interpolation function (b). The bulk values vary, $a_0 = 1$, $a_1 = 2$, and $a_2 = 3$. The dashed lines (-) indicate the boundary of the region where $\underline{\phi}$ is admissible.

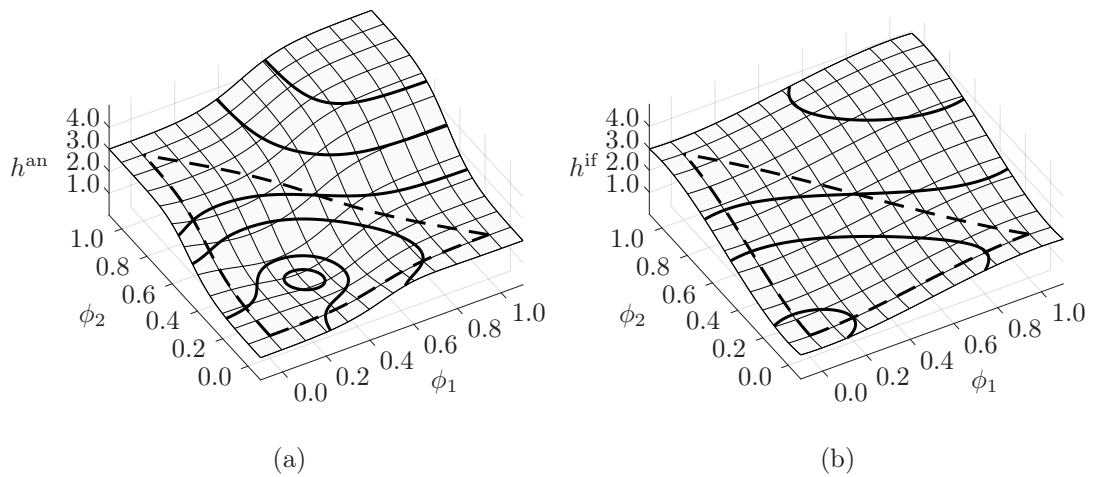


FIGURE 8.6: Comparison of the analogous interpolation approach h^{an} using a tanh interpolation, where $\theta = 5$ (a), and the case dependent interpolation approach h^{if} for any scalar interpolation function (b). The bulk values vary, $a_0 = 1$, $a_1 = 2$, and $a_2 = 3$. The dashed lines (-) indicate the boundary of the region where $\underline{\phi}$ is admissible.

Lebenslauf

Name Simon David Schmidt
 Geburtsort Saarbrücken
 Nationalität Deutsch

August 1998 - Juni 2002 Grundschule Südschule St. Ingbert

August 2002 - Juni 2010 Albertus-Magnus-Gymnasium St. Ingbert
 Abschluss: Allgemeine Hochschulreife

Oktober 2010 - Januar 2016 Studium Maschinenbau und Verfahrenstechnik
 Technische Universität Kaiserslautern

Diplomarbeit: *Determination of the Aerodynamic Quality of Single Slotted Arc-Cambered Sheet Blades with Constant Thickness by Experimental and Theoretical Methods*

Abschluss: Diplomingenieur Maschinenbau

Februar 2016 - Dezember 2019 Wissenschaftlicher Mitarbeiter
 Lehrstuhl für technische Mechanik
 Fachbereich Maschinenbau und Verfahrenstechnik
 Technische Universität Kaiserslautern